J. Fluid Mech. (1989), *vol.* 208, *pp.* 257–320
Printed in Great Britain

Elliptic jets. Part 1. Characteristics of unexcited and excited jets

By FAZLE HUSSAIN AND HYDER S. HUSAIN
Department of Mechanical Engineering, University of Houston, Houston, TX 77204-4792, USA

(Received 18 March 1988 and in revised form 20 April 1989)

This paper summarizes experimental studies of incompressible elliptic jets of different aspect ratios and initial conditions, and effects of excitations at selected frequencies and amplitudes. Elliptic jets are quite different from the extensively studied plane and circular jets – owing mainly to the fact that the azimuthal curvature variation of a vortical structure causes its non-uniform self-induction and hence complex three-dimensional deformation. Such deformation, combined with properly selected excitation can substantially alter entrainment and other turbulence phenomena, thus suggesting preference for the elliptic shape in many jet applications. The dominance of coherent structures in the jet far field is evident from the finding that switching over of the cross-section shape continues at least up to 100 equivalent diameters D_e. The locations and the number of switchovers are strongly dependent on the initial condition, on the aspect ratio, and, when excited, on the Strouhal number and the excitation level. We studied jets with constant exit momentum thickness θ_e all around the perimeter, thus separating the effects of azimuthal variations of θ_e (typical of elliptic jets) and of the shear-layer curvature. Also investigated are the instability characteristics, and enhanced entrainment caused by bifurcation as well as pairing of vortical structures. We discuss shear-layer and jet-column domains, and find the latter to be characterized by two modes: the preferred mode and the stable pairing mode – similar to those found in circular jets – both modes scaling on the newly-defined lengthscale D_e. The paper documents some time-average measurements and their comparison with those in circular and plane jets.

CONTENTS

1. Introduction

The elliptic jet is intermediate between the two limiting shapes: the often-studied circular and planar jets (e.g. Crow & Champagne 1971; Rockwell 1972; Becker & Massaro 1968). Numerical studies of an isolated elliptic vortex ring (Viets & Sforza 1972; Dhanak & Bernardinis 1981) suggest that the ring is inherently unstable due to the azimuthal variation of self-induction. The advection velocity of a local segment of a curved vortex filament is along its binormal (i.e. normal to the plane of the segment) and is proportional to its curvature (Arms & Hama 1965; Batchelor 1967). Consequently, a segment with a greater curvature moves faster than a segment with a smaller curvature. An elliptic vortex ring thus moves in such a way that it neither retains its shape nor remains in a plane (unlike a circular ring), but deforms such that after a time the two axes are interchanged (although it never repeats exactly (Bridges, private communication)). This process of switching of axes would continue periodically and persist indefinitely, were it not for the fact that vortex rings undergo breakdown (due to azimuthal instability) and decay (due to viscosity and shedding of vortical fluid).

In an elliptic jet, vortical ring structures deform somewhat like isolated elliptic vortices; however, the situation is more complex because of shear, entrainment, development of azimuthal instability and interactions such as pairing, tearing and even cross-linking. Moreover, longitudinal vortices (i.e. rib substructures) between successive structures and their coupling with the latter quite probably make the evolution, interaction and breakdown of a structure in a jet different from those of an isolated vortex.

Variation of θ_e

An elliptic jet is more complex than either plane or circular jets because of its two geometric dimensions: the major and the minor axes; these are in addition to the initial momentum thickness – an intrinsic lengthscale of any shear flow and thus also of a jet near field. Unlike circular or plane jets, the exit momentum thickness of an elliptic jet (issuing from a contoured nozzle) varies around the exit perimeter, having effects in addition to those due to non-uniform curvature. We will define a new lengthscale – the equivalent diameter D_e – and show that it can adequately characterize the jet behaviour. D_e is defined as the diameter of a circular jet with a momentum flux equal to that of an elliptic jet of exit semi-major and semi-minor axes a and b respectively, i.e. $D_e \equiv 2(ab)^{\frac{1}{2}}$.

Cut-and-connect

Flow visualization studies of isolated elliptic vortices in our laboratory (Oshima, private communication) revealed that above a certain aspect ratio (~ 3.5), the self-induced deformation of an isolated elliptic vortex is so severe that the two ends (along the initial major axis) of the vortex come in contact with each other. This results in cross-linking of vortex lines owing to viscous cross-diffusion. When this happens, the single vortex ring is split into two vortex rings. Similar bifurcations occur in elliptic jets also (discussed later). The jet aspect ratio thus represents a criterion for bifurcation of coherent structures. (Recent relevant studies of the cross-linking mechanism (Melander & Hussain 1988; Kida, Takaoka & Hussain 1989) will be discussed in §6.2.)

It has been suggested (Hussain 1983; Takaki & Hussain 1985) that a similar cross-linking of vortex filaments (termed by them as *cut-and-connect*) is responsible for the generation of smaller-scale structures (thus enhanced small-scale mixing) as well as generation of significant aerodynamic noise in the transitional region of a jet. This phenomenon presumably occurs in planar or circular jets in a spatially random fashion after the secondary (azimuthal) instability sets in. Under proper excitation, cut-and-connect interaction in elliptic jets can perhaps be stabilized to occur periodically at a fixed location. Stable bifurcation of an elliptic jet, if possible, thus offers an attractive means of studying experimentally the detailed physics of the cut-and-connect process by using phase-locked measurement techniques (combined with the alignment of successive realizations via iterative cross-correlation).

Literature review

Crighton (1973) studied the instability of a high-aspect-ratio elliptic shear layer. Morris (1986) extended the analysis to cover lower aspect ratios. Their results revealed that, unlike the shear layer of a planar or a circular jet, an elliptic shear layer is characterized by four basic instability modes. Some preliminary results of our study of elliptic jets were summarized earlier (Husain & Hussain 1983) and further details of the results presented here were documented by Husain (1984). Ho & Gutmark (1987) studied the time-average properties of an elliptic jet of aspect ratio 2. The far-field noise characteristics of low-subsonic elliptic jets and their connection with large-scale elliptic vortical coherent structures in the jet near field have been addressed by Bridges (1984) and Bridges & Hussain (1987).

Other motivations

Many practical jet flows are of irregular shapes, such as rectangular, square, triangular and cross. Studies in our laboratory (Toyoda, private communication) revealed that switching of axes similar to elliptic jets also occurs in other jets (for example, in the head-on view, the vertices of an equilateral triangle become the midpoints of the flat sides, and vice versa, as if the triangle is rotated by 60° in its plane; in square jets, the deformation gives the appearance of a 45° rotation of the square-shaped vortical rings). (The coherent structure dynamics in these jets are complicated, particularly owing to intense self-induction at sharp corners, and the resulting cross-linking and fine-scale mixing there.) Among irregular jets, an elliptic jet is less complex and better defined because of the smooth variation in the azimuthal curvature. Thus, an elliptic jet may lead the way to the understanding of other irregular jets. Furthermore, the large-scale structures near or downstream of the end of the potential core of a circular jet are instantaneously neither axisymmetric

nor do they remain in a plane; rather, a large spanwise variation arises owing to the formation of lobes because of azimuthal instability. By studying the near field of elliptic jets, the effects of non-uniform spanwise curvature on the dynamics of coherent structures and their interactions can be understood. This way, elliptic jet studies are relevant to all jets.

Considering practical applications, elliptic jets provide a capability to control turbulence via both passive and active means. Consider the motion of an elliptic vortical structure. As the major-axis side shrinks, it brings in ambient fluid toward the jet centreline and, simultaneously, jet fluid is carried outward on the minor-axis side as this side moves outwards. The elliptic structures thus act as pumping devices to mix ambient and core fluids. Because vortex lines in a viscous flow are not material, and vortical fluid is always shed from the ring (Maxworthy 1974), this pumping action alone would produce higher mixing in elliptic than in circular jets. As discussed later, this effect can be augmented dramatically by employing proper excitation and thus has important technological implications.

This paper addresses the general characteristics of elliptic jets, including time-average measures and instantaneous flow structures. Parts 2 and 3 address the dynamics of vortex pairing and preferred mode coherent structures.

Following description of air and water flow facilities and procedures (§2), we discuss the initial conditions, particularly emphasizing the need for their careful documentation (§3). We then address initially laminar jets, explaining time-average spread and decay in terms of elliptical vortical structures (§4). The instability of the shear layer and the effect of azimuthal variation in θ_e is discussed in §5. In §6 we explain how shear-layer and jet-column modes are identified and how the excitation level affects jet bifurcation and mixing. Finally, time-average profiles of mean and turbulence measures are discussed in §7. Effects of aspect ratio, studied by orifice nozzles, are discussed in the Appendix.

2. Experimental facilities and procedures

2.1. *Air jet*

Hot-wire measurements were made in a variable-speed air jet facility, to which nozzles of different sizes and shapes were attached. The facility, consisting of two settling chambers connected in tandem, is schematically shown in figure 1(*a*). A flexible rubber coupling connects the tunnel to a d.c. motor-driven centrifugal blower, isolating blower vibrations. The flow from the blower passes through a silencer box, a 10° conical diffuser, and a 5.08 cm deep honeycomb (hexagonal cells, 3.2 mm cell size) before entering the first settling chamber. The flow then passes through a 7.62 cm contraction and a 6° conical diffuser to the second settling chamber, and then through five screens (mesh size 1.41 mm and screen wire diameter 0.178 mm) before exiting through an elliptic nozzle into a large laboratory with controlled temperature, humidity and ambient draft.

Many of the experiments required carefully controlled excitation of the jet flow. A loudspeaker attached to the first settling chamber induces organ-pipe resonance in the settling chamber, producing longitudinal plane-wave excitations at the jet exit. The cavity in front of the loudspeaker is covered with a perforated contoured plate so that the settling chamber wall is uninterrupted. The second settling chamber in the tunnel eliminates any possible asymmetry induced by the speaker arrangement in the first chamber. The facility as described, but with a circular nozzle, produced axisymmetric distributions of mean and fluctuating velocity profiles downstream of

the nozzle. The exit-plane velocity perturbation induced by the speaker arrangement is sinusoidal, with negligible harmonic content.

Because the elliptic jet cross-section switches axes, one needs to remove the ambiguity about referring to local major and minor axes of elliptic jets. Thus, we define *major plane* and *minor plane* to denote the reference planes at the nozzle exit; i.e. they are the planes passing through the exit major axis and minor axis respectively. This study used contoured elliptic nozzles of aspect ratios 2 and 4, both with an equivalent diameter $D_e = 5.08$ cm, and had a contraction ratio of 25:1 (from a circular to an elliptic cross-section over a length of about $1.2D_i$, where $D_i = 25$ cm, the inlet diameter). The contraction profile of the nozzle follows a third-order polynomial curve with short straight portions on both upstream and downstream ends. Figure 1 (*b*) shows the nozzle contour shape and the coordinate system. Table 1 gives details of the nozzles.

Data were obtained with standard single and X-type hot-wires (4 μm tungsten) at an overheat ratio of 1.4, using linearized constant temperature anemometers (DISA). A laboratory minicomputer (HP 2100) was used for probe traverse control (with a resolution of 0.0025 cm), data acquisition, and on- and off-line processing. Analog signals were transmitted to a 12-bit A/D converter through cables designed to eliminate signal attenuation and distortion. Power spectra of the velocity signals were obtained using a real-time signal analyser (Ono Sokki CF-920).

All experiments involving hot-wire measurements in unexcited jets (§§4, 7.1 and 7.2) were performed at an exit velocity of $U_e = 29.26$ ms^{-1}; this corresponded to a Reynolds number ($Re_{D_e} = D_e U_e/\nu$) of 10^5. Data presented in §7.3 were obtained at $U_e = 10$ ms^{-1}. Because of the resonance frequency limitation of the excitation system, the instability studies (§5) had to be done at different exit velocities, namely, 18.28 ms^{-1} for the 2:1 jet (N1) and at 15.24 ms^{-1} for the 4:1 jet (N2). For the same reason, the effects of strong excitation at the preferred mode frequency (§6) were studied at $U_e = 20.5$ ms^{-1}. We use equivalent diameter D_e in defining jet Reynolds number because, as will be shown in this paper, D_e is the appropriate lengthscale for elliptic jets.

To cover the streamwise range up to $x = 100D_e$, data were taken with two hot-wire calibrations: one for $0 \leqslant x \leqslant 30D_e$ and another for $30 \leqslant x/D_e \leqslant 100$, thus assuring better utilization of the dynamic range of the A/D converter.

2.2. *Water jet*

A submerged water jet facility (figure 1*c*) was used for flow-visualization studies. A constant head supply tank upstream of the contraction nozzle maintains the flow rate at a prescribed value; two fine-mesh screens (mesh size 0.78 mm and screen wire diameter 0.125 mm) were placed in the settling chamber to minimize upstream disturbances. A contoured nozzle of contraction ratio 25, length $1.5D_i$ and an exit aspect ratio of 2 had provision for boundary-layer suction through a narrow slit all along the nozzle perimeter at 2 cm upstream of the nozzle exit. The boundary-layer suction slot terminated into a header, which connected to an exhaust line through eight equally spaced holes (shown in figure 1*d*). This allowed independent control of the exit momentum thicknesses on the major- and minor-axis sides.

To visualize the flow, a fluorescent dye (uranamine) at a low concentration seeped through a second narrow slit all along the nozzle perimeter, about 1 cm upstream of the exit plane (figure 1*d*). The dye was supplied at a head such that it did not disturb the boundary layer. A cylindrical lens flared a beam of light from a 12 W Ar-ion laser into a thin sheet to illuminate the plane of interest of the flow field. Alternatively,

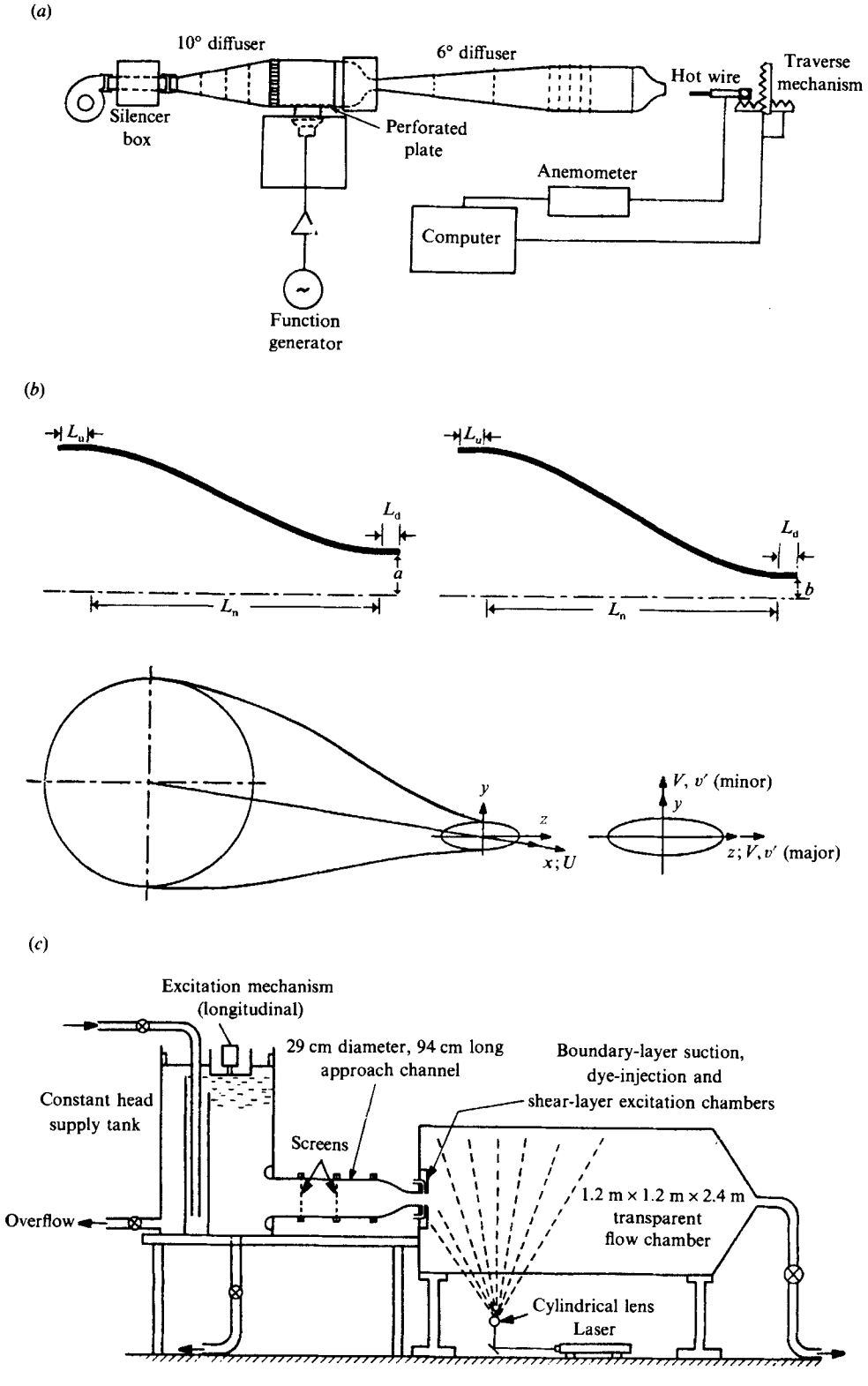

FIGURE 1 (*a–c*). For caption see facing page.

(*d*)

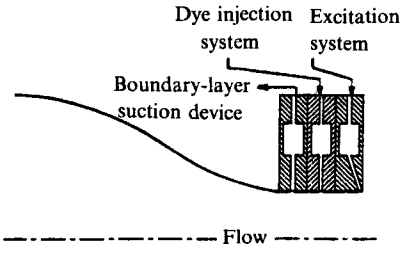

(*e*)

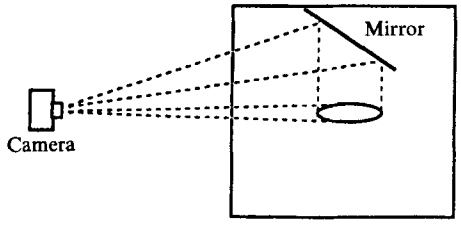

FIGURE 1. (*a*) Schematic of the air jet facility and measurement scheme. (*b*) Nozzle contour shape and coordinate system; L_n is the nozzle length; L_u, L_d are lengths of straight portions at the upstream and downstream ends of the nozzle. (*c*) Schematic of the water jet facility. (*d*) Details of the boundary-layer suction, dye-injection and excitation methods. Total length of the straight section added by the three slots is 3 cm. (*e*) Flow visualization arrangement for capturing two views simultaneously (see figure 5*b*).

Nozzle	Type	Aspect ratio	D_e	Exit condition
N1	Contoured	2:1	5.04 cm	Laminar boundary layer, uniform θ_e
N2	Contoured	4:1	5.04 cm	
N3	Contoured	2:1	5.04 cm	Laminar boundary layer, large θ_e variation
N4	Contoured	2:1	5.04 cm	Turbulent boundary layer, uniform θ_e
N5	Orifice	3:2	2.54 cm	Laminar (virtually zero momentum thickness)
N6	Orifice	2:1	2.54 cm	
N7	Orifice	4:1	2.54 cm	
N8	Orifice	6:1	2.54 cm	
N9	Orifice	8:1	2.54 cm	

Nozzle	L_u (cm)	L_n (cm)	L_d (cm)
N1	2.54	33	2
N2	2.54	29	2
N3	2.54	36	2.54
N4	2.54	29	2

TABLE 1. Characteristics of elliptic nozzles used

a biconvex lens was used to produce a cone of light when the whole jet was visualized. The evolution and interactions of coherent structures were also studied simultaneously in the major and minor planes by placing a mirror at an angle of 45° with the minor plane (figure 1*e*). The mirror was sufficiently far away from the jet axis that it did not interfere with the jet flow.

Flow visualization was done at a jet exit velocity of 0.45 ms^{-1}. To study the effects

of controlled perturbations, the shear layer was excited in the jet exit plane through a third slit of 0.5 mm width (figure 1*d*) using an electromagnetic shaker. The sinusoidal motion of the shaker actuated a piston in a cylinder containing water. The cylinder connects to the outer perimeter of the shear layer excitation chamber through four tubes. Thus, the sinusoidal perturbation is transmitted through water from the cylinder to the excitation chamber and finally to the nozzle boundary layer.

3. Initial condition: contoured nozzles

It is well known that the initial condition or the state of the entry flow (i.e. the profiles of mean and r.m.s. fluctuations of longitudinal velocity, and spectral characteristics of the boundary layer in the jet exit plane) plays an important role in the development of shear layers (Bradshaw 1966; Foss 1977; Hussain & Clark 1977). For criteria to characterize the initial condition in jets and shear layers see Hussain (1980). We concentrated on the two well-defined asymptotic initial boundary-layer conditions – namely, the *laminar* and *fully developed turbulent* states – and their effects on the evolution of elliptic shear layers.

Azimuthal variation of θ_e

In general, elliptic jets issuing from contoured nozzles have a large variation in the momentum thickness θ_e of the boundary layer along the nozzle exit perimeter because in the transition from circular to elliptic cross-section, the wall lengths and curvatures are different in the major and minor planes. In addition to the effects of non-uniform shear-layer curvature, there are effects of θ_e variation on the shear-layer evolution because of the resulting variation in the vorticity of the rolled-up structures. To address the effects of the elliptic geometry alone – free from the additional effects of azimuthal variation in θ_e – considerable effort was devoted to make nozzles with constant θ_e. Iterative recontouring of nozzles enabled us to produce a laminar boundary layer with a constant θ_e all along the exit perimeter for each of the two nozzles of aspect ratios 2 and 4 (nozzles N1 and N2 respectively). Nozzle N3 was used to investigate the additional effect of a large θ_e variation on the shear-layer instability and on the jet evolution; this is a typical elliptic nozzle with no extra effort to control θ_e, and it had a 55% variation in θ_e between the two axes (thicker in the major plane).

A sandpaper ring was used in the nozzle N4 (aspect ratio 2), attached upstream of the exit in order to trip the boundary layer. The width of the ring was judiciously varied azimuthally so that it produced a nearly fully developed turbulent boundary layer with a constant θ_e all along the exit perimeter. With this nozzle, we thus investigated the effect of ellipticity on the evolution of a jet with an initially turbulent boundary layer. All four nozzles (N1, N2, N3 and N4) were of the same exit area so that the jet exit momentum fluxes were virtually the same (varying by 0.56% between the laminar and turbulent cases).

Laminar exit condition

Detailed exit velocity profiles were measured at four locations, viz. in the major and minor planes of the elliptic cross-section. No noticeable peak in the u-spectra (not shown) was observed either in the boundary layer or in the free stream. For nozzles N1, N2 and N3, the boundary-layer profiles (figure 2*a–c*) agree very closely with the Blasius profile and have shape factors close to 2.59. The lines through the mean velocity data (left-hand ordinate) in figure 2(*a–c*) denote the Blasius profile. At

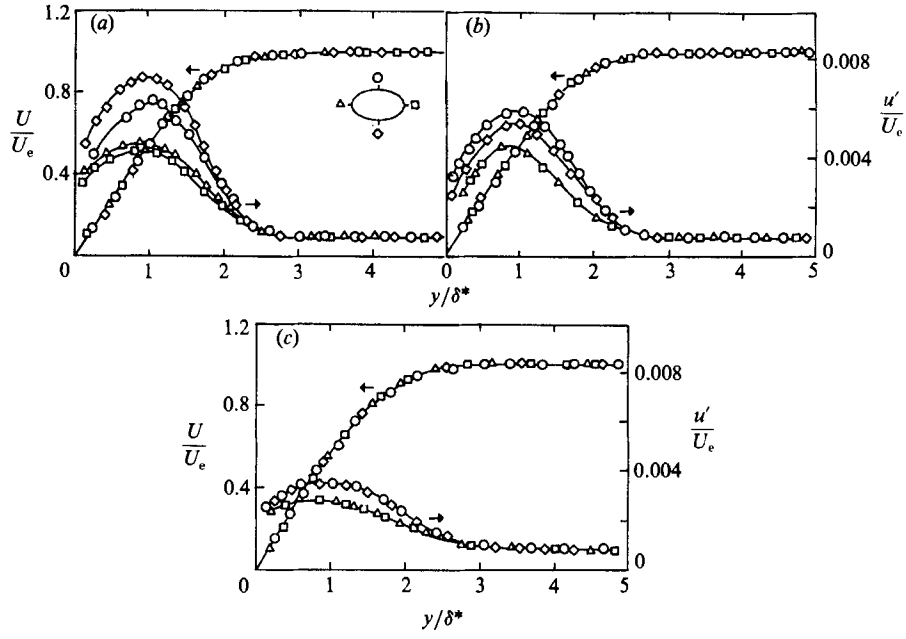

FIGURE 2. Profiles of longitudinal mean and r.m.s. fluctuation velocities in the nozzle exit boundary layers: (*a*) nozzle N1; (*b*) nozzle N2; (*c*) nozzle N3. δ^* is the displacement thickness; $D_e = 5.08$ cm; $U_e = 29.26$ ms^{-1}. Symbols identify locations in major and minor planes as indicated in (*a*).

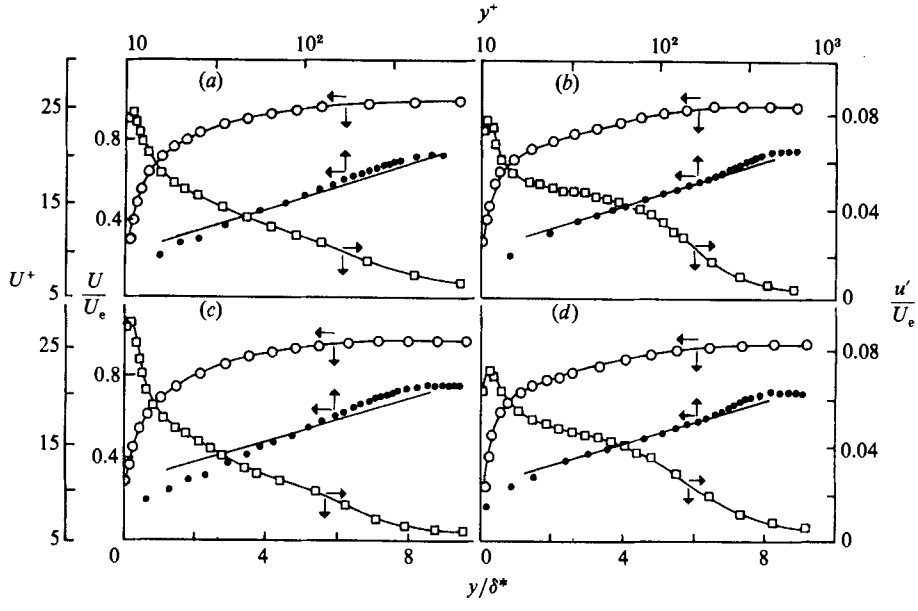

FIGURE 3. Profiles of longitudinal mean (U, U^+) and r.m.s. fluctuation (u') velocities in the boundary layers of initially turbulent jet (nozzle N4): (*a*) and (*c*) are in the major plane; (*b*) and (*d*) are in the minor plane. ○, U/U_e; □, u'/U_e; ●, U^+. $D_e = 5.08$ cm; $U_e = 29.26$ ms^{-1}. Note that the y^+-axis relates to U^+ data only. Solid line represents $U^+ = 5.6 \log_{10} y^+ + 4.9$.

$Re_{D_e} = 10^5$, θ_e values among these four locations were within 2% (of 0.124 mm) for nozzle N1 and 3% (of 0.083 mm) for nozzle N2. The profiles of the longitudinal velocity fluctuation u' at these four sections show the expected variations with peaks at $y \sim \delta^*$ (Hussain 1980) before decreasing monotonically to the free-stream value of about 0.08%. In all the three nozzles (N1, N2 and N3) the peak turbulence intensity in the boundary layer is higher in the minor plane than in the major plane. This is probably due to incipient separation and reattachment on the nozzle wall caused by the higher contraction of the nozzle along the minor plane. Nozzle N3 was longer than N1 and N2 and shows lower turbulence intensity peaks, presumably due to a reduced extent of incipient separation on the nozzle wall. Note that an absolute symmetry of the turbulence intensity profile across the centreline, realized in nozzle N3, could not be achieved in nozzles N1 and N2, which were recontoured to make θ_e constant along the entire perimeter. Attempts to improve the symmetry of u' further produced a greater variation in θ_e. Matching θ_e was considered to be more critical, and thus N1 and N2 represent the best compromises that could be achieved. The data demonstrate that boundary layers agreeing with the Blasius profile can nonetheless have varying extents of superposed fluctuations.

Turbulent exit condition

For the tripped nozzle (N4), the variation in the exit momentum thickness θ_e among the four reference locations was 1.5% (of 0.41 mm). Figure 3(*a–d*) shows the profiles of exit boundary layer mean velocity (U/U_e *vs.* y/δ^* and U^+ *vs.* y^+) and longitudinal fluctuation intensity (u'/U_e *vs.* y/δ^*). The friction velocity u^* required to compute U^+ and y^+ from $U(y)$ data was determined by the Clauser cross-plot technique. On the basis of the longitudinal mean velocity and fluctuating intensity profiles (figure 3), and broadband, smooth u-spectra (not included), the exit boundary layer was inferred to be fully developed turbulent. The mean velocity profile had a shape factor of 1.4. For comparison, the universal relation for flat plate boundary layers (Coles 1962), viz. $U^+ = 5.6 \log_{10} y^+ + 4.9$, is shown by solid lines. The logarithmic regions are distinct and agree with this equation better in the minor plane than in the major plane. Also, note that the wake region is better defined in the minor plane. The turbulence intensity profiles show good symmetry. The boundary layer in the exit plane cannot be truly of a flat plate type, in spite of the straight portions at the nozzle ends. A longer straight portion would produce a more developed boundary layer, but the resulting thicker layer would make the jet exit profile depart from top-hat. And because of the different spanwise curvatures in the major and minor planes of the nozzle, minute profile differences observed between the two reference planes are not unexpected.

The jet excitation level was kept at $u_e'/U_e = 1$ and 2.5% for the shear-layer and jet-column instability studies respectively. For the latter case the level was required for stable jet response. Excitation did not change the mean characteristics of the exit boundary layer. This is a reminder of the fact that the mean velocity profile cannot uniquely identify the state of a boundary layer; one must examine and document in detail the turbulence characteristics as well (Hussain 1980).

4. Jet spread and decay: initially laminar jet

Since the initial instability and generation of vortical structures are clearer in an initially laminar jet, we focus our attention on this case first in order to understand

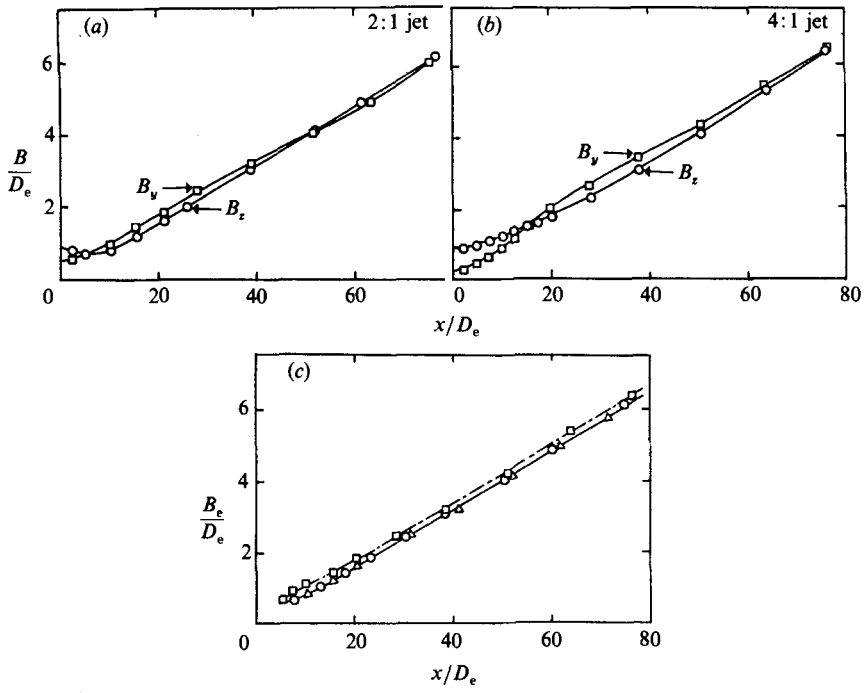

FIGURE 4. Widths of unexcited jets: (*a*) 2:1 jet (N1); (*b*) 4:1 jet (N2). ○, major plane (B_z); □, minor plane (B_y); (*c*) Equivalent jet width $B_e = (B_y B_z)^{\frac{1}{2}}$ of elliptic and circular jets. △, 2:1 jet (N1); □, 4:1 jet (N2); ○, circular jet (initially laminar, top-hat velocity profile; $D = 5.08$ cm). $D_e = 5.08$ cm for elliptic jets; $U_e = 29.26$ ms^{-1} for all jets.

the flow physics in terms of coherent structures. The initially turbulent case will be compared with the laminar case and discussed (along with its other time-average measures) in §7.

4.1. *Jet width*

The streamwise variations of the jet half-widths in the minor and major planes (B_y and B_z respectively), non-dimensionalized by the equivalent diameter D_e, are shown in figure 4(*a*, *b*) for jets N1 and N2. The jet half-width is defined as the transverse distance from the jet axis to the location where the mean velocity $U(x, y)$ is half of the centreline value $U(x, 0)$. Initially, the jets spread at a much higher rate in the minor plane than in the major plane, causing the axes of the elliptic cross-section to switch (i.e. its major axis becomes the minor axis so as to appear rotated in its plane by 90°) at some downstream location(s). Where the jet half-widths in both planes become equal before rotation can be detected is defined as a *switchover* location.

Equivalent jet width

Although the jet width in each of the reference planes exhibits a nonlinear variation with x, the equivalent jet half-widths, defined as $B_e = (B_y B_z)^{\frac{1}{2}}$, shows nearly linear spread in both jets for $x \geqslant 10 D_e$ (figure 4*c*). Circular jet (initially laminar with top-hat velocity profile) spread data, included in this figure for comparison, are closer to that of the 2:1 elliptic jet than the 4:1 jet, as expected. The agreement of the spread rate of the elliptic jet (when non-dimensionalized by D_e)

with that of the circular jet suggests that D_e is a proper choice of lengthscale in moderate aspect ratio elliptic jets. This will be reinforced by various other jet measures in the rest of the paper.

The most likely mechanism for the switching of axes in a free elliptic jet is the evolutionary dynamics and interactions of elliptic coherent structures. A structure undergoes a systematic deformation by self-induction not unlike an isolated elliptic vortex ring. As a result, the time-average measures also show switching of jet axes. In the present study, the switching of jet cross-section up to $x \approx 100D_e$ is a definite indication of the dominance of elliptic coherent structures even in the far field. Thus, to understand elliptic jet behaviour, it is worthwhile examining the dynamics of elliptic vortex rings.

4.2. *Deformation of elliptic vortices*

Self-induced velocity. Using the local induction approximation (LIA), the self-induced velocity of a curved vortex filament (Arms & Hama 1965; Batchelor 1967, p. 510) is,

$$\boldsymbol{u} = \boldsymbol{b}_n \frac{\kappa}{4\pi\rho} \ln\left(\frac{\rho}{\sigma}\right), \tag{1}$$

where κ is the vortex strength (i.e. circulation), ρ is the radius of curvature, σ is the core radius, and $\boldsymbol{b}_n$ is the local unit vector in the direction of the binormal. The radius of curvature, $\rho = |\boldsymbol{R}'|^3/|\boldsymbol{R}' \times \boldsymbol{R}''| = (b/r)[1+(r^2-1)\sin^2\theta)^{\frac{3}{2}}$, is obtained by substituting the derivatives of the position vector $R(\theta)$ for an ellipse, i.e. $R(\theta) = \boldsymbol{i}a\cos\theta + \boldsymbol{j}b\sin\theta$, of semi-axes a and b. Substitution of ρ into (1) yields, for the self-induced velocities in the major and minor planes of a planar ellipse,

$$\boldsymbol{u}_{mj} = \boldsymbol{b}_n\left(\frac{\kappa}{4\pi}\right)\left(\frac{r}{b}\right)\ln\left(\frac{b}{r\sigma}\right), \quad \boldsymbol{u}_{mn} = \boldsymbol{b}_n\left(\frac{\kappa}{4\pi}\right)\left(\frac{1}{br^2}\right)\ln\left(\frac{br^2}{\sigma}\right), \tag{2}$$

where r is the aspect ratio and subscripts mj and mn denote major and minor planes respectively.

Thus

$$\frac{|\boldsymbol{u}_{mj}|}{|\boldsymbol{u}_{mn}|} = r^3 \frac{\ln(b/\sigma) - \ln(r)}{\ln(b/\sigma) + 2\ln(r)} \sim r^3. \tag{3}$$

The approximation is valid for $r \ll (b/\sigma)$, which is easily satisfied for a slender vortex filament. This differential induction velocity deforms an elliptic vortex during its advection (causing the major-axis ends to move much faster than the minor-axis ends). As an example, the deformation of an isolated elliptic vortex filament, simulated numerically in our laboratory (Bridges, private communication), is shown in two views in figure 5(*a*). Of course, in a viscous vortex, additional effects of viscous diffusion are present.

Flow visualization

The deformation of vortical structures in the 2:1 elliptic jet has been further studied using flow visualization. Figure 5(*b*) shows the deformation as viewed simultaneously from the major plane (top sequence) and minor plane (bottom sequence); figure 5(*c*) shows the front view of the structure. Initially, when an elliptic vortex ring rolls up, the plane of the vortex ring is parallel to the nozzle exit plane. Owing to the higher curvature, the major-axis sides move ahead of the minor-axis sides. In this process, the vortex configuration soon becomes like the seam of a tennis ball. The forward inclination of the major-axis sides forms folds in the initial minor-axis sides. As a result, the induced velocity on the minor-axis sides, now directed outward, increases, and the minor-axis sides move outward. Consequently, the vortex again takes an

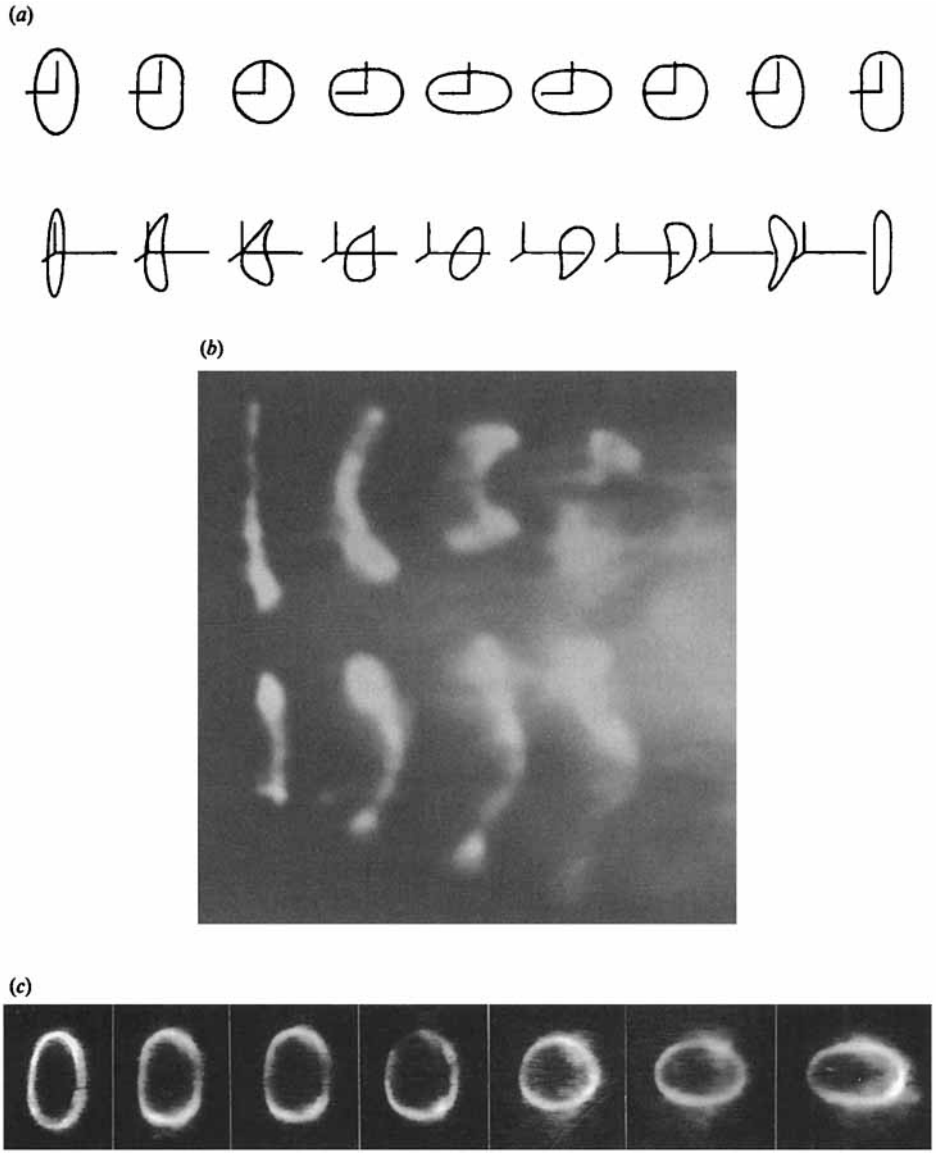

FIGURE 5. (*a*) Deformation of an elliptic vortex ring filament computed by numerical simulation. (*b*) Flow-visualization picture viewed simultaneously normal to the major plane (top) and the minor plane (bottom). (*c*) Flow-visualization picture in a view aligned with the jet axis.

elliptic shape; but now the major axis of the vortex is in the plane of initial minor axis, i.e. the axes have switched. The front view (figure 5*c*) indeed shows deformation of an elliptic shape to a near circle and then to an ellipse again (rotated by 90°).

Flow visualization failed to reveal any clear structure beyond the potential core because of the sudden breakdown of the initial structures and rapid diffusion of the dye. In contrast with the deformation of an isolated inviscid elliptic vortex (Dhanak & Bernardinis 1981), the switching of axes does not continue indefinitely in a jet. Diffusion (viscous as well as turbulent) causes the core radius to increase. The effect of increasing the core radius is to diminish the self-induced velocity (equation (1))

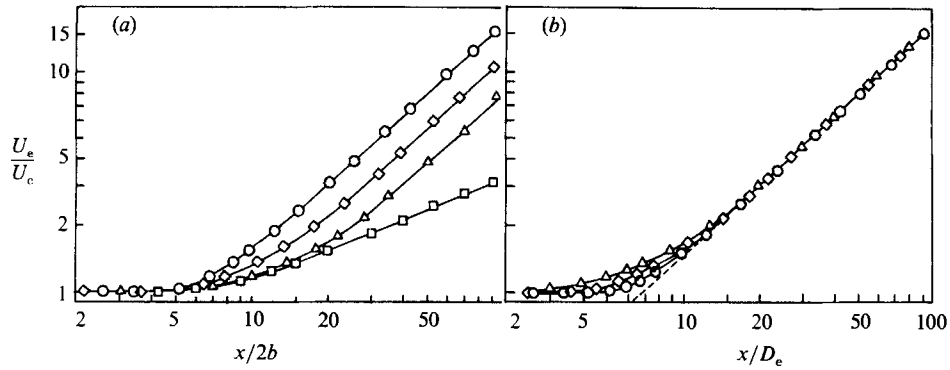

FIGURE 6. Centreline mean velocity of elliptic, circular and plane jets: (*a*) U_e/U_c *vs.* $x/(2b)$; (*b*) U_e/U_c *vs.* x/D_e. ◇, 2:1 jet (N1); △, 4:1 jet (N2); ○, circular jet ($D = 5.08$ cm); □, plane jet (slit width $h = 1.12$ cm, aspect ratio 124); $D_e = 5.08$ cm for elliptic jets; $U_e = 29.26$ ms^{-1} for all jets. Circular and plane jets are also initially laminar with top-hat velocity profiles.

and thus also deformation of elliptic vortical structures in a jet, and delay the axes switching process.

The time-average characteristics of a jet are the manifestations of the dynamics of coherent structures, and their interactions with one another and with incoherent turbulence. Thus coherent structures and vortex dynamics are worthwhile avenues for understanding and controlling various turbulence phenomena such as transports of heat, mass and momentum, and generation of aerodynamic noise and drag, and continue to be the primary approach in our investigations of various turbulent shear flows (see also Parts 2 and 3).

4.3. *Jet decay*

Some researchers (e.g. Trentacoste & Sforza 1967; Krothapalli, Baganoff & Karamcheti 1981) have studied the centreline mean velocity decay of rectangular jets, but no attempt has been made to examine the proper lengthscale which would result in a good collapse of velocity decay data for jets of various aspect ratios. To this end, we have measured the centreline mean velocity decay in elliptic jets (nozzles N1 and N2) as well as in a circular (diameter $D = 3$ cm) and a plane jet (slit width $= 1.12$ cm; aspect ratio $= 124$). The circular and plane jets (as well as the elliptic jets) were initially laminar and had top-hat velocity profiles at the exit plane. Figure 6 shows the centreline mean velocity U_c data as functions of both $x/(2b)$ and x/D_e; here $2b$ is the minimum width at the nozzle exit (i.e. diameter for the circular jet, slit width for the plane jet and minor axis for the elliptic jet). When the axial distance is non-dimensionalized by $2b$, the decay curves show trends similar to data in rectangular jets; i.e. there are three characteristic decay regions (potential core, intermediate, and asymptotic (axisymmetric) decay regions), but the lines for the third region of elliptic jets of various aspect ratios do not collapse. They do when D_e is used as the lengthscale. Both elliptic jets included in figure 6 attain an axisymmetric decay for $x \geqslant 20D_e$, shortly after the first switchover of axes. The virtual origin x_0 obtained by extending the axisymmetric decay line upstream seems to be the same (i.e. $x_0/D_e \approx 6$).

Not unexpectedly, the decay characteristic of the 2:1 elliptic jet is closer to that of the circular jet than is that of the 4:1 jet. The initial mean velocity decay is higher in the 4:1 jet than in the 2:1 jet, because the former has a higher entrainment

surface. Note that the decay shows axisymmetric behaviour farther upstream than shown by the jet widths in both planes (figure 4). Thus the centreline mean velocity is not a good indicator of where an elliptic jet (or in general, an irregular jet) achieves the state of axisymmetry.

Because the formation of elliptical vortical structures is connected with the instability of the elliptic shear layer, we postpone the discussion of other time-average measures of the jet until later (§7 and Appendix), and address next the instability of the shear layer and the jet column.

5. Instability of elliptic shear layers

It is obvious that the instability mechanism in an elliptic shear layer is complicated owing to the non-uniform azimuthal curvature (i.e. owing to aspect ratio) as well as the non-uniform exit momentum thickness θ_e. Thus, two interesting questions are: what is the effect of the aspect ratio on the instability, and how does a shear layer roll up when there is a variation in θ_e? The spanwise variation of θ_e may suggest different streamwise locations of roll-up in the major and minor planes. Instability characteristics were studied by both hot-wire measurements and flow visualization. To eliminate probe interference, a long-pronged probe was used at an angle such that the probe stem remained outside the shear layer and did not induce a shear-layer tone (a phenomenon discussed by us previously).

5.1. *Shear layers of uniform exit momentum thickness*

The instability of elliptic shear layers was investigated under controlled excitation at the natural instability frequency f_n using an excitation level of $u'_e/U_e = 1\%$ measured at the jet exit centreline. Recall that the limited range of the resonance frequencies of the excitation system forced the instability studies to be performed at different exit velocities to obtain the appropriate St_{θ_e}; for example U_e was 18.28 ms^{-1} for the 2:1 jet (N1) and 15.24 ms^{-1} for the 4:1 jet (N2). Corresponding values of f_n and θ_e are 1362 Hz and 0.161 mm for the 2:1 jet and 1160 Hz and 0.158 mm for the 4:1 jet, giving a value of the Strouhal number $St_{\theta_e}(\equiv f\theta_e/U_e) \approx 0.012$ in both cases. The streamwise development of the amplitudes $u'_{\frac{1}{4}f}$, $u'_{\frac{1}{2}f}$, u'_f, $u'_{\frac{3}{2}f}$ and u'_{2f} in the major and minor planes for both jets N1 and N2 are shown in figure 7. These represent the r.m.s. amplitudes of the spectral content of u at frequencies $\frac{1}{4}f$, $\frac{1}{2}f$, f, $\frac{3}{2}f$ and $2f$, where $f = f_n$ is the excitation (i.e. the fundamental) frequency. Also shown is the total r.m.s. velocity u'_t. The spectral development of u, being qualitatively similar for both jets, is shown in figure 8 for only the 2:1 jet (N1). These quantities were measured along a line where u'_f was the maximum across the shear layer. This line approximately coincides with the $U/U_e = 0.7$ line.

Growth of the fundamental wave

In all the cases (i.e. 2:1 and 4:1 jets; major and minor planes) the growth pattern of spectral components are quite similar to those for an axisymmetric mixing layer (Zaman & Hussain 1980). The fundamental u'_f grows exponentially up to $x/\theta_e \approx 45$ essentially following the total turbulence intensity u'_t. The fundamental's growth is arrested by the growth of the subharmonic. For a given aspect ratio, the fundamental's growth rates are almost the same in both planes. However, with the increase in aspect ratio from 2 to 4, the growth rate of u'_f is decreased. The u'_f evolution farther downstream also shows a difference between the two jets. In the 2:1 jet, following its saturation amplitude, the u'_f hits a minimum in both planes at

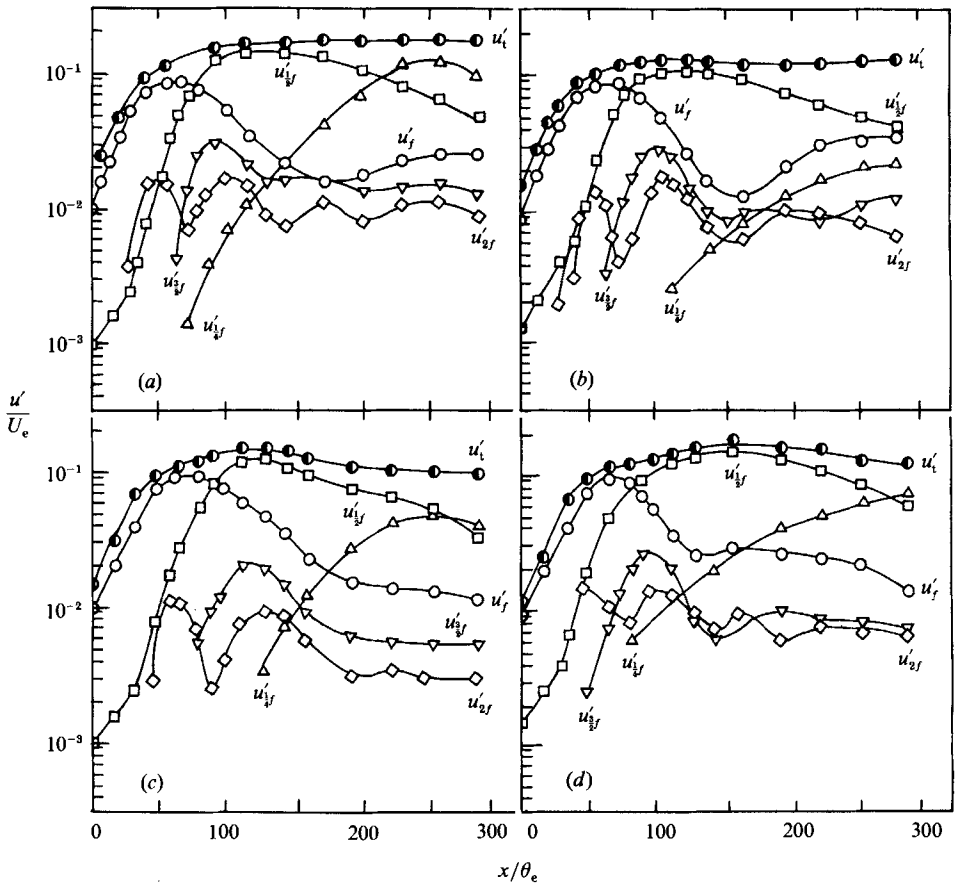

FIGURE 7. Growths of instability modes in elliptic shear layers: (*a*) major plane of 2:1 jet (N1); (*b*) minor plane of N1; (*c*) major plane of 4:1 jet (N2); (*d*) minor plane of N2. △, $u'_{\frac{1}{2}f}$; □, $u'_{\frac{1}{2}f}$; ○, u'_f; ▽, $u'_{\frac{3}{2}f}$; ◇, u'_{2f}; ◐, u'_t. $D_e = 5.08$ cm; $U_e = 18.28$ ms^{-1} and $f = 1362$ Hz for the 2:1 jet. $U_e = 15.24$ ms^{-1} and $f = 1160$ Hz for the 4:1 jet.

$x/\theta_e \approx 150$ before increasing again, reaching a second maximum at $x/\theta_e \approx 300$. There is no such clear minimum in the 4:1 jet.

The trend of decreasing growth rate with increasing aspect ratio has also been suggested by the analysis of Morris (1986). In the present study, the growth rates $-\alpha_1\theta_e$ of the fundamental are 0.063 and 0.044 for the 2:1 and 4:1 jets respectively. The corresponding values obtained by Morris (1986) in his analysis for ce_0 mode (which is analogous to axisymmetric mode) are 0.066 and 0.04. Although these values agree well with Ho & Gutmark (1987) and our data, this agreement is quite surprising. In his analysis, Morris used experimental mean velocity profiles of Gutmark & Ho (1985) at $x/a = 0.5$ and 2. These two locations correspond to $x/(\theta_e)_{mn} = 76$ and 305 respectively, where the fundamental has already saturated, and there is a large variation in momentum thickness between the major and minor planes. Thus, the agreement of the experimental results with the theoretical prediction is unexpected. Parenthetically, why linear stability analysis of the time-mean profile is apparently so successful in a highly nonlinear situation involving large spatial and temporal variations of the profile at scales at which the instability is studied – Morris' analysis being one of many shear flow studies (see Hussain 1983) – continue to remain puzzling.

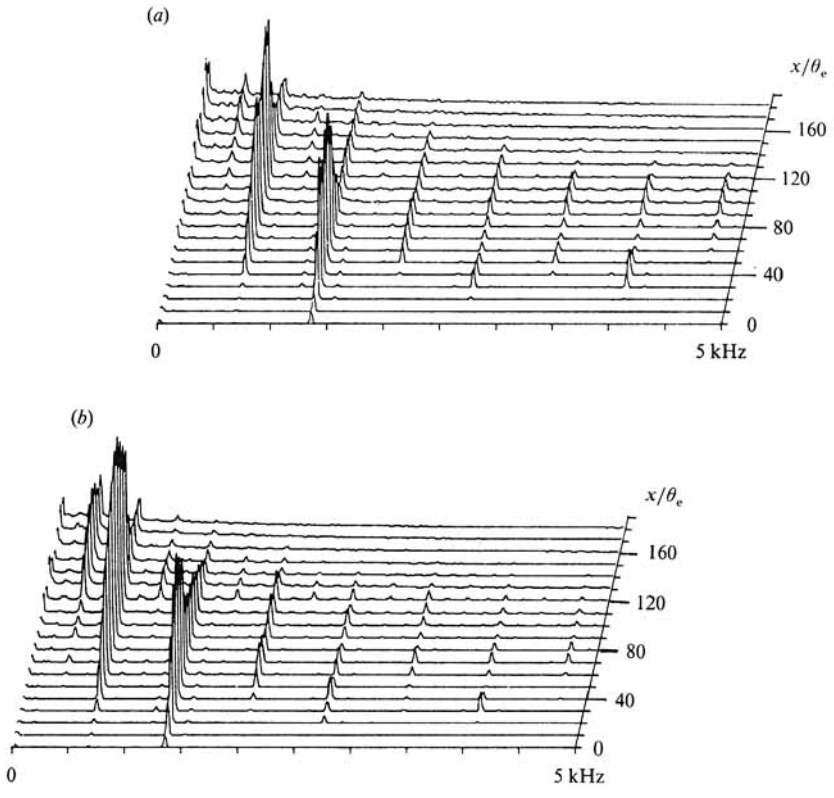

FIGURE 8. Evolution of u-spectrum in the shear layer of the 2:1 (N1) elliptic jet: (*a*) minor plane; (*b*) major plane. $D_e = 5.08$ cm, $U_e = 18.28$ ms^{-1}. Successive traces are for different probe locations in the streamwise direction as indicated in the figure.

There is an area of apparent disagreement between our data and Morris' analysis. Our results show that the fundamental u_f' grows almost at the same rate and also reaches the same saturation amplitude in both major and minor planes; this was observed in both jets (of aspect ratio 2 (N1) and 4 (N2)). Ho & Gutmark's (1987) experimental results also show the same growth rate and saturation amplitude of u_f' in both planes of a 2:1 jet. Morris' analysis, however, predicts the maximum amplitude of (pressure) perturbations in the major plane and a monotonic decay to zero in the minor plane. That is, he predicts amplification to be the maximum in the major plane, but zero in the minor plane.

This apparent disagreement (between the experimental results and the analysis of Morris), regarding the growth rates in the two planes can be reconciled if we examine the azimuthal θ_e variations in these cases. As mentioned earlier, $(\theta_e)_{mj}$ is always greater than $(\theta_e)_{mn}$ in practical elliptic nozzles (recall that in our nozzle N3, $(\theta_e)_{mj}$ is 55% higher than $(\theta_e)_{mn}$), unless extreme care is taken in designing a nozzle with a constant θ_e all around the perimeter (see also §5.2). The present study was carried out using nozzles of constant θ_e (viz. nozzles N1 and N2). In Ho & Gutmark's nozzle, $(\theta_e)_{mj}$ was 25% higher than $(\theta_e)_{mn}$. In Morris' analysis, he assumed $(\theta_e)_{mn}/(\theta_e)_{mj} =$ aspect ratio; i.e. $(\theta_e)_{mn}$ is much thicker than $(\theta_e)_{mj}$ for two cases (aspect ratios 2 and 4) he studied. (Note that this variation in θ_e is opposite to that which occurs naturally in an elliptic nozzle. This is an aside, because the discussion that follows would apply equally even if Morris made the correct assumption of relative θ_e values

between the planes. In that case, he would get exactly the same prediction as the experiments: roll-up to occur in the minor plane first. The contradiction arises because of his unrealistic assumption of large variation of θ_e (twofold and fourfold) and opposite to that in real jets.) The above mentioned studies, involving elliptic shear layers of non-uniform θ_e (including our study of N3, discussed in §5.2), indicate that instability starts in the plane of minimum θ_e. The Strouhal number St_{θ_e} based on the minimum θ_e and the most unstable frequency is about 0.017. The receptive band of unstable frequencies is $0 < St_{\theta_e} \lesssim 0.034$ with zero growth rate at $St_{\theta_e} \approx 0.034$. Thus, for the large θ_e variation he assumed, his results are not surprising. For the 2:1 jet, where he assumed $(\theta_e)_{mn} = 2(\theta_e)_{mj}$, the local St_{θ_e} value corresponding to the most unstable frequency (say f) in the major plane (where θ_e is assumed to be the minimum) falls in the middle of the unstable band, while the local St_{θ_e} value in the minor plane (where θ_e is assumed to be the maximum) corresponding to f and $(\theta_e)_{mn}$ falls at the upper end of the unstable band; this is why his growth rate in the plane of $(\theta_e)_{mn}$ is zero. For the 4:1 jet where he assumed $(\theta_e)_{mn} = 4(\theta_e)_{mj}$, the growth rate in the minor plane is obviously zero because St_{θ_e} there is far outside the unstable band.

In practical flows, however, the shear layer in the plane of the maximum θ_e cannot maintain zero perturbation growth, as predicted by the theory, forever. The flow in this plane becomes unstable at a downstream location presumably by azimuthal propagation of roll-up (addressed in §5.2).

Growth of the subharmonic and higher harmonics

Both linear and nonlinear theories give insight into relative amplifications of u'_f and $u'_{\frac{1}{2}f}$. Initially, the subharmonic component $u'_{\frac{1}{2}f}$ grows exponentially at a low rate, consistent with the (linear) Kelvin–Helmholtz instability. The fundamental u'_f grows in x as the shear-layer thickness also increases (so does St_{θ_e}); thus the growth rate of u'_f decreases but that of $u'_{\frac{1}{2}f}$ increases. Where u'_f becomes neutral, the growth rate of u'_f becomes about the maximum. Now, considering nonlinear instability, as u'_f grows to a critical amplitude, $u'_{\frac{1}{2}f}$ is able to extract energy from the former and to grow at a higher rate. This arrests the growth of u'_f, producing its saturation. Near the saturation location of u'_f (viz., $x \approx 45\theta_e$), $u'_{\frac{1}{2}f}$ starts growing at a higher rate. The enhanced growth of $u'_{\frac{1}{2}f}$ is the result of the nonlinear resonant interaction between the fundamental and the subharmonic; the interaction produces an $\frac{1}{2}f$ component, thereby reinforcing the subharmonic (Kelly 1967; Monkewitz 1988). Of course, the nonlinear interaction produces higher harmonics of u'_f and $u'_{\frac{1}{2}f}$ also through self- and cross-interactions (figures 7 and 8), but not resonantly.

Physically, the saturation of the fundamental corresponds to the roll-up of vortices. Near this saturation, the appearance of the resonantly growing subharmonic is due to the pairing of two neighbouring vortices. Saturation of the subharmonic indicates the completion of the pairing process. The higher harmonics of the fundamental and of the subharmonic are the manifestations of the distortion of the vorticity field during roll-up and subsequent pairing interactions; the u'_{2f} peaks are caused by nonlinear saturation (i.e. steepening of waves) of u'_f and $u'_{\frac{1}{2}f}$. Note that the u'_{2f} distribution exhibits a decaying oscillatory behaviour; not surprisingly, the dominant first and second peaks in u'_{2f} are where the fundamental and the subharmonic reach their respective peaks.

The saturation of the subharmonic is in turn associated with the development of the second subharmonic $u'_{\frac{1}{4}f}$ – an example of sub-subharmonic resonance causing second pairing. The maximum amplification of $u'_{\frac{1}{4}f}$ is smaller than $u'_{\frac{1}{2}f}$ in all the cases

except in the major plane of the 2:1 jet. The weaker u'_{1f} is to be expected because at these far downstream locations, the structures are diffuse; further, any jitter in the second pairing location decreases the r.m.s. signal from a stationary probe.

In general, the pairing process of elliptic ring vortices is quite different from those of circular vortices because of the out-of-plane deformation. Prior to the first pairing, the out-of-plane deformation of elliptic vortices is very small (since this pairing occurs soon after planar roll-up). This results in an essentially complete pairing over the entire perimeter as in an axisymmetric or planar shear layer. However, after the first pairing, the out-of-plane deformation is significant and the pairing does not occur along the entire perimeter like in the case of planar vortices. Pairing of elliptic vortices is discussed in detail in Part 2.

5.2. *Effects of non-uniform exit momentum thickness* (2:1 *jet*)

For the jet N3 of aspect ratio 2 with a large variation in θ_e along the exit perimeter (recall that θ_e was 55% greater on the major plane than on the minor plane), the roll-up frequency was found to be the same all around the periphery. The natural roll-up frequency corresponded to $St_{\theta_e} \approx 0.012$ based on the minimum θ_e which occurred in the minor plane, and $St_{\theta_e} \approx 0.019$ on the major plane. To explain how an elliptic shear layer rolls up in the presence of a large spanwise variation in θ_e, we employed flow visualization. The nozzle used for this allowed boundary-layer suction from four sides independently as described in §2.2 (the nozzle is the same as N3 except that it has extra attachments for boundary-layer suction, dye injection and excitation; see figure 1*d*). Using different suction rates in major and minor planes, we have studied the roll-up process of elliptic shear layers for two opposite cases: $(\theta_e)_{mn} < (\theta_e)_{mj}$ and $(\theta_e)_{mj} < (\theta_e)_{mn}$. Here $(\theta_e)_{mj}$ and $(\theta_e)_{mn}$ denote the exit momentum thicknesses in the major and minor planes respectively.

Observations of the laboratory flow, as well as of recorded video films, show the sequence of events fairly clearly; however reproduction loses clarity, takes up a lot of space, and is not equally convincing. In some such situations, illustration by sketches of visualized observations appears unavoidable and even desirable. We include in figure 9(*a*, *b*) two pictures as representative cases; both show views perpendicular to the major plane. Figure 9(*a*) shows the roll-up of the shear layer for $(\theta_e)_{mn} < (\theta_e)_{mj}$ and figure 9(*b*) for $(\theta_e)_{mj} < (\theta_e)_{mn}$. The detailed sequence of events gleaned from laboratory visualization and examination of video films are highlighted by sketches in figure 9(*c*–*f*). In both the cases, the roll-up starts only in the azimuthal plane where the momentum thickness is the minimum. In the *first* case, (i.e. $(\theta_e)_{mn} < (\theta_e)_{mj}$) – the case of typical elliptic jets – the vortex roll-up starts in the minor-axis side. Figure 9(*a*) convincingly shows no roll-up on the major-axis side while roll-up is complete on the minor-axis side (let us call this rolled up vortex element a *spindle*). The roll-up then gradually propagates azimuthally toward the major-axis side, resulting in a complete roll-up of the elliptic ring (figure 9*a*, *c*).

In the *second* case (i.e. $(\theta_e)_{mj} < (\theta_e)_{mn}$), the vortex element rolls up locally only in the major-axis side like a *crescent*, but does not propagate toward the minor-axis side (figure 9*b*, *d*, *e*). Rather, the minor-axis side rolls up independently at a location farther downstream, evidently scaling on the $(\theta_e)_{mn}$. The roll-up process on the minor-axis side propagates toward the major-axis side (similar to the first case), and the rolled-up vortex element (i.e. spindle) joins with the nearest crescent on the major-axis side, resulting in a single, rolled-up vortex ring. Depending upon the ratio $(\theta_e)_{mj}/(\theta_e)_{mn}$, the spindles and crescents adjust their advection speeds in order to enable them to line up and fuse into a single vortex ring. In figure 9(*d*, *e*), the joining

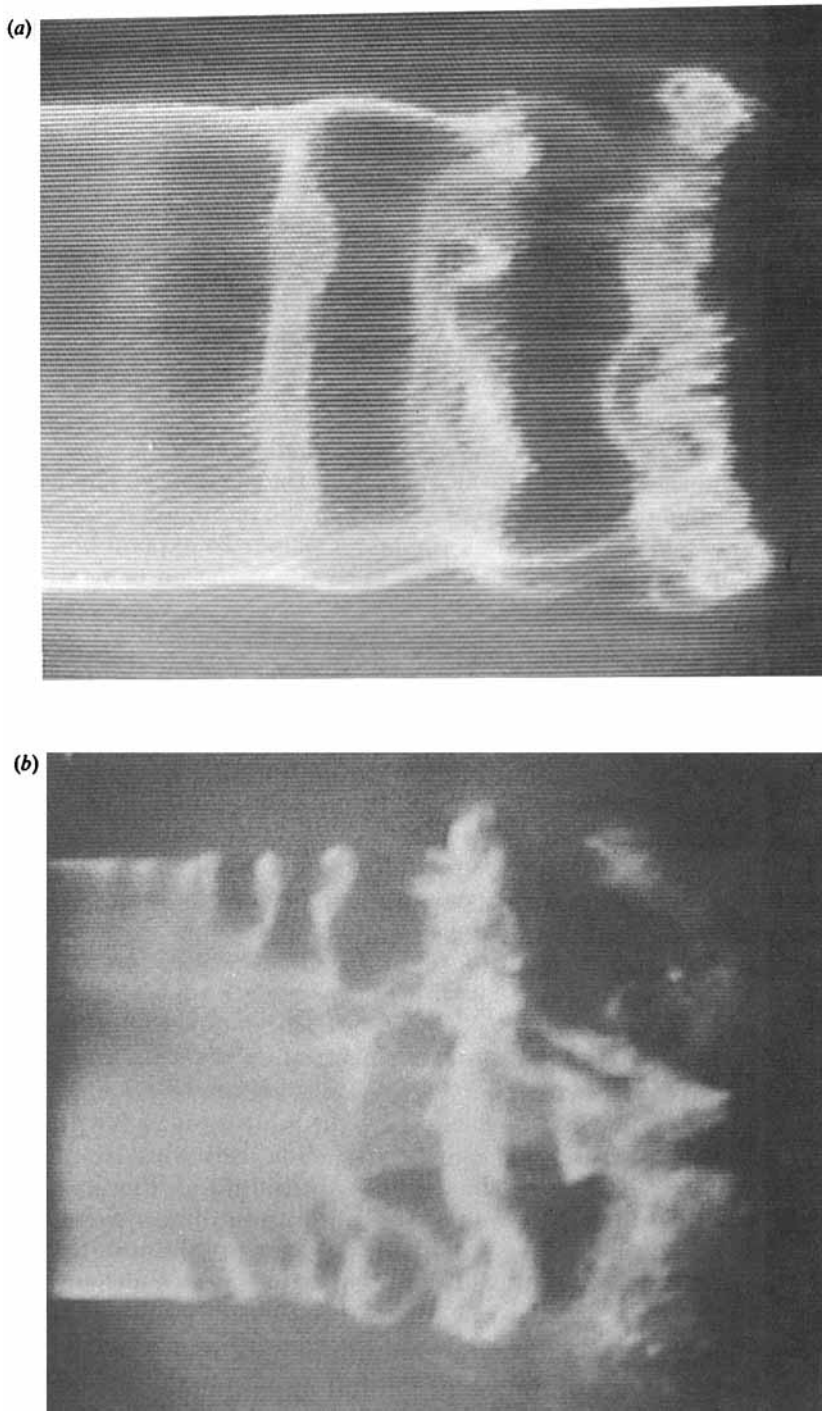

FIGURE 9(a, b). For caption see facing page.

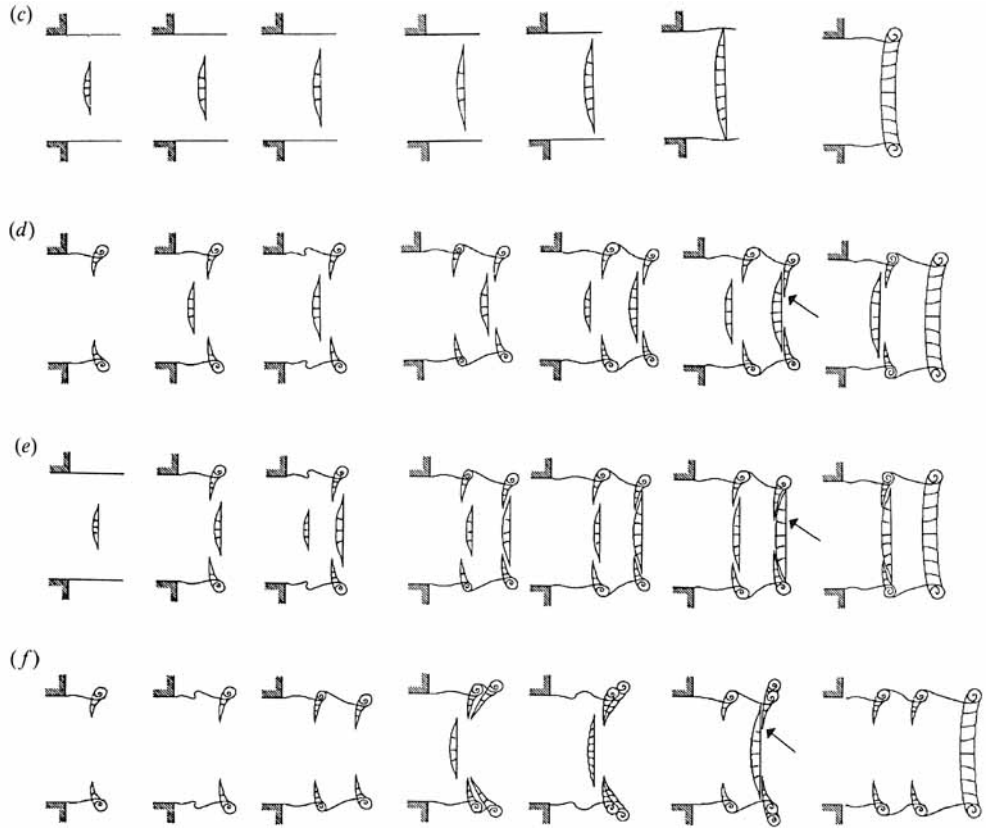

FIGURE 9. Flow-visualization picture, viewed normal to the major plane, showing the roll-up of vortices for (*a*) $(\theta_e)_{mn} < (\theta_e)_{mj}$; (*b*) $(\theta_e)_{mj} < (\theta_e)_{mn}$. (*c*)–(*f*) Schematics extracted from flow visualization of the roll-up process of an elliptic shear layer in the presence of large momentum thickness variations along the exit perimeter; (*c*) for $(\theta_e)_{mn} < (\theta_e)_{mj}$; (*d*, *e*) for $(\theta_e)_{mj} < (\theta_e)_{mn} < 2(\theta_e)_{mj}$; (*f*) for $(\theta_e)_{mn} = 2(\theta_e)_{mj}$.

of the spindles and crescents is marked by arrows. A spindle joins with the neighbouring downstream crescent in figure 9(*d*), but with the neighbouring upstream crescent in figure 9(*e*).

When $(\theta_e)_{mn}$ is almost twice that of $(\theta_e)_{mj}$, the roll-up location on the minor-axis side coincides with the pairing location of the crescents on the major-axis side (figure 9*f*). In this case, the spindle joins with the paired crescent on the major-axis side, again resulting into a single elliptic ring. Similar to the second case above, the paired crescent discussed here can occur either upstream or downstream of the spindle.

In the flow-visualization studies, since we have no measurements of θ_e variations, we cannot quantitatively address the effects of local θ_e and curvature on the instability mechanism. However, from these two opposite cases, i.e. $(\theta_e)_{mj} < (\theta_e)_{mn}$ and $(\theta_e)_{mn} < (\theta_e)_{mj}$, we have concluded qualitatively that the curvature plays an important role in the propagation of the roll-up process of the vortex sheet in the azimuthal direction. This interesting aspect of instability needs more quantitative studies.

The effect of θ_e variation is also evident from the measured jet-width data, shown in figure 10. For comparison, the data for nozzle N1 in both major and minor planes are also included. Since θ_e in the minor plane of both jets (i.e. N1 and N3) are nearly

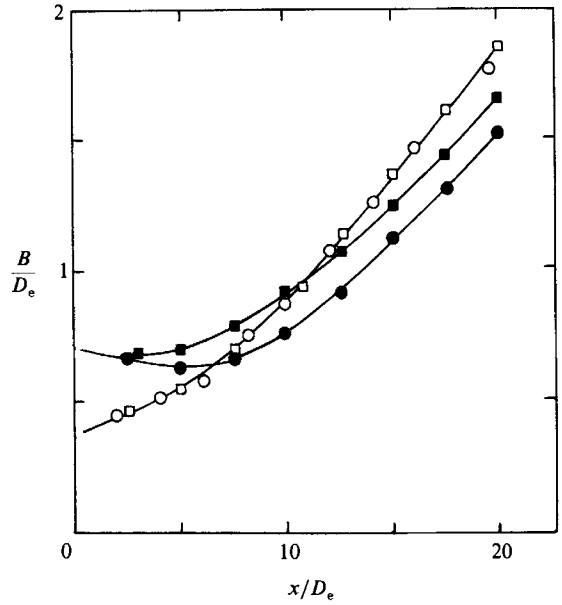

FIGURE 10. Effects of uniform and non-uniform θ_e on jet spread. ○, 2:1 jet with uniform θ_e (N1); □, 2:1 jet with non-uniform θ_e (N3); open symbols for minor plane; solid symbols for major plane. $D_e = 5.08$ cm; $U_e = 29.26$ ms^{-1}.

the same, the vortex in this plane rolls up at nearly the same location. Consequently the jet half-widths of these two jets in the minor plane are also almost the same. In the major plane, recall that θ_e is 55% greater for the nozzle N3; this results in the delay of structure formation in N3. Thus the width in the major plane, instead of decreasing (as in N1), shows no growth up to $x \approx 5D_e$ before it starts increasing. Correspondingly, the axis switchover location moves farther downstream (from $x \approx 6D_e$ to $10D_e$).

6. Behaviour of the jet column under controlled excitation

6.1. *Coherent structure modes*

One of our primary objectives was to investigate whether there are preferred mode coherent structures in the near field and, if so, how these elliptic structures interact. To this end, the jets N1, N2 and N4 were subjected to controlled sinusoidal longitudinal excitation (one frequency at a time). The variation of longitudinal turbulence intensity $u'_c(x)$ along the jet centreline of the 2:1 elliptic jet (N1) is shown in figure 11(*a*) for various Strouhal numbers St_{D_e}. For the unexcited jet, the peak intensity ($\sim 14\%$) occurs at $x \approx 8D_e$. With increasing St_{D_e}, a second peak develops nearer to the jet exit plane ($x/D_e = 2$ to 3) and reaches a maximum at $St_{D_e} \approx 0.85$. In an unexcited jet, the formation, pairing and breakdown of structures do not occur at fixed spatial locations. The spatial jitter of these events produces a broad peak in $u'_c(x)$. Under excitation, however, these events can be essentially localized in space. This can produce a separate, sharper peak in $u'_c(x)$ closer to the exit plane, while the breakdown of structures near the end of the potential core gives rise to the second peak. The fundamental r.m.s. amplitude u'_f variation (figure 11*b*, *c*) shows that it reaches its maximum value at $St_{D_e} \approx 0.4$. Note that at this St_{D_e}, u'_f has also the

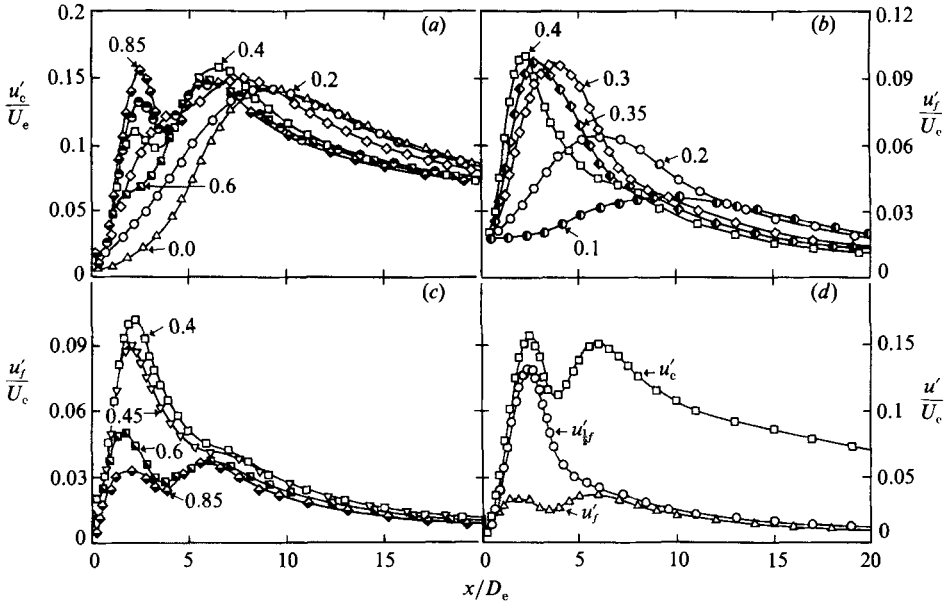

FIGURE 11. Response of the 2:1 initially laminar elliptic jet (N1) to controlled 2% excitation: (*a*) dependence of $u_c'(x)$ on St_{D_e}; (*b*, *c*) dependence of $u_f'(x)$ on St_{D_e}. St_{De} values are: △, unexcited; ◐, 0.1; ○, 0.2; ◇, 0.3; ◆, 0.35; □, 0.4; ▽, 0.45; ◪, 0.6; ◆, 0.85; ◓, 0.9. (*d*) Distributions of $u_c'(x)$, $u_f'(x)$ and $u_{\tilde{f}}'(x)$ at $St_{D_e} = 0.85$. $D_e = 5.08$ cm; $U_e = 29.26$ ms^{-1}.

highest growth rate. For higher or lower values of St_{D_e}, the u_f' peak decreases monotonically. With increasing St_{D_e}, the location of the peak progressively moves upstream, as to be expected. These frequencies being sufficiently away from the shear-layer modes (for example, $St_{D_e} = 0.9$ correspond to $St_{\theta_e} = 0.002$), the shear layer modes – which would produce greater peaks much nearer the nozzle lip – are not excited. Spectral data show that, at $St_{D_e} = 0.4$, u_f' saturates near the peak of u_c' due to the development of higher harmonics. The spectrum revealed no subharmonic, consistent with the fact that this excitation is at the terminal Strouhal number – the dominant frequency near the end of the potential core (Zaman & Hussain 1977, 1980). With further increase in x, the spectral peaks progressively become submerged in the growing broadband, background turbulence.

Preferred mode

Following Crow & Champagne (1971), $St_{D_e} = 0.85$ would have been called the preferred mode, because the total centreline turbulence level u_c' becomes the highest at this St_{D_e}. However, the preferred mode was redefined by Zaman & Hussain (1977, 1980) as that which *produced maximally amplified fundamental amplitude* u_f', rather than the total turbulence level. We conclude that the preferred mode of elliptic jets of moderate aspect ratios is $St_{D_e} \approx 0.4$. Note that the St_{D_e} value of the preferred mode in circular jets has been found to vary somewhat from experiment to experiment in published works. This is not an indication of the lack of universality of either the concept or the St_{D_e} value but merely of the fact that this value depends on the method of determination, as is to be expected. Not only should the preferred mode frequency be determined by using excitations induced at one frequency at a time, but also the location of measurement must be agreed upon. In the case of the latter, the

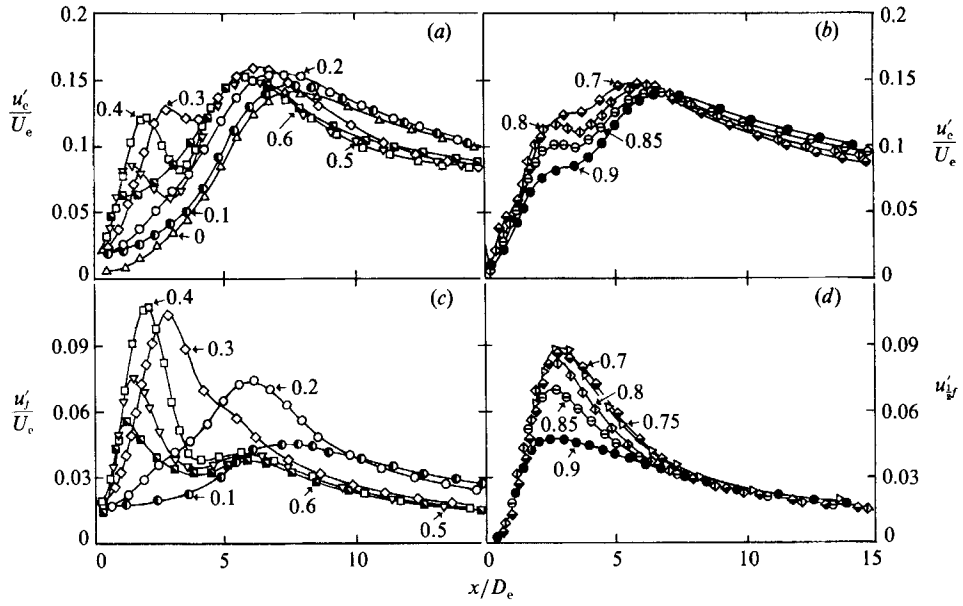

FIGURE 12. Response of the 2:1 initially turbulent elliptic jet (N4) to controlled 2% excitation: (*a*, *b*) dependence of $u_c'(x)$ on St_{D_e}; (*c*) dependence of $u_f'(x)$ on St_{D_e}; (*d*) dependence of $u_{\frac{1}{2}f}'(x)$ on St_{D_e}. St_{D_e} values are: △, unexcited; ◐, 0.1; ○, 0.2; ◇, 0.3; □, 0.4; ▽, 0.5; ◪, 0.6; ◆, 0.7; ▷, 0.75; ◈, 0.8; ⊖, 0.85; ●, 0.9. $D_e = 5.08$ cm; $U_e = 29.26$ ms^{-1}.

spectral peak frequency not only varies in x (typically due to pairing) but also, by as much as threefold, in the radial direction across the mixing region (Hussain 1983).

Jet column pairing mode

Why is u_f' the largest at $St_{D_e} = 0.4$ while the total intensity u_c' is the largest at $St_{D_e} = 0.85$? This is because most of the energy in the second case is in the subharmonic frequency associated with the stable jet column mode of pairing (Zaman & Hussain 1977, 1980). The large intensity on the centreline is the induced footprint of the successive vortex pairing events at the same physical location. Figure 11(*c*) shows that, with increasing St_{D_e} above 0.4, the saturation level of the fundamental decreases. At $St_{D_e} = 0.85$, the fundamental u_f' is very weak but the subharmonic $u_{\frac{1}{2}f}'$ is large because of stable pairing, having a maximum at $x \approx 2.5D_e$ (figure 11*d*). Similar to subharmonic resonance in the shear layer, we can regard this as the subharmonic resonance of the jet column. Farther downstream of the location of the peak in $u_{\frac{1}{2}f}'$, the fundamental shows a slight increase (at $x \approx 7D_e$) owing to the generation of the higher harmonics of the subharmonic during the breakdown process. The second peak at $x \approx 7D_e$ in u_c' in figure 11(*d*) is due to the combined contributions of higher harmonics of the fundamental and of its subharmonics (i.e. $\frac{3}{2}f, 2f, \ldots$, components). The spectrum of u revealed no $\frac{1}{4}f$ component, suggesting no second stage of pairing; visualization studies also showed that only one stage of pairing occurred at this St_{D_e}.

The response of jets N2 and N3 to similar excitations were also found to be similar to that of N1. The preferred mode and the stable pairing mode frequencies for these two jets were also found to be $St_{D_e} = 0.4$ and 0.85 respectively, confirming that the

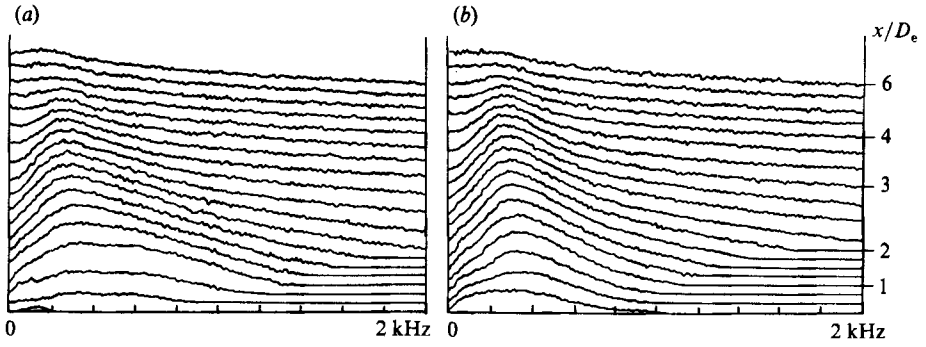

FIGURE 13. Evolution of u-spectrum along the jet centreline in the absence of excitation: (*a*) N1 jet; (*b*) N4 jet. $D_e = 5.08$ cm, $U_e = 29.26$ ms^{-1}. x/D_e values are: 0.25, 0.5, 0.75, 1.0, 1.25, 1.5, 1.75, 2.0, 2.25, 2.5, 2.75, 3.0, 3.25, 3.5, 4.0, 4.5, 5.0, 5.5, 6.0.

jet-column mode is independent of aspect ratio (at least for moderate values) and of non-uniformity in θ_e. The occurrence of the preferred mode and the stable pairing mode for the jet with initially turbulent boundary layer (N4) is further demonstrated in figure 12. The fundamental r.m.s. amplitude distributions are essentially the same as in the laminar case, being the highest at $St_{D_e} = 0.4$, and indicate that equally strong preferred-mode coherent structures are formed in an elliptic jet irrespective of the initial boundary-layer characteristics. This is consistent with the preferred-mode structures in circular jets (Zaman & Hussain 1980). The first peak in u_c' for stable pairing mode excitation, however, is weaker when the jet boundary layer is initially turbulent. This is not an indication of the lack of universality of the stable pairing mode concept but is probably due to the fact that a higher initial turbulence produces a jitter in the pairing location. The jet centreline velocity signal – which is a good indicator of large-scale activity in the shear layer – revealed that pairing became intermittent. Subharmonic data (figure 12*d*) indicate that the pairing occurs over a range of St_{D_e} from 0.7 to 0.8. For the turbulent case, the pairing is not as sharply defined in frequency nor is it as dominant (e.g. peak of $u_{\frac{1}{2}f}'$ is lower) as in the laminar case (compare figures 11 and 12).

The spectral evolutions of u along the jet axis for unexcited jets, N1 and N4, are shown in figure 13(*a*, *b*) respectively. At small x, the spectral peak is much broader for the laminar jet (N1) than for the turbulent jet (N4). The corresponding St_{D_e} values at $x = 0.5D_e$ are nearly 0.8 and 0.5, respectively. With increasing x, the spectral peaks shift to lower frequencies, and St_{D_e} for both cases reach a terminal value of about 0.4 – the preferred mode frequency. The laminar jet (N1) first rolls up in the shear-layer mode. The vortices then pair before the jet-column instability takes over. Thus, sub- and higher-harmonics of the shear-layer instability mode with phase jitter produce a broader spectral hump. On the centreline, away from the vortices, the velocity signal captures only an integrated footprint which is smeared. For the turbulent jet (N4), the structures are rolled up at a larger x where only the jet-column instability manifests; that is, there is organized activity only at the terminal St_{D_e}, resulting in a spectral hump narrower than in jet N1. Note that because the roll-up of the initially turbulent jet occurs at the terminal St_{D_e}, the spectrum does not shift to lower frequencies with increasing x (figure 13*b*). The evolution of the centreline u spectrum in natural jets can show the presence of the preferred mode and can give

a rough estimate of its frequency. However, to obtain the precise value of the preferred mode St_{D_e}, one should study jets by exciting at one frequency at a time and select the preferred mode to be the frequency that produces the largest r.m.s. amplitude of the *fundamental*.

Effects of moderate excitation levels

We have stated that excitation as well as the initial condition can affect the switching location. Of course, excitation has to be properly selected by choosing the Strouhal number (i.e. mode) and the excitation amplitude. Based on the results discussed earlier, the two St_{D_e} values of obvious interest are 0.4 and 0.85, and we have studied the effects of excitation at these two St_{D_e} for both initially laminar and initially turbulent boundary layers. Here we focus on the effects of these excitations on jet spreading only. In the following, we discuss the results of moderate excitation level (viz. $u'_e/U_e = 2.5\%$). (The effects of a higher-level excitation (viz. $u'_e/U_e = 15\%$) are discussed immediately following.)

The effects of 2.5% excitation at $St_{D_e} = 0.4$ and 0.85 on the spreading of the initially laminar jet (N1) are shown in figure 14(*a*, *c*) and of the initially turbulent jet (N4) in figure 14(*b*, *d*); data in both major and minor planes are included. These are compared with the corresponding unexcited jet spread data (hollow symbols). To compare the effects of excitation on the jet cross-section, the corresponding variations of the equivalent jet width $B_e [\equiv (B_y B_z)^{\frac{1}{2}}]$ are shown in figure 14(*e*, *f*); figure 14(*g*) shows the percentage increase in the jet cross-sectional area $\Delta A\%$, computed by using B_e and expressed as the percentage increase with respect to the corresponding unexcited case.

From these figures, a number of observations can be made. The effect of excitation in shifting the switching location upstream is more pronounced in the initially turbulent jet than in the initially laminar jet. Both excitations (i.e. $St_{D_e} = 0.4$ and 0.85) move the switching location upstream: from $x/D_e \approx 3.5$ to 2 in the initially laminar jet (figure 14*a*, *c*) and from $x/D_e \approx 16$ to 4 in the initially turbulent jet (figure 14*b*, *d*). It is interesting that even though the dynamics of vortical structures under these two modes of excitation are quite different – namely, excitation at $St_{D_e} = 0.4$ inhibits pairing of structures, while excitation at $St_{D_e} = 0.85$ stabilizes pairing – the shift in the switchover location is insensitive to the St_{D_e} value; this is true at least for the excitation level and the two initial conditions studied. For the initially laminar jet, B_e distribution is almost the same at both the St_{D_e}, although noticeably higher than the unexcited case (figure 14*e*). In the initially turbulent jet, however, the effect of excitation in increasing B_e is less for $St_{D_e} = 0.85$ than for $St_{D_e} = 0.4$ (figure 14*f*).

There are no clear explanations for many of the differences seen in figure 14(*a–g*). Consider unexcited jets. The axial distance where the vortices roll up is much larger when the jet is initially turbulent than when initially laminar. Since the switching location follows the roll-up of vortical structures and their subsequent deformation due to self-induction, switching of axes in an initially turbulent jet should be expected to occur at a location farther downstream than that in an initially laminar jet. Excitation induces the formation of the vortical structures closer to the exit plane, shifting their deformation locations upstream and hence causing early switching of axes. (Roll-up of structures in an initially turbulent (unexcited) elliptic jet, their deformation and jet spreading are discussed in §7.3).

As mentioned earlier, preferred mode excitation produces almost equally strong

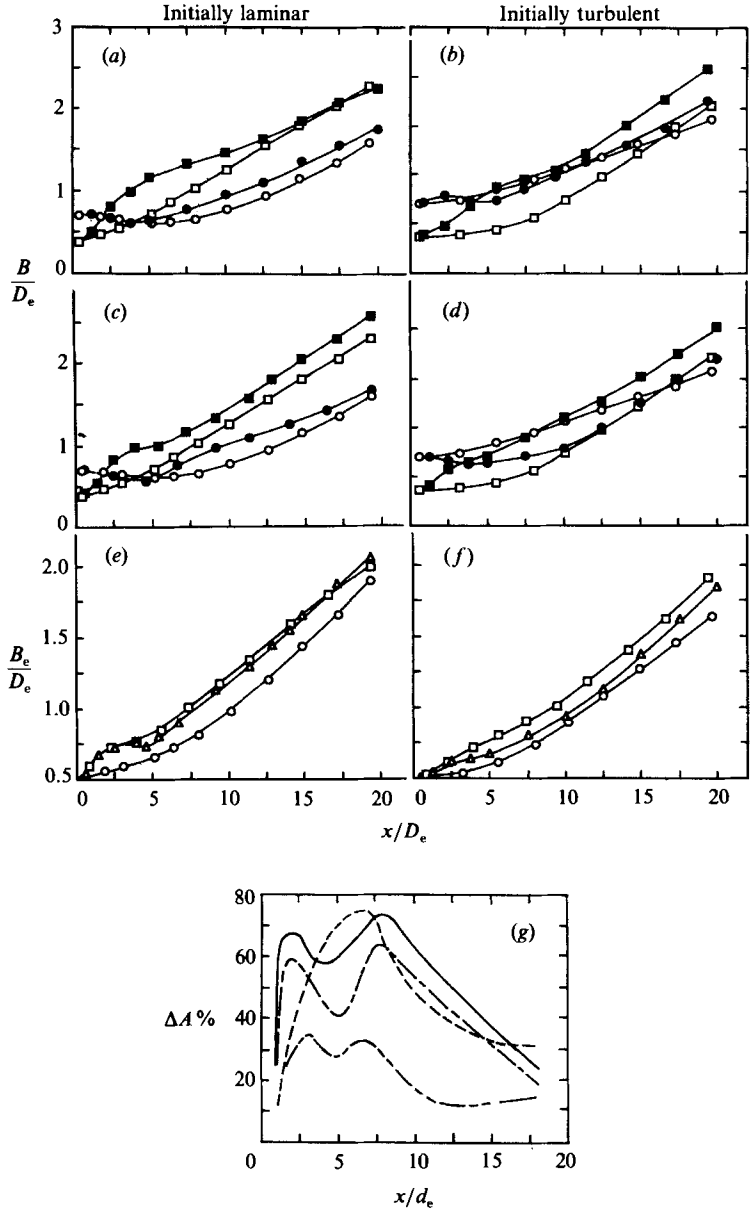

FIGURE 14. (*a*)–(*d*) Widths of unexcited and excited, initially laminar (N1) and turbulent (N4) jets: (*a*) N1, unexcited and excited ($St_{D_e} = 0.4$); (*b*) N4, unexcited and excited ($St_{D_e} = 0.4$); (*c*) N1, unexcited and excited ($St_{D_e} = 0.85$); (*d*) N4, unexcited and excited ($St_{D_e} = 0.85$). □, minor plane; ○, major plane; hollow symbols are for unexcited jets and solid symbols are for excited jets. Equivalent jet widths: (*e*) N1 jet; (*f*) N4 jet, ○, unexcited; □, $St_{D_e} = 0.4$; △, $St_{D_e} = 0.85$. (*g*) Percentage increase in jet cross-sectional area due to excitation. ——, N1 jet, $St_{D_e} = 0.4$; — — —, N1 jet, $St_{D_e} = 0.85$; – – –, N4 jet, $St_{D_e} = 0.4$; — — — —, N4 jet, $St_{D_e} = 0.85$. $D_e = 5.08$ cm, $U_e = 10$ ms^{-1}, excitation level $u'_e/U_e = 0.025$.

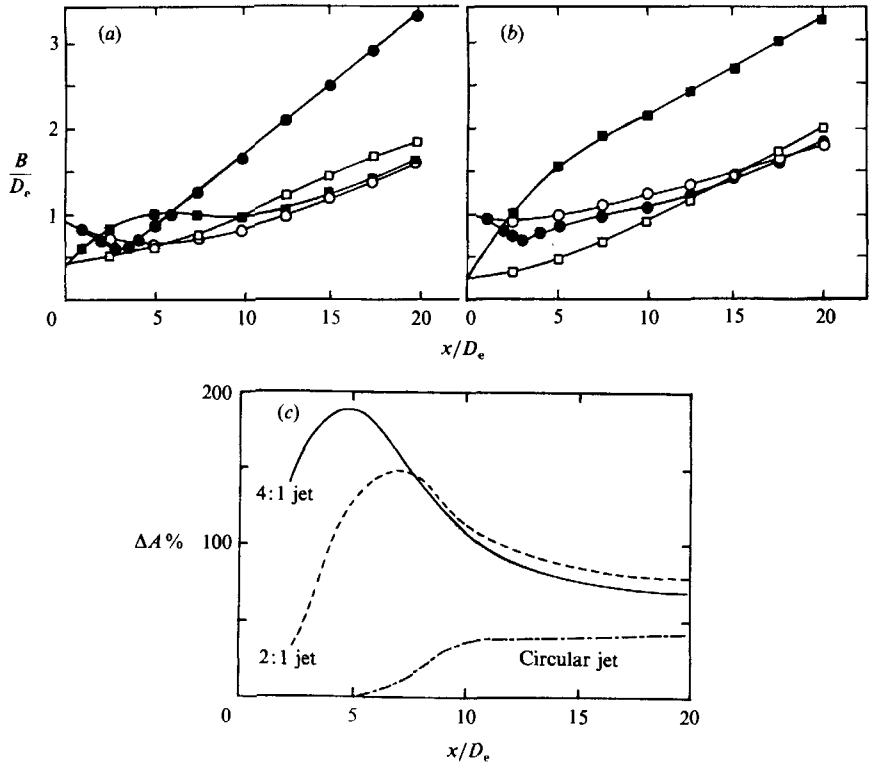

FIGURE 15. Widths of excited ($St_{D_e} = 0.4, u'_e/U_e = 0.15$) and unexcited jets: (*a*) 2:1 elliptic jet (N1); (*b*) 4:1 elliptic jet (N2). □, unexcited, minor plane; ○, unexcited major plane; ■, excited minor plane; ●, excited, major plane. (*c*) Percentage increase in the jet cross-sectional area under excitation ($St_{D_e} = 0.4, u'_e/U_e = 0.15$). ———, circular jet ($D = 5.08$ cm); – – – –, 2:1 jet (N1); ——, 4:1 jet (N2). $D_e = 5.08$ cm for elliptic jets, $U_e = 20.5$ ms^{-1} for all jets.

structures irrespective of the initial boundary-layer characteristics; this causes almost the same spreading of both initially laminar and turbulent jets. On the other hand, excitation, unless very strong, fails to stabilize the pairing process in the initially turbulent jet as effectively as it does in the initially laminar jet. Pairing occurs intermittently (as observed from the intermittent appearance of the subharmonic component of the u-signal) and also suffers from spatial jitter. Occasionally, structures do not interact, but break down instead. Thus, the effect of pairing on the spreading of a jet is much weaker when it is initially turbulent, in spite of the noticeable effect on the switchover location. Our detailed study of the dynamics of vortex pairing in an elliptic jet of aspect ratio 2 revealed that pairing occurs in the major plane, while in the minor plane, the trailing vortex, instead of merging with the leading one, rushes through it, pushing the minor-axis sides of the leading vortex transversely away from the jet axis (see Part 2). That is why the spreading in the minor plane of the initially laminar jet (figure 14*c*, solid square symbol) shows a hump at $x/D_e \sim 3$. Intermittent pairing with jitter in the pairing location does not produce such a hump in the initially turbulent jet. Note that if enhanced mixing is the objective, initially laminar elliptic jets are to be preferred. It is particularly interesting to note that the non-pairing excitation ($St_{D_e} = 0.4$) produces higher $\Delta A\%$

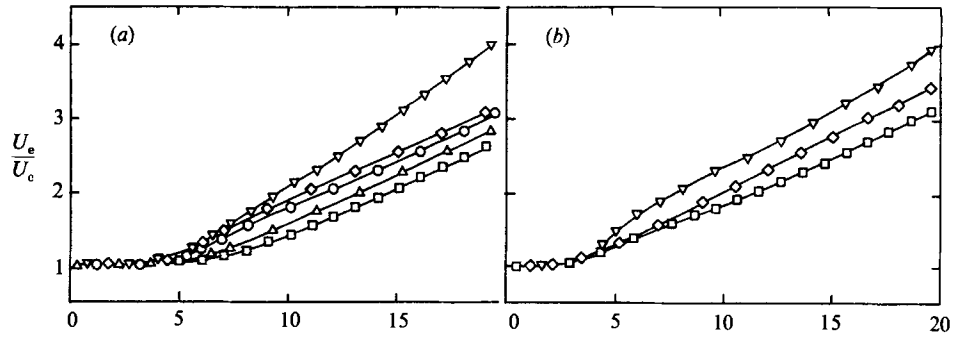

FIGURE 16. Dependence of the centreline mean velocity decay on excitation level at $St_{D_e} = 0.4$: (*a*) 2:1 elliptic jet (N1); (*b*) 4:1 elliptic jet (N2). Excitation levels u'_e/U_e are: □, unexcited; △, 1%; ○, 2%; ◇, 4%; ▽, 15%. $D_e = 5.08$ cm, $U_e = 20.5$ ms^{-1}.

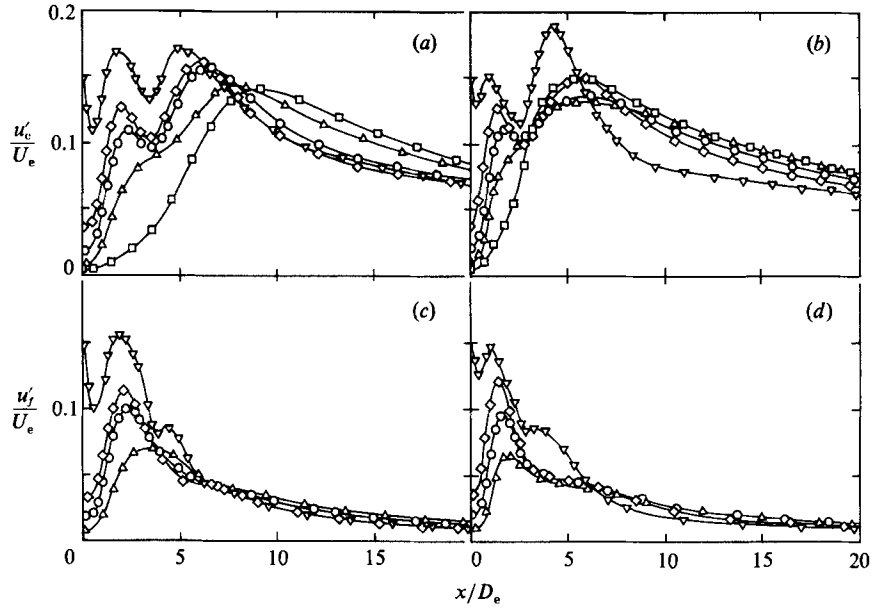

FIGURE 17. Dependence of $u'_c(x)$ on excitation level at $St_{D_e} = 0.4$: (*a*) 2:1 jet (N1); (*b*) 4:1 jet (N2). Dependence of $u'_f(x)$ on excitation level at $St_{D_e} = 0.4$: (*c*) 2:1 jet (N1); (*d*) 4:1 jet (N2). D_e, U_e and symbols are the same as in figure 16.

than pairing excitation ($St_{D_e} = 0.85$) – more so for the initially turbulent cases. Also interesting is the dip in ΔA% at $x/D_e \approx 4$ in the laminar cases.

Effects of strong excitation at $St_{D_e} = 0.4$

The effects are found to be quite dramatic at higher excitation levels. Hot-wire measurements were performed in jets N1 and N2 at various levels of excitation (viz. $u'_e/U_e = 0.01$, 0.02, 0.04 and 0.15) at the preferred mode frequency. The half-widths of the jets under preferred-mode excitation at the 0.15 level are shown in figure 15(*a*, *b*). Up to $x/D_e = 20$, major and minor axes switch twice in the 2:1 jet, but only once in the 4:1 jet. In either jet, excitation moves the switching location upstream and increases the ellipticity of the jet considerably. For example, at $x \approx 20D_e$, both jets

are nearly axisymmetric in the absence of excitation. However, when excited, the aspect ratio at this location increases dramatically.

The maximum increases in the jet cross-sectional area due to excitation are 150% and 190% for the 2:1 and 4:1 jets, respectively – considerably more than that in a circular jet (figure 15*c*). The corresponding centreline mean velocity distributions show increased velocity decay with increasing excitation amplitude (figure 16). The decay in a circular jet at similar excitation conditions (or for self-excitation using a whistler nozzle) is much less.

The centreline u_c'/U_e distributions (figure 17*a*, *b*) show that, for a low-level (1%) excitation, a broad hump is developed near the end of the potential core as a result of the breakdown of primary elliptic structures (similar to an unexcited jet). With increased excitation amplitude, a second peak develops upstream of the first; both peaks are amplified and they move upstream with increasing excitation level. Higher levels of excitation cause earlier formation of preferred-mode structures and earlier development of higher harmonics. Figure 17(*c*, *d*) shows that most of the energy near the first peak in u_c'/U_e distribution is due to the fundamental. Note that higher excitation levels cause a reduction of the total turbulence level downstream of the breakdown region even though the fundamental there remains unchanged. Presumably, higher excitations cause larger production and faster cascade, and thus a rapid far-field decay of the smaller scales.

Although we have not measured directly the mass entrainment, the increase in jet cross-section (based on the equivalent jet half-widths) in a region where the flow is well mixed owing to structure breakdown and where turbulence intensity is the highest, is an unambiguous indication of phenomenal increases in entrainment and turbulent mixing.

The jet response to excitation depends directly on the response of the coherent structures. In the 4:1 jet, the coherent structures respond to high-amplitude excitation by bifurcating into two rings. In the following, we demonstrate the occurrence of bifurcation through measurements of correlation, phase average and time average measures, and explain why bifurcation occurs in the 4:1 jet but not in the 2:1 jet.

6.2. *Bifurcation of an elliptic jet*

Obviously, time-average data alone cannot explain why the jets experience striking increases in the cross-section under strong excitation. To explore the dynamics of vortical structures, we studied the jets using flow visualization under strong excitation at the preferred mode. This revealed a rather dramatic picture of the events in the 4:1 jet. The major-axis sides of the vortical structures moved ahead of the minor-axis sides and toward the jet centreline much faster than they did in the 2:1 jet because of the greater curvature on the major-axis sides (see (3)). After the first switching of axes, the major-axis sides continued to move farther toward the jet centreline instead of reversing back to start another axis switchover. This caused the original major-axis sides to come close enough together at the jet centreline to touch each other. The resulting interaction seems to produce two nearly circular vortices via a cut-and-connect interaction. The 4:1 jet then spread more in the initial minor plane due to the presence and growth of two side-by-side, nearly circular structures. Cut-and-connect in isolated vortex rings has been known for some time (Takaki & Hussain 1985; Oshima, private communication), but this is the first time we observed bifurcation of a jet due to the cut-and-connect of advecting preferred mode structures. A sequence of this bifurcation process in an elliptic vortex ring is shown

schematically in figure 18(*a*). Figure 18(*b*) show flow-visualization pictures of the deformation and bifurcation of a preferred mode structure in the 4:1 elliptic jet; (i)–(iii) denote three successive phases of bifurcation recorded at successive x-locations. The resulting bifurcation of the elliptic jet is schematically shown in figure 18(*c*).

Annihilation, bridging and incomplete bifurcation

Very recent studies (Melander & Hussian 1988; Kida *et al.* 1989) have provided considerable insight into the cut-and-connect mechanism; these suggest that the bifurcation process is more subtle than indicated in figure 18(*a–c*). Figure 18(*d*) is an attempt to capture the reality; its contrast with actual flow pictures (figure 18*b*) needs explanation. The following paragraph explains this contrast, the essence of the cut-and-connect mechanism in an elliptic jet and the basis of figure 18(*d*).

A sequence of frames (1–6) in figure 18(*d*), each frame showing two orthogonal views, denote the dynamics of the elliptic vortex bifurcation process (synthesized from the direct numerical simulations); frame 6 (whose perspective view is frame 7) should correspond to the last frame in figure 18(*a*). As the two sides of the switched elliptic vortex touch each other (frame 3), the contiguous vortex lines from the two locally antiparallel vortex tubes (i.e. vortex dipole) undergo annihilation across the contact plane due to viscous cross-diffusion. The remaining parts of the annihilated vortex lines are instantaneously linked up, then advected, unfolded and stretched as they wrap around the two tubes. The accumulated bundle of cross-linked vortex lines form *bridges* (frame 4) across the initial tubes at either end of the contact zone (Melander & Hussain 1988). Annihilation is sustained as the two tubes continue to press against each other. The two bridges strengthen with the corresponding accumulation of cross-linked vortex lines, and become parts of two newly-formed vortex rings across the contact zone (frame 5); the configuration now is like that of eye-glasses with the dipole vortices as the nose-rest. Note that until frame 5 the two dipole vortices at the contact point were pressed against each other by curvature-induced self-induction (equation (1)). The flow induced by the bridges, however, reverses the curvature (between frames 5 and 6) of the dipole vortices which now move apart by self-induction (equation (1)). This would arrest annihilation, were it not for the fact that the stretching of the dipole intensifies vorticity gradient across the contact plane to sustain some annihilation. The two rings then move apart by self-induction, as do the remnants of the original unannihilated parts – the *threads* – connecting the two rings. The configuration in frames 6 and 7, consisting of two rings connected by two threads, then undergoes uneventful viscous decay. Of course, in an elliptic jet there will be further evolutionary changes including increased vorticity shedding, azimuthal instability and breakdown. Frames 6 and 7, showing large increases in vorticity boundary (of the two rings and threads) and associated vortex stretching, suggest that bifurcation is an efficient mechanism for mixing and enstrophy cascade; the process clearly must also be an active source of sound (Takaki & Hussain 1985).

Why are the threads not clear in picture (iii) of figure 18(*b*)? First, it is hard to visualize the bifurcation in detail in a jet because of turbulent diffusion of markers introduced upstream. Secondly, the experiment involves a very large Schmidt number (Sc), so the dye boundary is not a vorticity boundary. But even at $Sc = 1$, picture (iii) of figure 18(*b*) will look more like (*h*) of figure 18(*a*) rather than frame 7 of figure 18(*d*) because of intrinsic differences between scalar and vorticity transport in three-dimensional flows. Dye or smoke is a passive marker, while vorticity is not

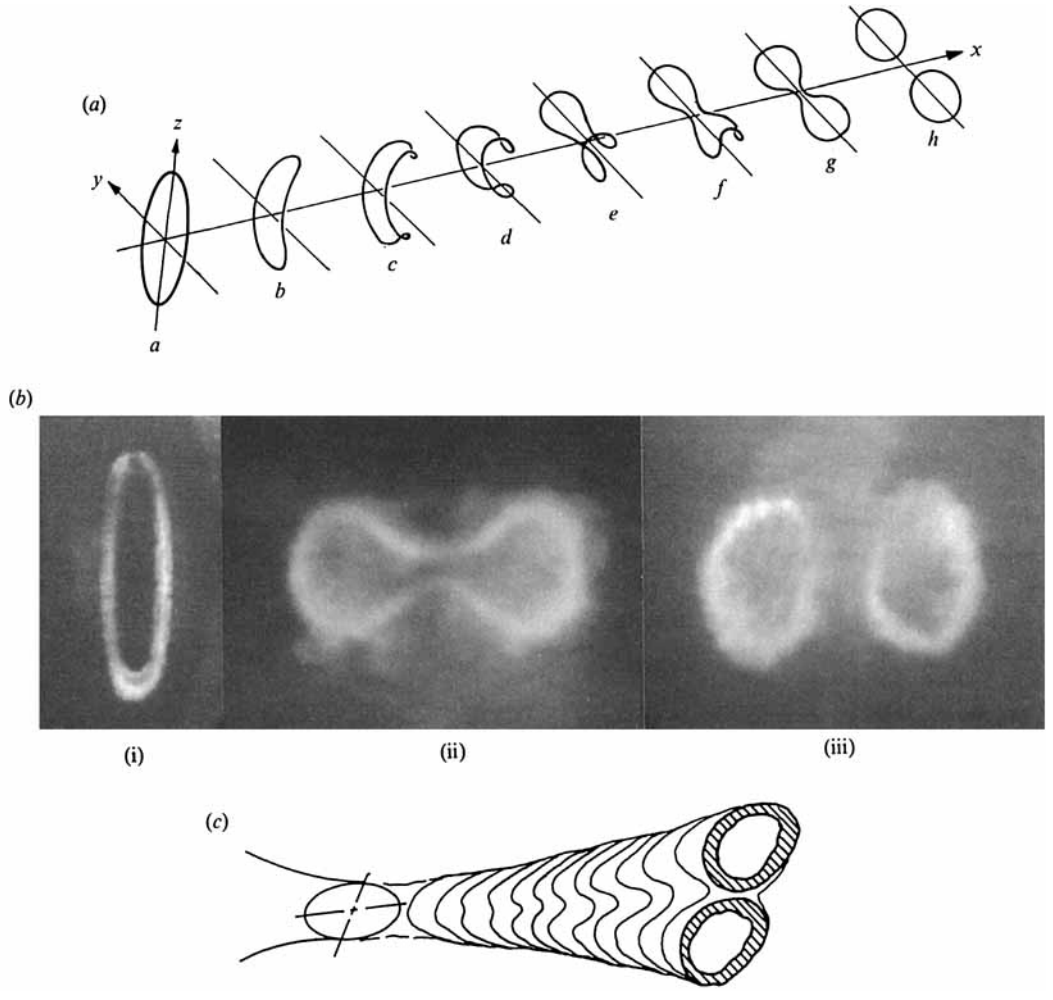

FIGURE 18(*a–c*). For caption see facing page.

and undergoes self-augmentation; markers are depleted away from zones of vorticity augmentation. Thus, flow visualization in a three-dimensional viscous flow can distract our attention away from the dynamically dominant events or points characterized by intensified vorticity. A direct simulation of reconnection of vortex tubes at $Sc = 1$ (Melander & Hussain 1988) shows that there is no scalar in the threads (the remnants of the dipole). This supports our longstanding warning (Hussain 1980, 1983) against relying too heavily on flow visualization to study coherent structures and vortex dynamics.

Further details of jet bifurcation

Unlike in the 4:1 jet discussed above, flow visualization failed to reveal any bifurcation in the 2:1 jet, consistent with the fact that the second switchover (figure 15*a*) could not happen if there were bifurcation after the first. The question remained open as to why the 2:1 jet also showed a high rate of jet spread and continued ellipticity, similar to that of the 4:1 jet (figure 15*a*, *b*). Is this due to a bifurcation farther downstream, where flow visualization failed to reveal any clear picture? In

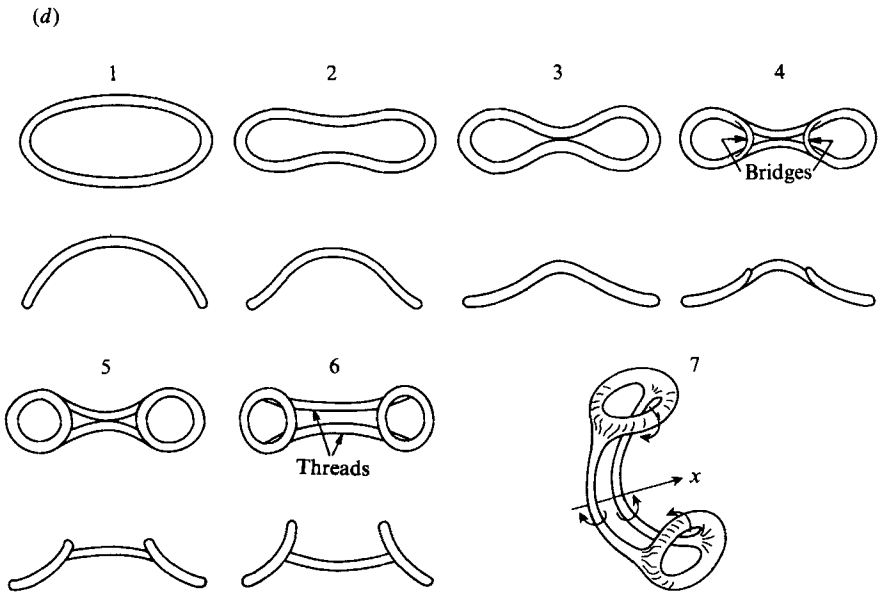

FIGURE 18. (*a*) Schematics of the cut-and-connect process in an elliptic vortex ring. (*b*) Flow visualization picture of the bifurcation of an elliptic vortical structure in the 4:1 jet. (i), (ii) and (iii) denote three successive phases of bifurcation recorded at successive x-locations. (*c*) Schematic of the bifurcation of an elliptic jet. (*d*) Schematics of the realistic cut-and-connect process in an elliptic vortex ring, showing the formation of bridges and threads. Frame 7 is a realistic perspective view of frame 6.

the 2:1 jet, if bifurcation does not occur, what mechanism produces the large spreading and increasing ellipticity of the jet? Additionally, what is the critical amplitude of excitation above which the 4:1 jet bifurcates? To address these questions thoroughly the obvious choice is to educe coherent structures at various phases during their evolution; this will be too cumbersome and is beyond the scope of this study. Instead, we address these questions using distributions of time average measures, such as cross-correlation coefficients, mean velocities, turbulence intensities and Reynolds stress, and using spectral evolution and limited phase-average measurements (of u only).

Distributions of cross-correlation coefficients R_{uu} are shown in figure 19(*a–f*) at a few streamwise locations; figures 19(*a*) and 19(*b*) are for the 2:1 jet and figures 19(*c*)–(*f*) are for the 4:1 jet, and measurements are limited to major and minor planes only. The coefficients are defined as

$$R_{uu}(\Delta y, \tau; x, y, z) = \frac{1}{u'_{\mathrm{r}} u'_{\mathrm{m}}} \frac{1}{T} \int_0^T u_{\mathrm{r}}(x, y, z, t)\, u_{\mathrm{m}}(x, y+\Delta y, z, t+\tau)\, \mathrm{d}t,$$

$$R_{uu}(\Delta z, \tau; x, y, z) = \frac{1}{u'_{\mathrm{r}} u'_{\mathrm{m}}} \frac{1}{T} \int_0^T u_{\mathrm{r}}(x, y, z, t)\, u_{\mathrm{m}}(x, y, z+\Delta z, t+\tau)\, \mathrm{d}t.$$

Here subscripts r and m denote reference and measurement probes, (x, y, z) is the location of the reference probe, and Δy and Δz are the probe separations in the y- and z-directions. An averaging period $T = 20$ s was used; this corresponds to the passage of about 3200 structures. For simplicity, when $\tau = 0$ we will denote the two correlations by $R_{uu}(\Delta y)$ and $R_{uu}(\Delta z)$ respectively. The location of the reference probe

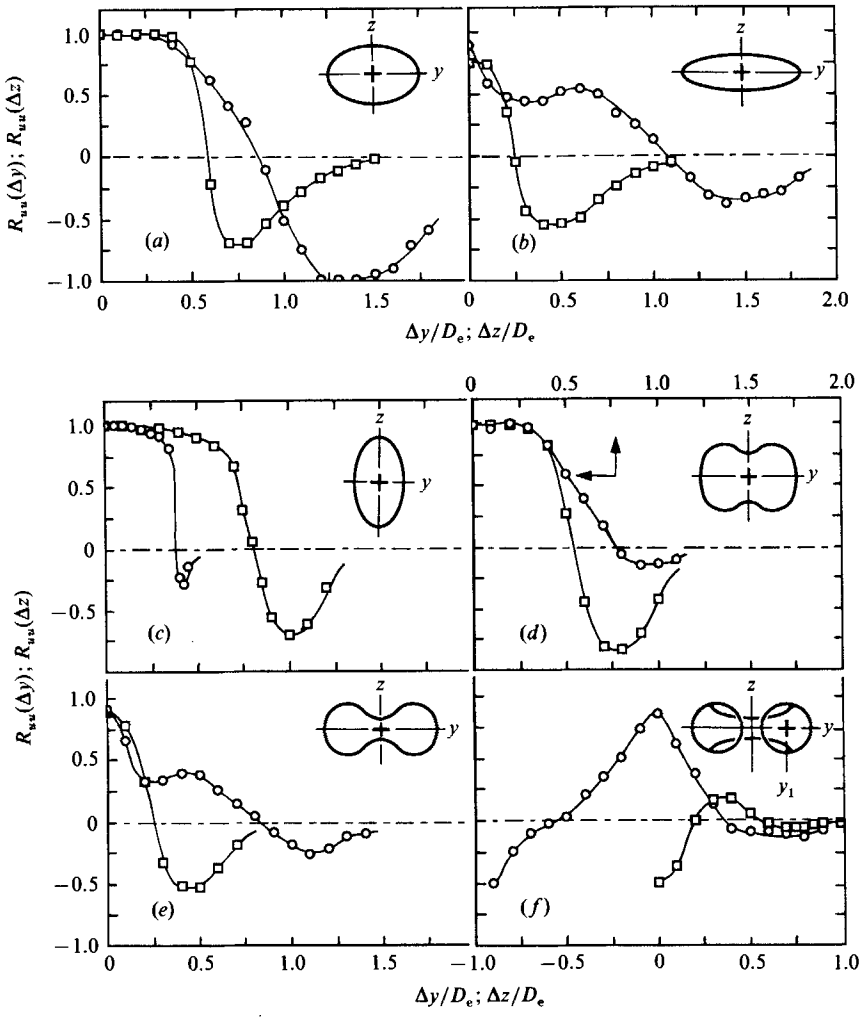

FIGURE 19(*a–f*). For caption see facing page.

(denoted by + symbol) along with schematics of the inferred structure configuration at the respective x-locations are shown as inserts in these figures; correlation data validate these configurations.

Note that the reference probe was placed on the jet axis except for measurements in the 4:1 jet at $x/D_e = 3.5$ (figure 19*f*). In this particular case, the u-signal was found to be highly random on the jet centreline, presumably due to the cut-and-connect process and the formation of bridging. That is why the reference probe was placed in the minor axis at $y = y_1 (= 0.9D_e)$, where the u-signal was found to be much cleaner; the measurement probe was, once again, traversed in the y- and z-axes only.

For all of the correlation measurements, the reference probe had to be placed about 3 mm above the measurement probe such that the measurement probe did not hit the reference probe during its travel. Because of this transverse separation between the probes and increased random u-fluctuations with increasing x, the

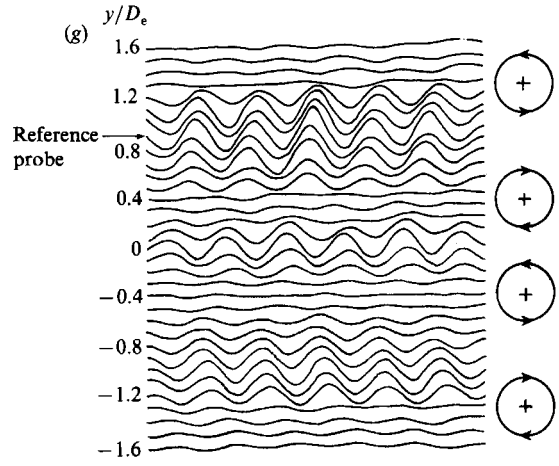

FIGURE 19. Distributions of cross-correlation coefficients $R_{uu}(\Delta y)$ and $R_{uu}(\Delta z)$ under strong excitation at the preferred mode frequency ($St_{D_e} = 0.4$, $u'_e/U_e = 0.15$): (*a*) N1 jet, $x/D_e = 2$; (*b*) N1 jet, $x/D_e = 4$; (*c*) N2 jet, $x/D_e = 1$; (*d*) N2 jet, $x/D_e = 2$; (*e*) N2 jet, $x/D_e = 3$; (*f*) N2 jet, $x/D_e = 3.5$. ○, minor plane; □, major plane. (*g*) Traces of $R_{uu}(\Delta y, t)$ in the minor plane of the N2 jet at $x/D_e = 3.5$. $D_e = 5.08$ cm, $U_e = 20.5$ ms^{-1}. + sign in the inserts in figures 19(*a*–*f*) denotes reference probe location.

maximum values of $R_{uu}(\Delta y)$ and $R_{uu}(\Delta z)$ remained below unity for $x/D_e > 2$; for $x/D_e < 2$ and within the potential core, the unity value was achieved.

It is to be expected that $R_{uu}(\Delta y)$ and $R_{uu}(\Delta z)$ should change sign across the core of advecting structures because of the change in the phase of u by 180°. Each of $R_{uu}(\Delta y)$ and $R_{uu}(\Delta z)$ distributions in the 2:1 jet show only one zero crossing (figure 19*a*, *b*), suggesting the advection of single vortical ring structures through the (y, z)-plane. Similar to the 2:1 jet, $R_{uu}(\Delta y)$ and $R_{uu}(\Delta z)$ in the 4:1 jet also show one zero crossing up to $x/D_e = 3$, indicating the advection of single ring structures at these x locations (figure 19*c*–*e*). At $x/D_e = 3.5$, however, $R_{uu}(\Delta y)$ shows two zero crossings (figure 19*f*). This suggests the splitting (i.e. bifurcation) of each original single structure into two ring structures as drawn in the insert in figure 19(*f*).

$R_{uu}(\Delta z)$ at $x/D_e = 3.5$ also show two zero crossings in the major plane. But, the positive peak of $R_{uu}(\Delta z)$ is much lower than that of $R_{uu}(\Delta y)$. This difference in $R_{uu}(\Delta z)$ can be explained if we consider the presence of the threads in the major plane. It appears that the circulation associated with the bridges is stronger than the threads at this x-location. As a result, the induced velocity of the bridges overshadows the induced velocity of the threads near the jet axis. Since these two induced velocities act in opposite directions (see frame 7 in figure 18*d* and also figure 24*c*) the resultant velocity field thus produces negative correlation in the vicinity of the jet axis. But with increasing Δz and closer to the thread, the induced velocity of the thread is strong enough to produce a small region of low positive $R_{uu}(\Delta z)$ at $\Delta z/D_e \approx 0.3$. Away from the thread, $R_{uu}(\Delta z)$ becomes negative again, as expected (similar to all the other curves). These correlations qualitatively suggest that the distances of the bridges and the threads from the jet axis are roughly $0.5D_e$ and $0.3D_e$ respectively at this x-location.

Note that, because of the off-centreline location of the reference probe, both positive and negative values of Δy are included in figure 19(*f*). Also, the absolute value of $R_{uu}(\Delta z)$ at $\Delta z = 0$ is considerably lower than 1 because the reference probe

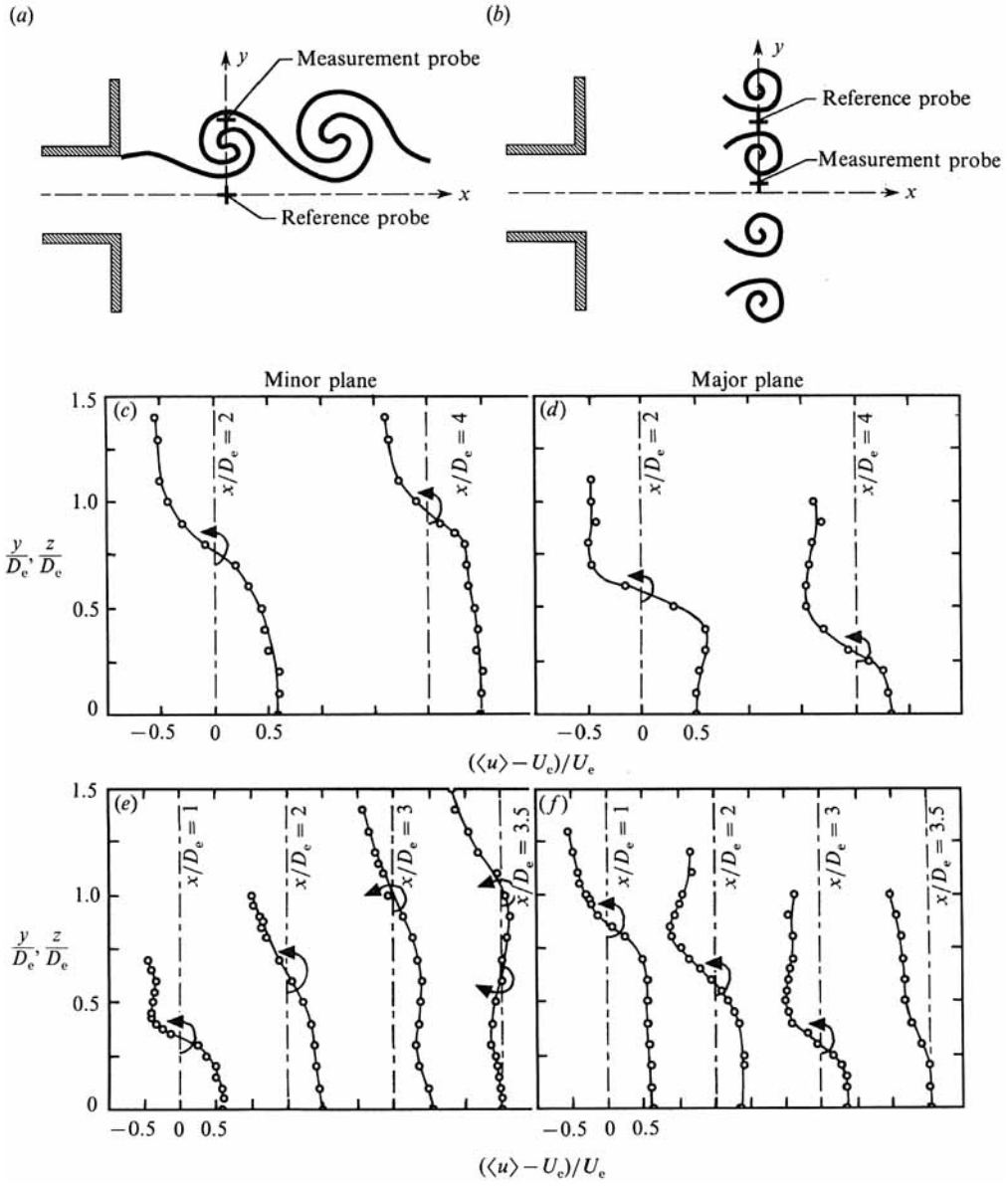

FIGURE 20. (*a*, *b*) Schematics, showing the probe arrangement for phase-average measurements. Profiles of $(\langle u\rangle - U_e)/U_e$: (*c*) N1 jet, minor plane; (*d*) N1 jet, major plane; (*e*) N2 jet, minor plane; (*f*) N2 jet, major plane. $D_e = 5.08$ cm, $U_e = 20.5$ ms^{-1}, $St_{D_e} = 0.4$, $u'_e/U_e = 0.15$.

was located off-axis (by the probe separation $y_1 = 0.9D_e$ in y), while the measurement probe was traversed along the z-axis. Particularly note also that the leftmost data in the two profiles in figure 19(*f*) correspond to the measurement probe being on the jet axis.

These time-average correlation data give only qualitative indications of advecting structures, as the correlation is also weighted by flows between structures. To get a better idea, it is useful to consider space–time correlations. In figure 19(*g*) we show these as time traces as a function of the displacement Δy with respect to the reference

probe (located at $y/D_e = 0.9$) for the 4:1 jet at $x/D_e = 3.5$. The traces show the phase reversal of perturbations in u across each vortex core region. Based upon the transverse locations of such phase reversals, approximate core locations along with their direction of rotation are indicated on the right-hand side of this figure. A strong correlation, even across the jet axis and retaining clear periodicity, signifies periodic occurrence of organized events, in particular, stable bifurcation of advecting structures.

The structure bifurcation is also evident from the distributions of phase-averaged, longitudinal velocity $\langle u \rangle$; this is clearer when $\langle u \rangle$ is examined in a reference frame moving with the structure convection velocity U_c. Since excitation induced the cut-and-connect events to be periodic (discussed above), $\langle u \rangle$ could be satisfactorily determined by phase-locked measurements. For this purpose, the reference probe was placed at the same locations as for cross-correlation measurements just discussed and its signal was used as the reference for selection of the phase for sampling the measurement probe signal.

Phase averaging was performed using a real-time analyser (Ono Sokki CF-920). The peaks in the $u_r(t)$ signal of the reference probe corresponded to the passage of structure cores past the reference probe; see figure 20 (a, b) for schematics of single and bifurcated structures. The data acquisition of the measurement probe was initiated by triggering on the reference probe signal when the latter reached a level close to its peak value; following each trigger, data were taken for a period of about six structure passages. At the next trigger, a new batch of structures were sampled and recorded. A total of 512 realizations were collected and then ensemble averaged.

The structure convection velocity U_c was inferred as the $\langle u \rangle$ at the transverse location where the phase of $\langle u \rangle$ changed by 180°. Transverse profiles of $(\langle u \rangle - U_c)/U_e$ are shown in figure 20 (c–f) with the inferred structure locations indicated by curved arrows. Because elliptic structures do not remain planar (as they deform by self-induction), the zero crossing of a $(\langle u \rangle - U_c)/U_e$ profile does not denote the exact structure centre when the structures are inclined to the (y, z)-plane; only spatial distributions of phase-averaged vorticity contours can identify the exact centre. However, a change in the sign of $(\langle u \rangle - U_c)$ with increasing y clearly indicates the presence of a vortical structure. A change in the direction of $(\langle u \rangle - U_c)$ twice in the minor plane of the 4:1 jet at $x/D_e = 3.5$ indicates the presence of two vortical core regions on one side of the jet, confirming the occurrence of bifurcation of an elliptic structure into two – one on each side of the jet axis.

Critical amplitude of excitation for stable bifurcation

To determine the critical amplitude of excitation required for jet bifurcation, $R_{uu}(\Delta y)$ was measured in the minor plane of the 4:1 jet at $x/D_e = 3.5$ for various initial excitation levels (viz. $u'_e/U_e = 3, 5, 7.5, 10, 12$ and 15%). For $u'_e/U_e > 5\%$, two zero crossings of the $R_{uu}(\Delta y)$ distribution confirm jet bifurcation (figure 21 a, b). With decreasing excitation levels, the absolute value of $R_{uu}(\Delta y)$ near the jet axis ($\Delta y = -0.9D_e$) also decreases and becomes approximately zero for $u'_e/U_e < 5\%$. This indicates that for $u'_e/U_e < 5\%$, no stable bifurcation occurs at this streamwise location.

Time average profiles

Cross-correlation and flow visualization proved unsuccessful to reveal any clear structure for $x/D_e > 4$. We then decided to document the time-average characteristics of elliptic jets. Time-average profiles of U, V, u', v' and $\overline{uv}$ are shown for the 4:1

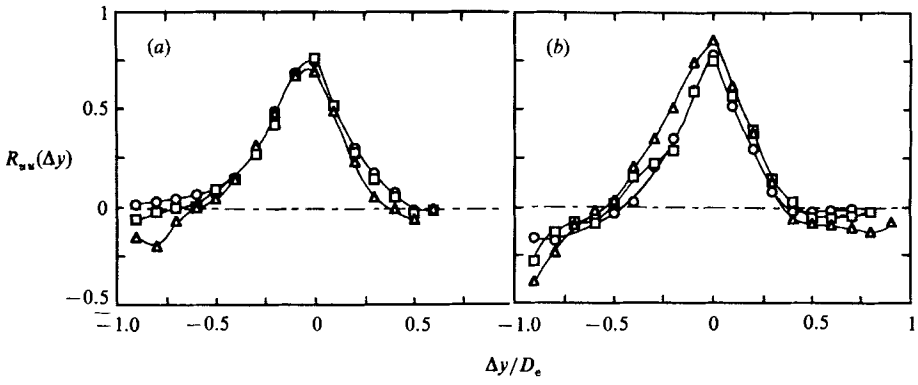

FIGURE 21. Distributions of $R_{uu}(\Delta y)$ in the minor plane of the N2 jet under various levels of excitation, showing the critical level of excitation required for jet bifurcation. $D_e = 5.08$ cm, $U_e = 20.5$ ms^{-1}, $St_{D_e} = 0.4$, $x/D_e = 3.5$. Excitation levels u'_e/U_e are: (*a*) ○, 0.03; □, 0.05; △, 0.075; (*b*) ○, 0.1; □, 0.12; △, 0.15.

and 2:1 jets in figures 22 and 23, under excitation at $St_{D_e} = 0.4$ and $u'_e/U_e = 15\%$. These data may also serve as benchmarks for validating three-dimensional numerical codes.

For the 4:1 jet, profiles of time-average measures in the minor and major planes are significantly different. For $x/D_e > 3.5$, profiles of U, u', v' and $\overline{uv}$ have two peaks (say, humps) in the minor plane (including the peak on the axis), while there is only one peak in the major plane. The time-average profiles are in agreement with our hypothesis of the bifurcation of the 4:1 jet. In figure 24, we schematically denote the effects of strong vortical structures on velocity profiles. The two vortex cores (say, 1 and 2), produced by bifurcation are shown in figure 24(*a*) along with their induced velocity fields. When these induced velocities are superimposed on the basic $U(y)$ distribution (dashed line), the resulting velocity distribution (solid line) represents the phase-average velocity $\langle u \rangle$ at the instant when the structure crosses this plane. Note that each vortex produces a peak and a valley in the $\langle u(y) \rangle$ profile (figure 24*b*). The time-average profile is the average of such $\langle u \rangle$ profiles at various phases during the advection of structures. This averaging process smears out the peaks and valleys in the $\langle u \rangle$ profiles to some extent, but, depending upon the strength of the vortices, still leaves a 'footprint' on the time-average profile. That is why, after bifurcation, we observe a valley and a hump in the velocity profile away from the jet axis owing to the presence of vortex 1 (figure 24*b*). The presence of vortex 2 does not produce the hump and valley clearly, but instead steepens the velocity gradient with respect to the unexcited state.

In the above discussion, we have not considered the effects of threads. After the cut-and-connect is completed, the flow dynamics in the vicinity of the jet axis is complicated by the presence of the threads in the major plane. The flow induced by the bridges and the threads, and the expected mean velocity profiles are shown schematically in figure 24(*c*). At the jet axis, the induced velocity of the threads is in the mean flow direction, but opposite to that of bridges; hence it is the reason for the spike in the velocity profile on the jet axis. $U(y)$ profiles across the entire jet are shown for two x-locations in figure 24(*d*). Apart from showing symmetry, the measured profiles agree very well with that inferred on the basis of bifurcated structures (figure 24*c*).

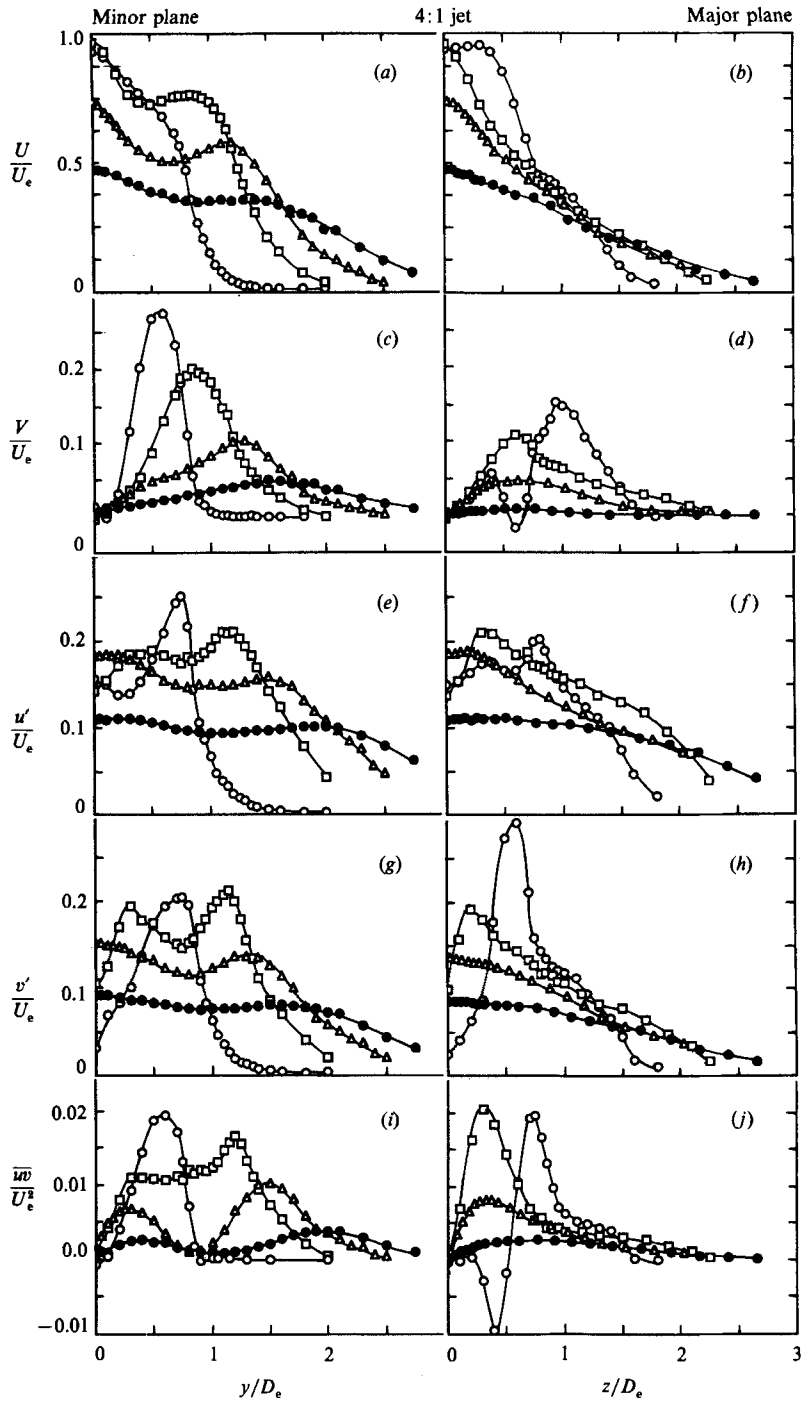

FIGURE 22. Time-average profiles of the 4:1 jet (N2) under excitation at $St_{D_e} = 0.4$, $u'_e/U_e = 0.15$: (*a*, *c*, *e*, *g*, *i*) for the minor plane and (*b*, *d*, *f*, *h*, *j*) for the major plane. (*a*, *b*) U; (*c*, *d*) V; (*e*, *f*) u'; (*g*, *h*) v'; (*i*, *j*) $\overline{uv}$. ○, $x/D_e = 2$; □, $x/D_e = 3.5$; △, $x/D_e = 5$; ●, $x/D_e = 7.5$, $D_e = 5.08$ cm, $U_e = 20.5$ ms^{-1}.

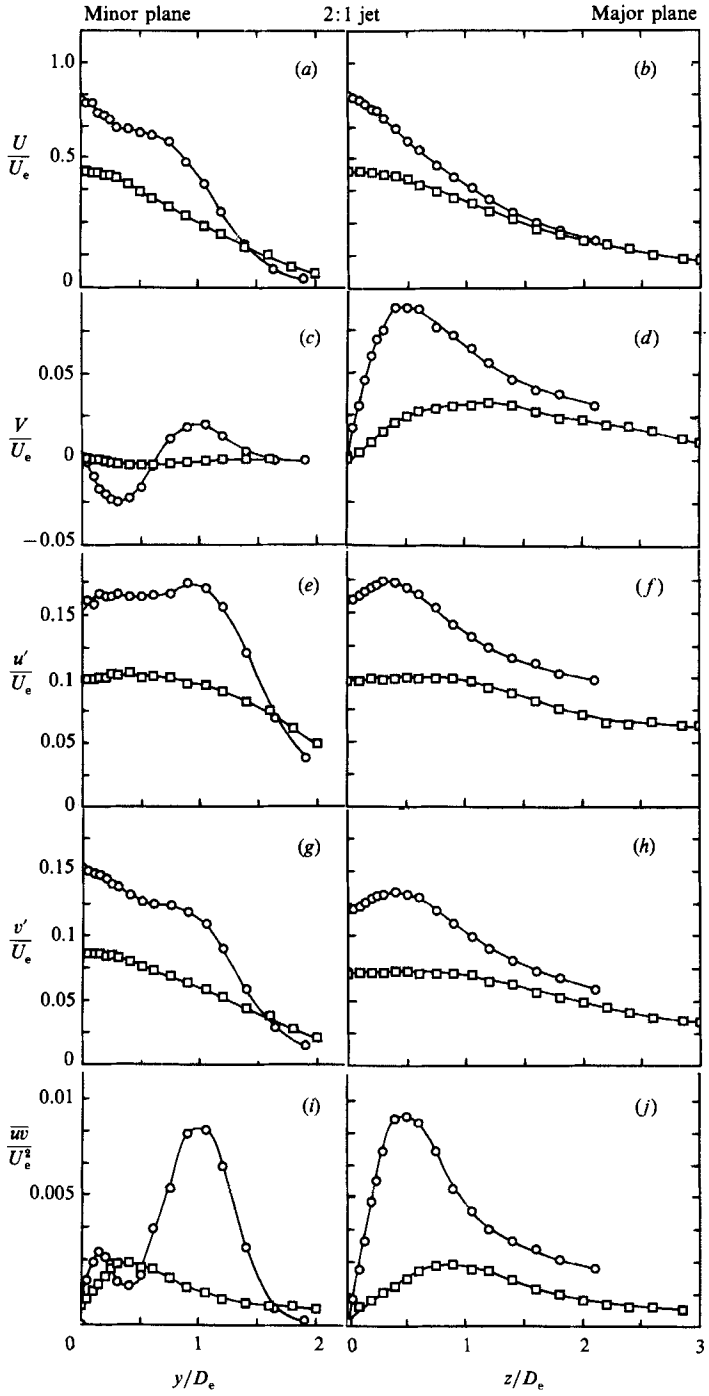

FIGURE 23. Time-average profiles of the 2:1 jet (N1) under excitation at $St_{D_e} = 0.4$, $u_e'/U_e = 0.15$: (*a*, *c*, *e*, *g*, *i*) for the minor plane and (*b*, *d*, *f*, *h*, *j*) for the major plane. (*a*, *b*) U; (*c*, *d*) V; (*e*, *f*) u'; (*g*, *h*) v'; (*i*, *j*) $\overline{uv}$. ○, $x/D_e = 6$; □, $x/D_e = 10$. $D_e = 5.08$ cm, $U_e = 20.5$ ms^{-1}.

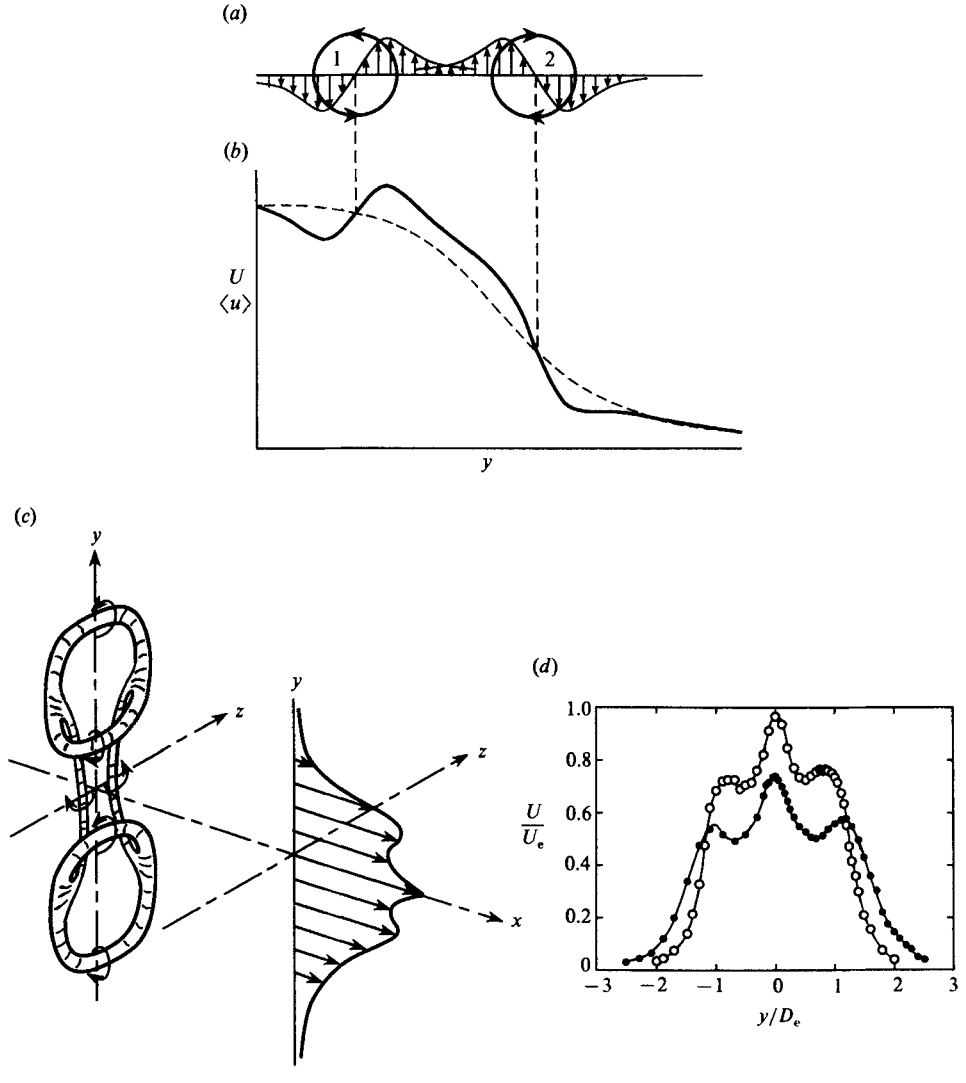

FIGURE 24. Schematics, showing the modification of the longitudinal velocity profile due to jet bifurcation. (*a*, *b*) Modification due to bridges only; (*c*) modification due to bridges and threads; (*d*) experimental $U(y)$ profiles at $x/D_e = 3.5$ (open symbol) and 5 (solid symbol) in the minor plane of the 4:1 jet. $D_e = 5.08$ cm, $U_e = 20.5$ ms^{-1}, $St_{D_e} = 0.4$, $u'/U_e = 0.15$.

Studies of coherent structures in various flows have revealed that each passage of a structure past a transverse location will result in a single peak in profiles of u', v' and $\overline{uv}$. For $x/D_e \geqslant 3.5$, the presence of two strong shear regions in the U profile, and two peaks in each of u', v' and $\overline{uv}$ profiles at $y/D_e \approx 0.3$ and 1.5 (figure 22(*a*, *e*, *g*, *i*)) suggest the advection of two vortex cores in the minor plane of the 4:1 jet. These data, again, demonstrate the bifurcation of an elliptic structure into two structures across the jet axis. Although time-average measures have identified jet bifurcation, one needs a more sophisticated conditional sampling technique – such as eduction of coherent structures – to study the details of structure evolution. This is beyond the scope of this study.

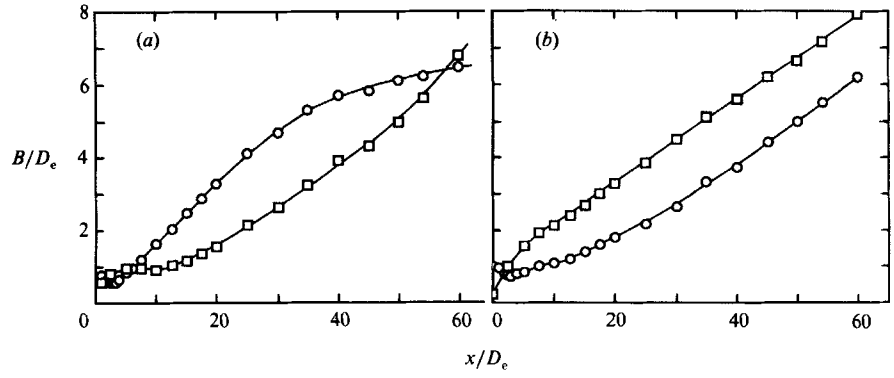

FIGURE 25. Effects of strong excitation at the preferred mode frequency ($St_{D_e} = 0.4$, $u'_e/U_e = 0.15$) on the far field jet widths: (*a*) 2:1 jet (N1); (*b*) 4:1 jet (N2). □, minor plane; ○, major plane. $D_e = 5.08$ cm, $U_e = 20.5$ ms^{-1}.

Since the entire structure in the minor plane of the 4:1 jet moves away from the jet axis, the V profiles, unlike other profiles, show a single peak. This is because the induced transverse velocity of opposite signs on the upstream and downstream sides of advecting structures has negligible contribution to the mean V. (In general, peak of $\langle v \rangle$ on the upstream side is slightly greater than that on the downstream side (Hussain 1983)). On the other hand, at $x/D_e = 2$, the inward motion of the vortex in the major plane produces a small region of negative V in the transverse direction. This region is also associated with negative Reynolds stress, indicating negative turbulence production. Note that the negative peak in $\overline{uv}$ occurs closer to the jet axis than in V. This is consistent with our detailed preferred mode coherent structure studies (Part 3) in a 2:1 jet, which show that the negative peaks in phase-averaged $\langle uv \rangle$ occur closer to the jet axis than in $\langle v \rangle$ as the structure in the major plane moves toward the jet axis.

The time-average profiles in the 2:1 jet (at two locations, e.g. $x/D_e = 6$ and 10) do not show two peaks in u', v' and $\overline{uv}$ profiles as observed in the 4:1 jet. The first x-location approximately corresponds to the second switching location. If bifurcation occurred in the 2:1 jet, it should have occurred downstream of the second switching location. However, the time average profiles at $x/D_e = 10$ do not indicate structure bifurcation in the 2:1 jet. Note that, at $x/D_e = 6$, the structures in the minor plane move slowly inward (see figure 15*a*), producing low negative values of V and a local decrease in $\overline{uv}$ at $x/D_e \approx 0.5$, but not strong enough to produce negative $\overline{uv}$ like in the 4:1 jet (figure 22*d*, *j*).

One expects that if bifurcation does not occur in the 2:1 jet, the advecting elliptic structures should switch axes further downstream. To examine this, we have extended the jet width measurements up to $x/D_e = 60$ (figure 25). Indeed, the width of the 2:1 jet shows a third switching of axes at $x/D_e \approx 58$, while the width of the 4:1 jet increases almost linearly in the minor plane. The switching of axes in the 2:1 jet at a far downstream location suggests no bifurcation even under strong excitation. This is consistent with the results of isolated elliptic vortices by Oshima (private communication), who observed bifurcation in elliptic vortices of aspect ratio greater than about 3.5, but not below this aspect ratio.

The question remained open as to why the 2:1 jet experiences a large increase in the jet width similar to the 4:1 jet, but without undergoing bifurcation. The

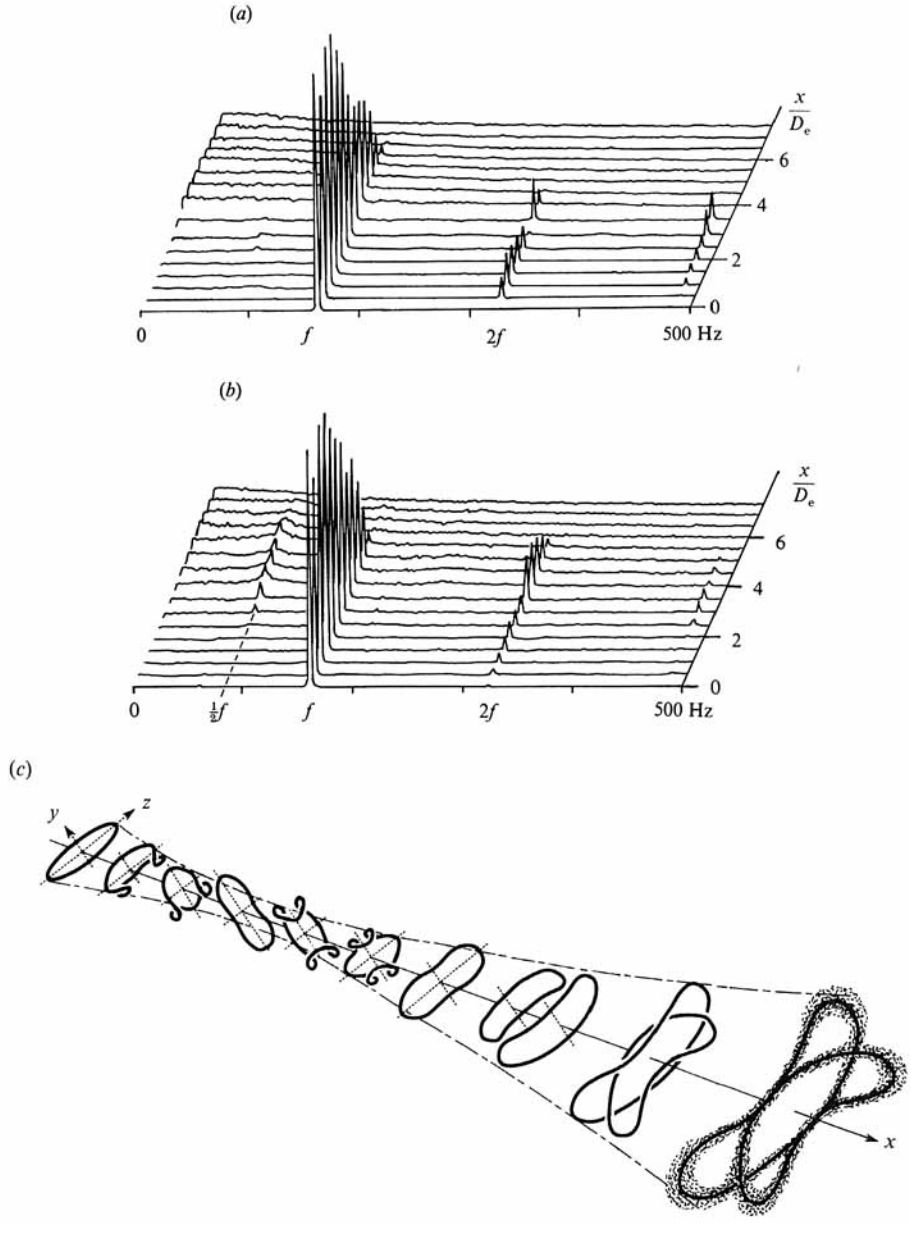

FIGURE 26. Evolution of centreline u-spectrum under strong excitation at $St_{D_e} = 0.4$, $u'_e/U_e = 0.15$: (*a*) 4:1 jet (N2); (*b*) 2:1 jet (N1). $D_e = 5.08$ cm, $U_e = 20.5$ ms^{-1}. x/D_e values are 0 to 7.5 at an interval of $0.5D_e$; (*c*) Schematic of pairing interaction in the 2:1 jet (N1).

mechanism for increased jet width in the 2:1 must be different from that of the 4:1 jet. The centreline spectral evolution of u-velocity shows the development of a weak subharmonic component in the 2:1 jet at $x/D_e \sim 4$, but no such subharmonic is present in the 4:1 jet (figure 26*a*, *b*). This indicates that near the second switching location of the 2:1 jet the structures start interacting, presumably *undergoing* intermittent pairing. This was further examined by flow visualization. Although flow visualization is obscured by the diffusion of dye markers at these distant locations,

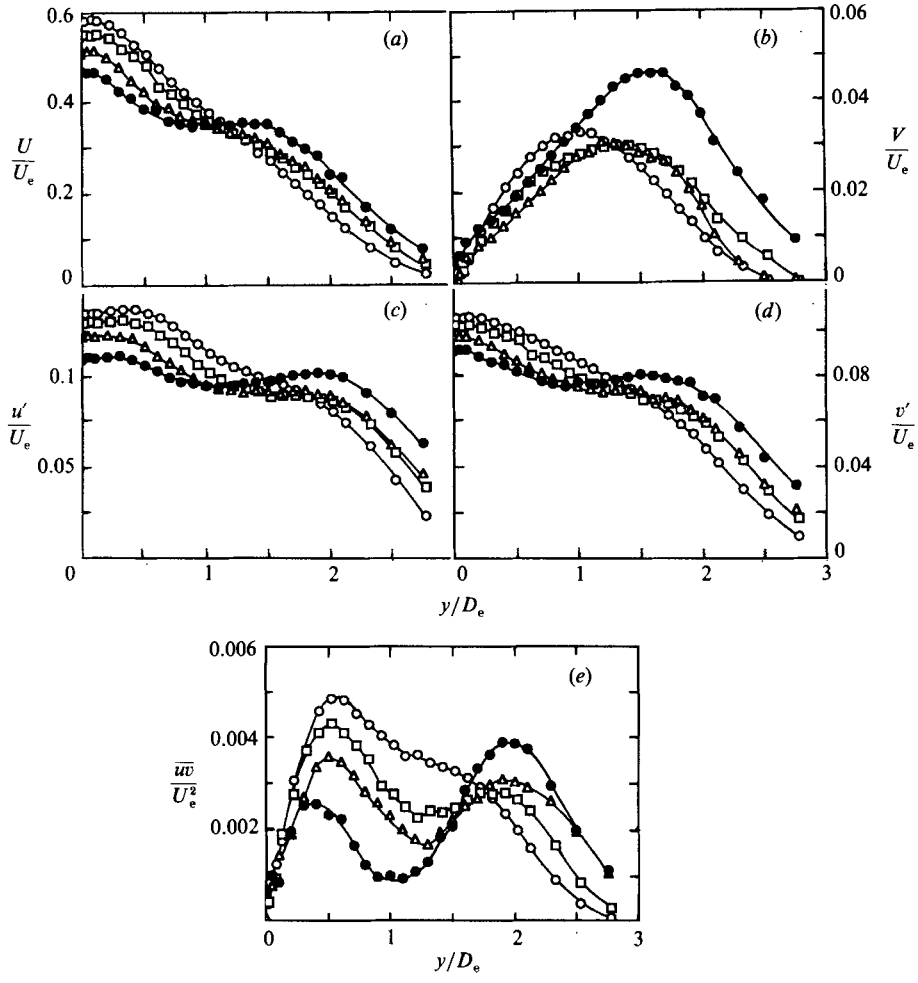

FIGURE 27. Effects of excitation level at $St_{D_e} = 0.4$ on time-average profiles in the minor plane of the 4:1 jet (N2) at $x/D_e = 7.5$, showing the critical level of excitation for jet bifurcation: (*a*) U; (*b*) V; (*c*) u'; (*d*) v' and (*e*) $\overline{uv}$. Values of u'_e/U_e are: ○, 0.05; □, 0.075; △, 0.1; ●, 0.15. $D_e =$ 5.08 cm, $U_e = 20.5$ ms^{-1}.

we were able to see evidence of intermittent merger of vortices in the minor plane; in the major plane, the trailing structure rushed through the leading one, dilating (viz. increasing the perimeter) the latter. That is why the jet experiences a large spread in the major plane. The interaction of vortical structures and their effect on the spreading of the jet are schematically shown in figure 26(*c*). It is quite plausible that during this interaction in the 2:1 jet, the structures break down and new elliptic structures are formed which undergo switching farther downstream. But this needs further investigation.

Effects of excitation level on time-average measures

Time-average quantities were measured for various levels of excitation in the minor plane of the 4:1 jet at $x/D_e = 7.5$ to examine the critical level of excitation which produces bifurcation of the jet. Profiles of U, V, u', v' and $\overline{uv}$ for various excitation levels (viz. $u'_e/U_e = 5$, 7.5, 10 and 15%) are shown in figure 27(*a–e*). For

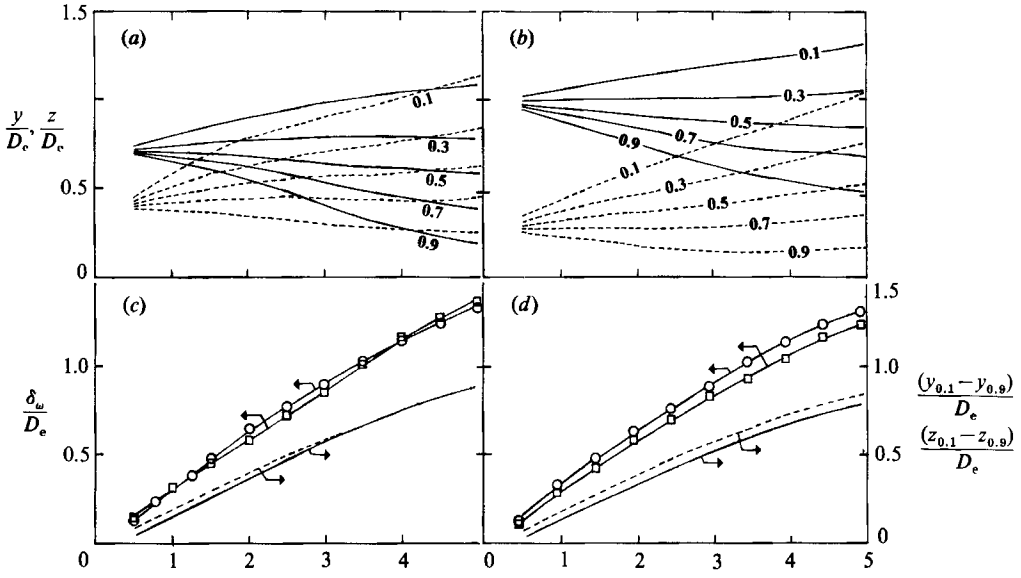

FIGURE 28. Contours of U/U_c in the near field of (*a*) 2:1 (N1) and (*b*) 4:1 (N2) jets. ----, minor plane; ——, major plane. (*c*, *d*) Streamwise variations of shear-layer and vorticity thicknesses for data in (*a*) and (*b*). ----, $(y_{0.1}-y_{0.9})/D_e$; ——, $(z_{0.1}-z_{0.9})/D_e$; ○, δ_ω/D_e in the minor plane; □, δ_ω/D_e in the major plane. $D_e = 5.08$ cm, $U_c = 29.26$ ms^{-1}.

$u'/U_e > 5\%$, a second peak in the U, u', v' and $\overline{uv}$ profiles is quite clear, consistent with the occurrence of jet bifurcation. From the cross-correlation coefficients (figure 21) and these time-average (especially $\overline{uv}$) profiles, it appears that for $u'/U_e < 5\%$, stable bifurcation of elliptic structures ceases to occur.

7. Time-average measures of unexcited jets

7.1. *Initially laminar jet: near field*

Shear layer thickness

Like axisymmetric shear layers, elliptic shear layer have an imposed lengthscale, namely, the jet equivalent diameter D_e. However, sufficiently close to the exit plane, if $\theta/D_e \ll 1$, as is typical in a jet with top-hat exit profile, the elliptic shear layer should behave like a plane shear layer. But with increasing x, this similarity should disappear. Thus, to characterize the entire elliptic shear layer, we need an appropriate local lengthscale. In the present study, the local vorticity thickness $\delta_\omega = U_c/(\partial U/\partial y)_{max}$ is used as the lengthscale to non-dimensionalize transverse coordinates; δ_ω is determined by first least-squares fitting a tanh (y) profile through the $U(y)$ data at each station and then obtaining the slope of this profile at $U/U_c = 0.5$.

U/U_c contours in figures 28 (*a*, *b*) show the spreading of elliptic shear layers (for N1 and N2) in both major and minor planes; note that the $U/U_c = 0.5$ line represents the half width. This line shows that the shear layer spreads outward from the jet axis in the minor plane, but more toward the jet axis in the major plane. Note that the inner boundary of the shear layer (say, $U = 0.9U_c$ line) of both jets approach the x-axis at a higher rate in the major plane than in the minor plane. The outer boundary (say, $U = 0.1U_c$ line), however, shows an opposite trend: the shear layer spreads initially

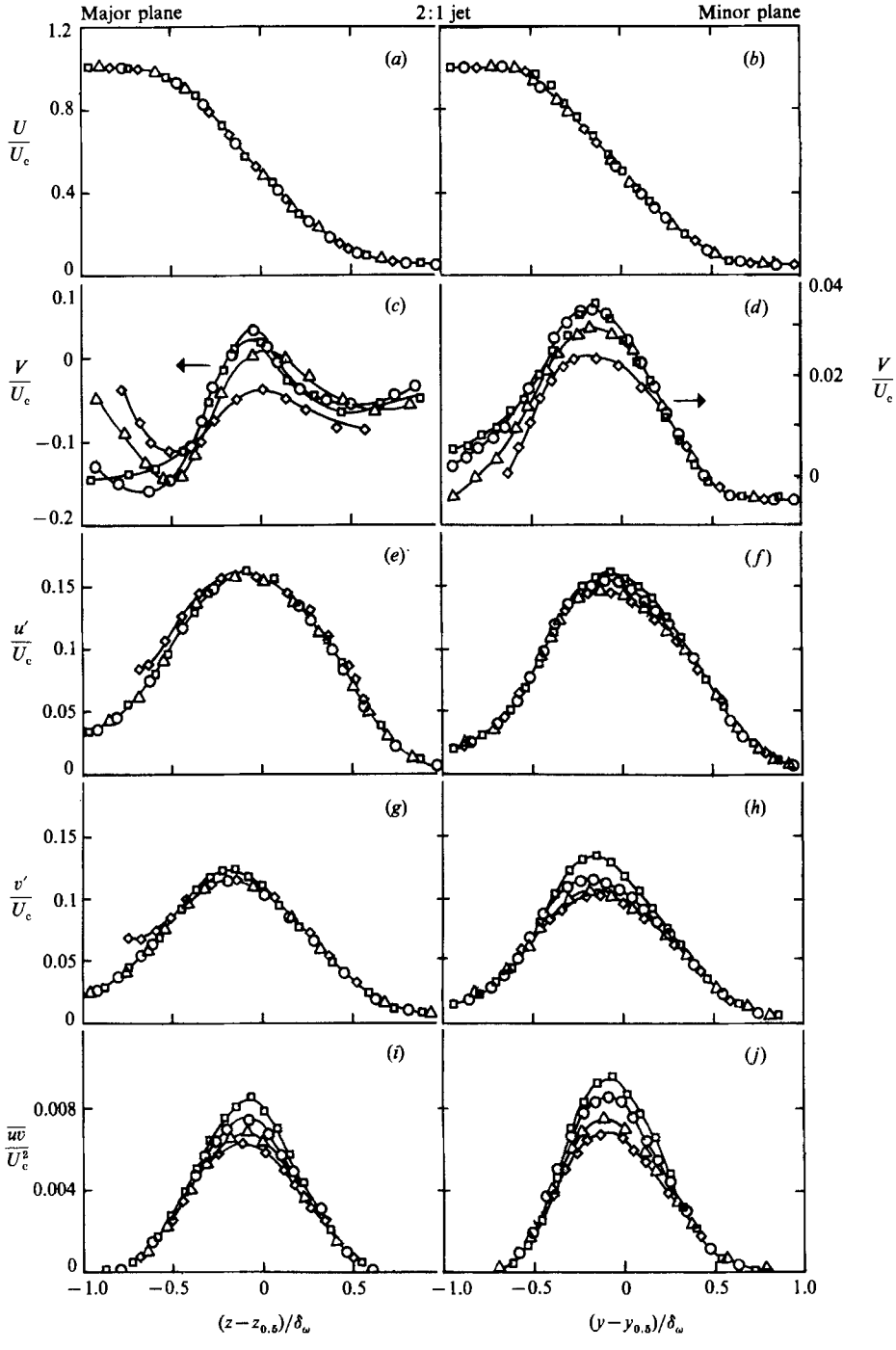

FIGURE 29. Time-average profiles in the near field of the 2:1 jet (N1): (a, c, e, g, i) for the major plane and (b, d, f, h, j) for the minor plane. (a, b) U; (c, d) V; (e, f) u'; (g, h) v'; (i, j) $\overline{uv}$. □, $x/D_e = 1$; ○, $x/D_e = 2$; △, $x/D_e = 3$; ◇, $x/D_e = 5$. $D_e = 5.08$ cm, $U_e = 29.26$ ms^{-1}.

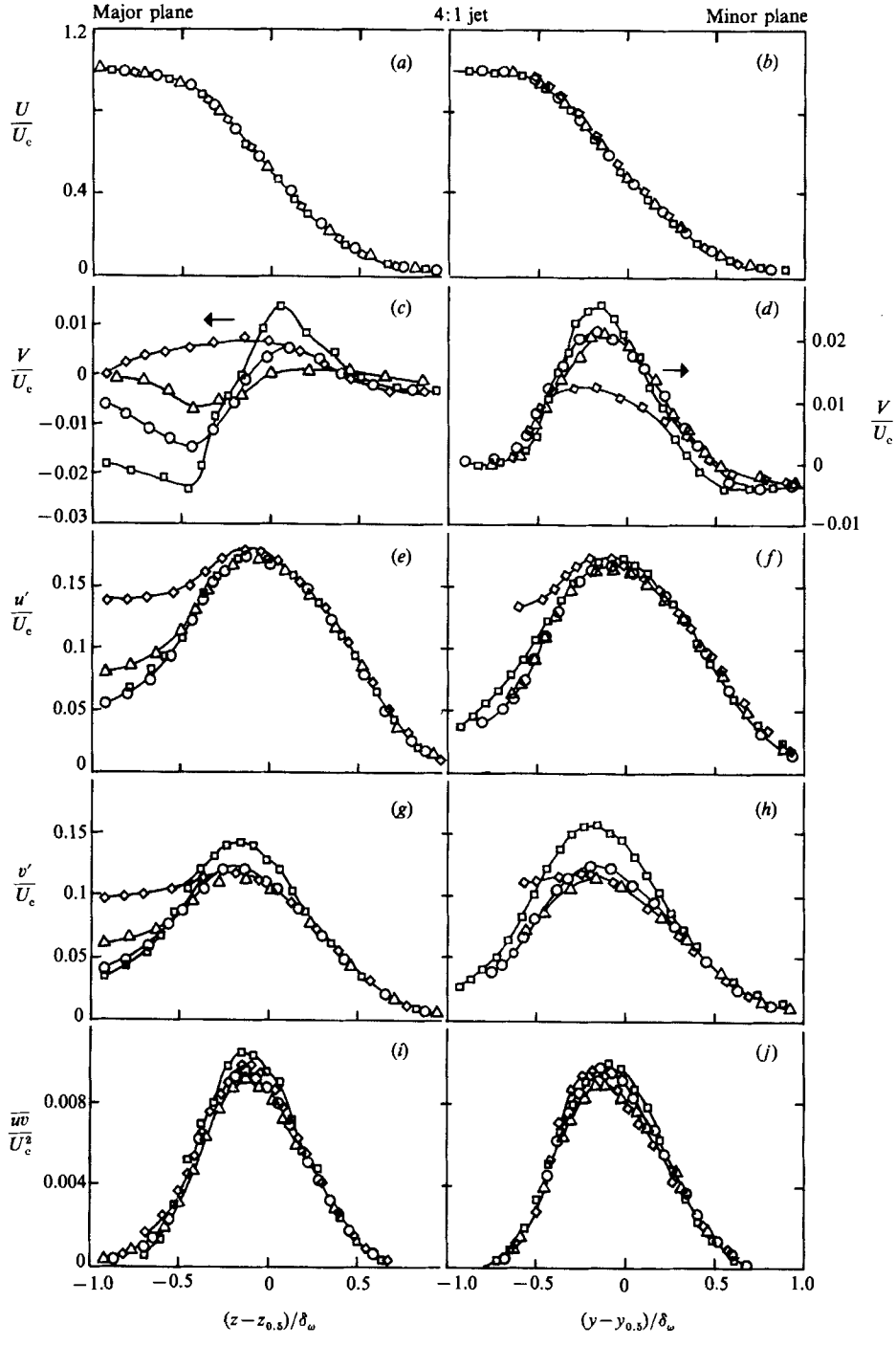

FIGURE 30. Time-average profiles in the near field of the 4:1 jet (N2). $D_e = 5.08$ cm; $U_e = 29.26$ ms^{-1}. The numbers and symbols are the same as in figure 29.

at a higher rate in the minor plane than in the major plane. That is, in the major plane, the shear layer spreads more on the high-speed side, while in the minor plane, the spread is more on the low-speed side. Yet, the shear-layer thicknesses ($y_{0.1}-y_{0.9}$, $z_{0.1}-z_{0.9}$) as well as values of δ_ω (figure 28*c*, *d*) are essentially the same in both planes. Note that, unlike in plane shear layers and plane and circular jets, the thicknesses of elliptic shear layers do not increase linearly with x: they increase less than proportionately with x. This nonlinearity is higher in a jet of higher aspect ratio.

Flow-field measures

Profiles of U, V, u', v' and $\overline{uv}$, non-dimensionalized by the local centreline mean velocity U_c, are shown in figures 29 and 30 for the 2:1 (N1) and 4:1 (N2) jets respectively. These data are plotted as functions of transverse coordinates $(y-y_{0.5})/\delta_\omega$ in the minor plane and $(z-z_{0.5})/\delta_\omega$ in the major plane; here $y_{0.5}$ and $z_{0.5}$ are the half-velocity locations. In these coordinates, U profiles show excellent similarity across the entire shear layer, while similarities in V, u', v' and $\overline{uv}$ are less so, V being the least. These profiles, however, exhibit better similarity on the low-speed side of the shear layer.

The spatial extent of the similarity of various turbulence measures depends on x. With increasing x, as the local θ becomes of the order of D_e, the similarity behaviour deviates from that of a plane shear layer because of the importance of spanwise curvature. Note that all profiles show comparable similarity on the low-speed side, but not necessarily so on the high-speed side. The reason is probably that there is complicated coupling of the organized structures across the jet centreline. The dissimilarity in the profiles appears sooner in x in the 4:1 jet because of its shorter potential core length. Unlike u' and v' profiles, $\overline{uv}$ profiles on the core side do not show noticeable dissimilarity because the velocity fluctuations on the core side are mostly potential and do not contribute to the Reynolds stress. Note that, since the local vorticity thickness exceeds the corresponding jet half width (i.e. $y_{0.5}$ or $z_{0.5}$) beyond a certain x, the profiles at these x locations stop short of $(y-y_{0.5})/\delta_\omega = -1$ or $(z-z_{0.5})/\delta_\omega = -1$ in figures 29 and 30 (for example $x/D_e = 5$, minor plane).

By symmetry, the transverse velocity should be zero on the jet axis. Note that, at $(y-y_{0.5})/\delta_\omega = -1$ and $(z-z_{0.5})/\delta_\omega = -1$ in figures 29 and 30, V is non-zero for small values of x (viz. $x/D_e = 1$ and 2) because these locations are far from the jet axis. Consider the minor plane first. $V(y)$ profiles attain positive values, reaching their maxima near the middle of the shear layer. Although the vortical structures in the minor plane move away from the jet axis, the outer edge of the V profiles shows a slight negative value. Why this is so can be understood by considering both the motion of a coherent structure and its induced velocity field. Detailed coherent structure measures (see Part 2) show negative v at the back and positive v at the front of coherent structures; the negative v region has a much larger radial extent, thus producing a negative region of mean V at the outer edge. Similar negative values are observed in rectangular jets also (see Krothapalli *et al.* 1981).

In the major plane, however, $V(z)$ profiles attain a negative peak on the high-speed side, approach zero value close to the half-velocity location, and decrease slightly with increasing transverse distance. This trend of $V(z)$ profiles is due to the inward motion of vortical structures. Closer to the jet exit (viz. $x/D_e = 1, 2$), the peak of $V(z)$ is more negative in the 4:1 jet than in the 2:1 jet because of higher radial velocity induced by higher curvature. In this plane, the positive v at the front of vortical structures is stronger than the negative v at the back. Thus, the strong outward motion at the front (i.e. positive v) would tend to nullify inward motion (i.e. negative

v) of the whole structure in the major plane. It is thus not surprising that the time-average V is close to zero near the middle of the shear layer.

For both jets, the transverse locations where u', v' and $\overline{uv}$ reach their respective peak values do not coincide with the half velocity location; peak values occur away from the half velocity point, approximately by $0.15\delta_\omega$ toward the jet centreline. (A similar trend was also observed in axisymmetric shear layers (Z. Hussain 1982).) These time-average profiles show some strong similarities between the two jets as is to be expected. Yet there are some unexplained differences: v' shows better collapse in the 2:1 jet than in the 4:1 jet, while $\overline{uv}$ profiles suggest better collapse in the 4:1 jet, etc. These differences, as well as the lack of similarity of V, u', v' and $\overline{uv}$ profiles even when U profiles show excellent similarity, warn against using U data alone as evidence of similarity.

7.2. *Initially laminar jet: far field*

Let us now look at the mean characteristics of the jet in the far field. Distributions of U/U_c, u'/U_c, v'/U_c and $\overline{uv}/U_c^2$ in both major and minor planes of the 2:1 jet (N1) are shown in figure 31 for $10 \leqslant x/D_e \leqslant 50$. These measures show that U/U_c profiles have achieved similarity already at $x/D_e = 10$, while u'/U_c, v'/U_c and $\overline{uv}/U_c^2$ do not show similarity even at $x/D_e = 50$. It is evident that the mean velocity is least sensitive to the initial condition, while higher moments take longer distances to reach their states of self-preservation. True self-preservation is perhaps achieved farther downstream of the location where systematic switching of axes ceases and the jet becomes virtually axisymmetric. Note that, for a given aspect ratio, vortical structures should undergo more severe deformation in a smaller elliptic jet than in a larger one because of greater curvature on the major-axis side in the former. This may be partly the reason why the mean velocity field in the present study ($D_e = 5.08$ cm) shows self-preservation (for $x/D_e > 10$), but not in the study of Ho & Gutmark (1987) in a smaller jet ($D_e = 3.59$ cm) even up to the largest x ($x/D_e = 28.3$) of their data.

Profiles of longitudinal turbulence intensity u'/U_c show a mild saddle even at $x/D_e = 50$. A similar but stronger saddle is also observed in plane jets (Heskestad 1965; Gutmark & Wygnanski 1976) and rectangular jets (Krothapalli *et al.* 1981), but not in circular jets for $x/D > 30$ (Wygnanski & Fielder 1969). The peak value of u' is greater than the peak value of v' in an elliptic jet, similar to both plane and circular jets. Along the jet axis, the ratio v'/u' attains a value of approximately 0.78–0.8; we find nearly the same value in circular, plane and rectangular jets studied by us and others. Profiles of either u' or v' are very similar in both major and minor planes, but $\overline{uv}$ distributions show higher peak values in the major plane, especially at large x/D_e. Similar higher peak values in $\overline{uv}$ distributions in the major plane were also found in rectangular jets (Krothapalli *et al.* 1981). Note that the location of the peak value of $\overline{uv}/U_c^2$ being close to the location of maximum mean strain rate (i.e. $(\partial U/\partial y)_{max}$ in the minor plane and $(\partial U/\partial z)_{max}$ in the major plane), one should expect a peak in the u' profile away from the jet centre. That this latter peak is not a strong one suggests that other transport terms are also dominant.

7.3. *Initially turbulent jet*

Mean velocity

The effect of an initially turbulent boundary layer on jet evolution is investigated using a 2:1 elliptic jet (nozzle N4). Contours of U/U_c for this jet are shown in figure 32(*a*, *b*); also included for comparison are data for the initially laminary boundary

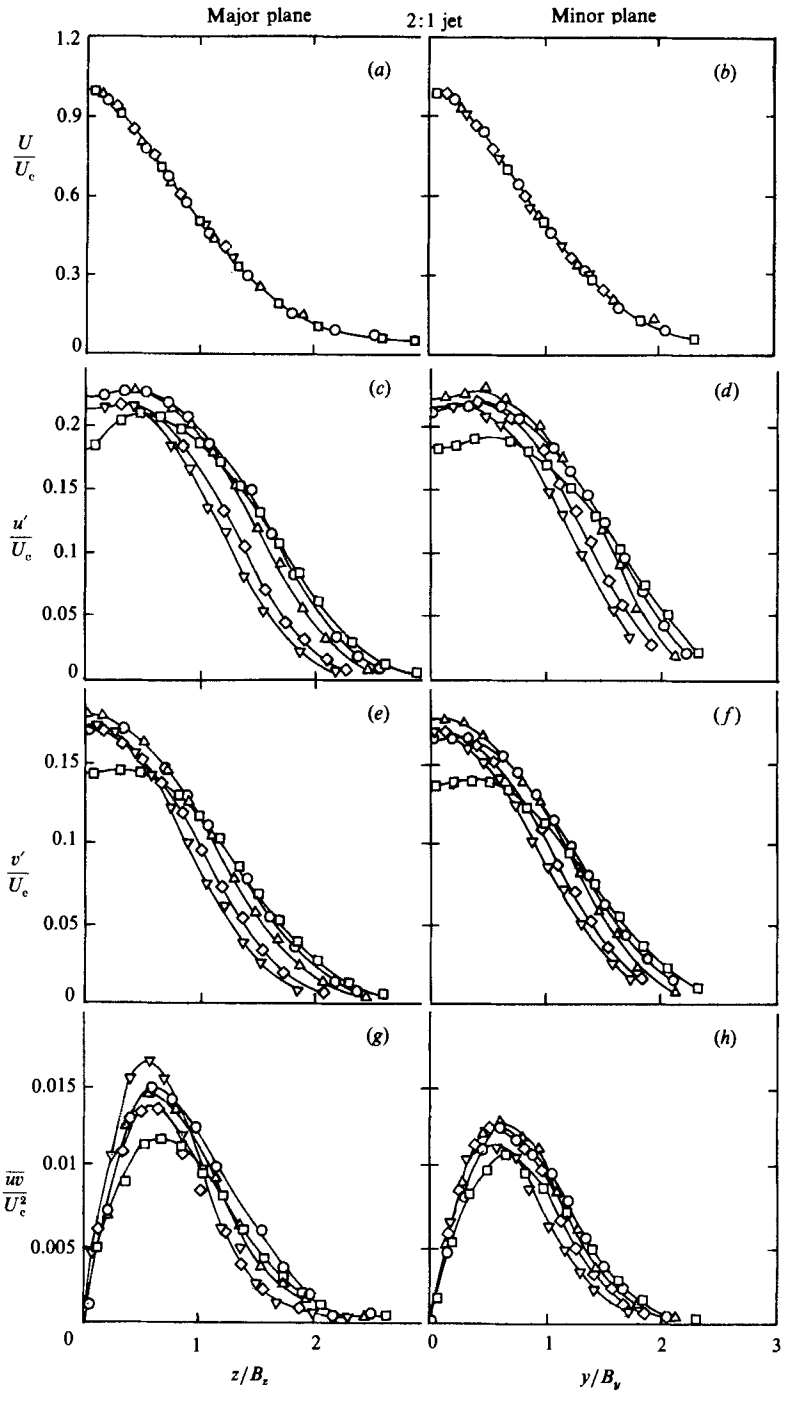

FIGURE 31. Time-average profiles in the far field of the 2:1 jet (N1): (*a*, *c*, *e*, *g*) for the major plane, and (*b*, *d*, *f*, *h*) for the minor plane. (*a*, *b*) U; (*c*, *d*) u'; (*e*, *f*) v'; (*g*, *h*) $\overline{uv}$. □, $x/D_e = 10$; ○, $x/D_e = 20$; △, $x/D_e = 30$; ◇, $x/D_e = 40$; ▽, $x/D_e = 50$. $D_e = 5.08$ cm, $U_e = 29.26$ ms^{-1}.

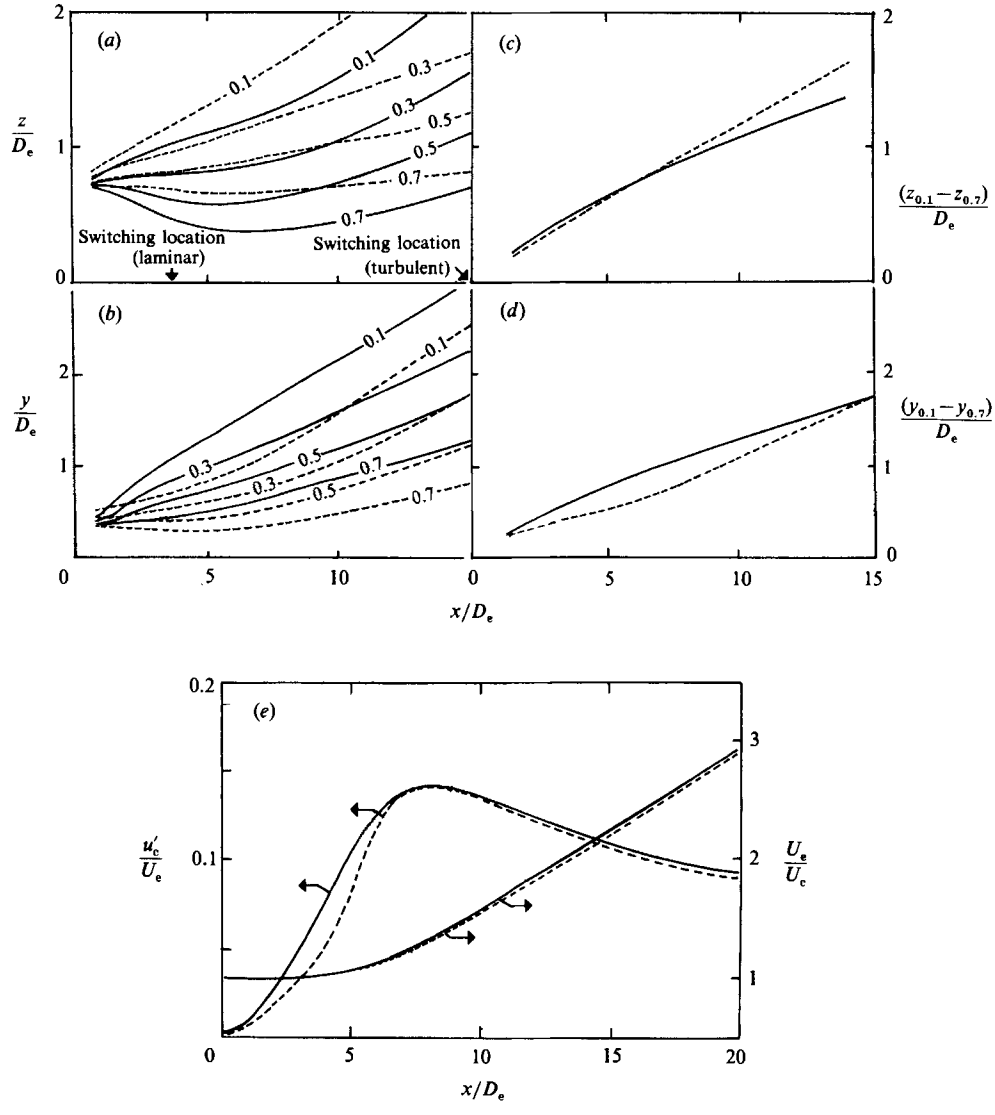

FIGURE 32. Contours of U/U_c: (*a*) in the major plane and (*b*) in the minor plane of N1 (initially laminar) and N4 (initially turbulent) elliptic jets. (*c*) Shear-layer width $(z_{0.1}-z_{0.7})/D_e$ in the major plane; (*d*) shear-layer width $(y_{0.1}-y_{0.7})/D_e$ in the minor plane. (*e*) Centreline U_e/U_c and u_c'/U_e distributions. ——, N1 jet; – – – –, N4 jet. $D_e = 5.08$ cm, $U_e = 10$ ms^{-1}.

layer (nozzle N1). Switchover locations are marked by arrows on the x-axis. Tripping the initial boundary layer moves the switchover location downstream (from $x/D_e \approx 3.5$ to $x/D_e \approx 15$) and significantly changes the spreading of the jet. As a result of tripping, the jet spreads more in the major plane but less in the minor plane. For example, the $U = 0.7U_c$ line shows a significant squashing of the jet in the minor plane owing to tripping. Both of these effects point to a diminished role of coherent structures when the jet is initially turbulent (discussed in the following paragraph). The shear-layer widths, defined as $(y_{0.1}-y_{0.7})/D_e$ and $(z_{0.1}-z_{0.7})/D_e$ in the minor and major planes respectively, as shown in figure 32(*c*, *d*). In the minor plane, the shear-

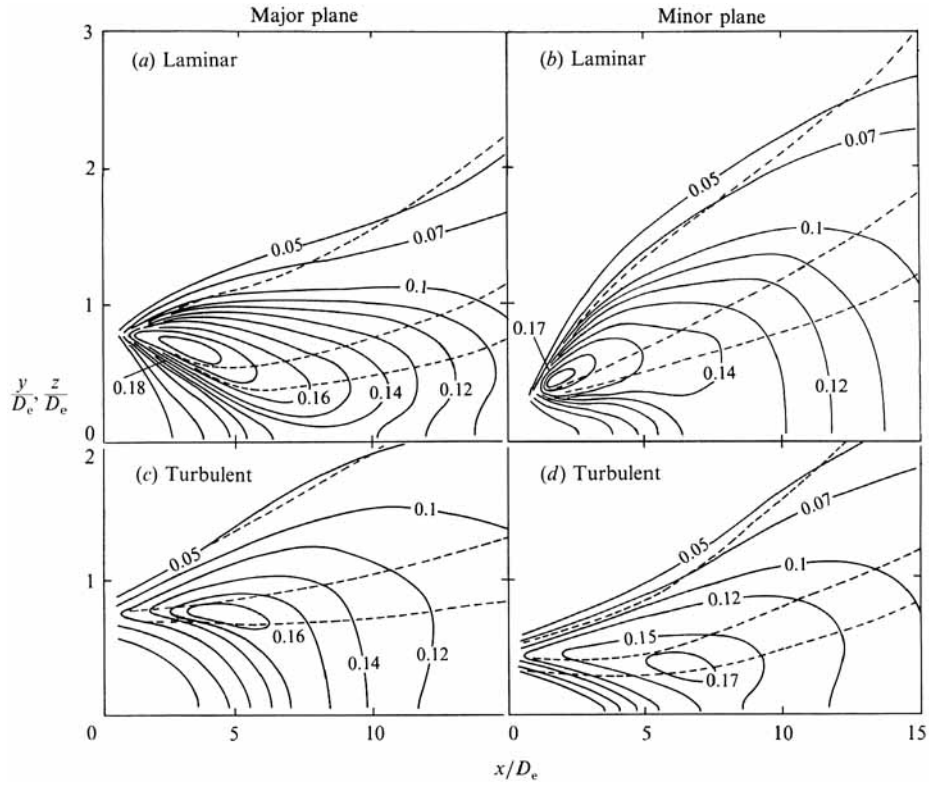

FIGURE 33. Contours of u'/U_e of elliptic jets: (*a*) in the major plane of the initially laminar jet (N1); (*b*) in the minor plane of the jet N1; (*c*) in the major plane of the initially turbulent jet (N4); (*d*) in the minor plane of the jet N4. $D_e = 5.08$ cm, $U_e = 10$ ms^{-1}.

layer width of the initially laminar jet is significantly higher than in the initially turbulent jet, particularly for $5D_e \leqslant x \leqslant 10D_e$. In the major plane, however, these two shear-layer widths are almost the same up to $x/D_e \approx 10$. Farther downstream, the width is greater in the initially turbulent jet.

The profound effect of the initial condition on jet evolution can be explained if we examine the initial instability of the shear layer and the deformation of elliptic vortical structures. The mechanism for shear-layer roll-up in an initially turbulent boundary layer is not yet well understood. Studies of an unexcited single-stream mixing layer with an initially turbulent boundary layer revealed that the roll-up of structures is completed by $x \approx 500\theta_e$ (Hussain & Zaman 1985), while for a laminar shear layer, this distance is less, viz. $x \approx 100\theta_e$. Thus, an initially turbulent shear layer rolls up farther downstream than an initially laminar shear layer. In physical dimensions, this length is much longer because θ_e for the turbulent case is several times that for the laminar case. Thus, the roll-up distance in a tripped shear layer is typically 10–20 times that in a laminar shear layer. In a jet, the instability mechanism is more complicated owing to the imposed geometric lengthscale (say, D_e). From the axial location where the local momentum thickness θ becomes of the order of D_e, the dynamics is controlled by the lengthscale D_e; this region is the so-called *jet column domain*. For the elliptic jet with an initially turbulent boundary layer (N4, $\theta_e = 0.41$ mm), the distance necessary for the shear layer to roll up is well within the jet column domain. The delayed roll-up explains the reduced initial

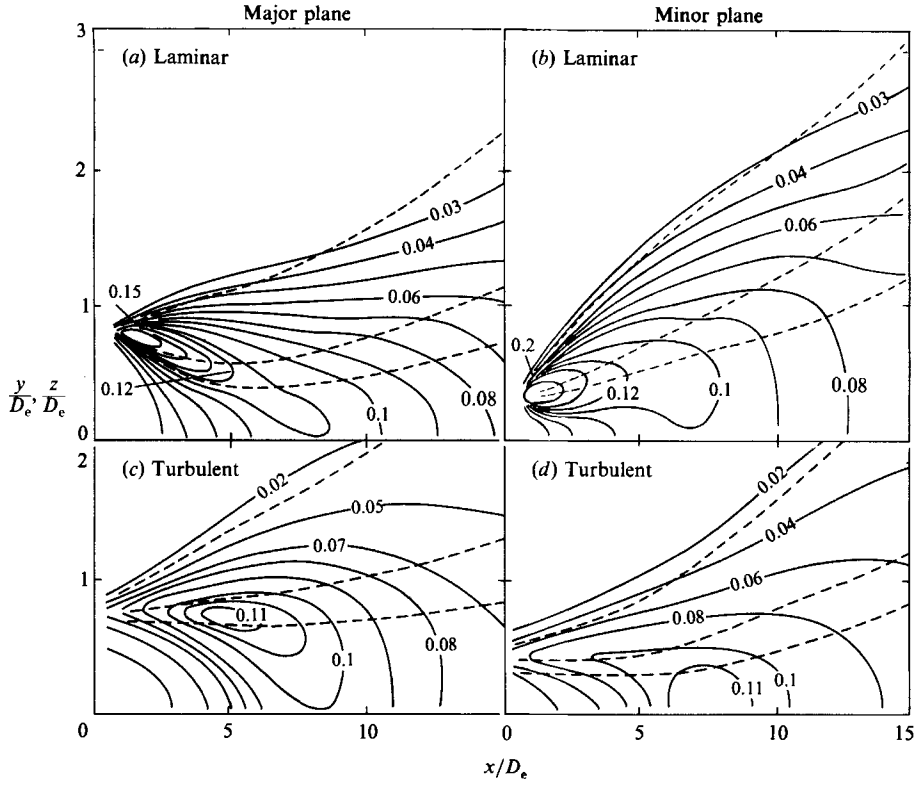

FIGURE 34. Contours of v'/U_e in elliptic jets. $D_e = 5.08$ cm, $U_e = 10$ ms^{-1}. (*a*), (*b*), (*c*) and (*d*) are the same as in figure 33.

spreading of the shear layer (up to $x/D_e \approx 3$). In addition, the thickened shear layer in the tripped jet rolls up into thick-core vortices with relatively weak self-induced velocity (see equation (1)). Such an elliptic vortical structure does not undergo the large distortions experienced by one with a thinner core (typical of initially laminar boundary layers). Consistent with these, unlike in the initially laminar jet, contours of U/U_c in the turbulent case show no significant negative slope in the major plane (figure 32*a*, *b*) and indicate weak inward motion in this plane. In plane or circular jets the motion of the rolled-up structures is simple translation downstream, compared to elliptic jets where the initial vorticity and the core size affect advection of rolled-up structures. Thus the initial condition effect will not be so strong in plane and circular jets.

The centreline mean velocity decay U_e/U_c and longitudinal turbulence intensity distributions u'_c/U_e, are shown in figure 32(*e*); these data are compared with the corresponding initially laminar jet. Although structure formation and subsequent deformation are dependent on the initial condition, the footprint on the mean velocity along the jet axis is fairly insensitive to the initial condition. Distributions of u'_c/U_e, however, show a mild dependence (closer to the exit plane) on the initial condition. Thinner-core vortical structures, closer to the exit plane, cause a higher turbulence intensity in the initially laminar jet.

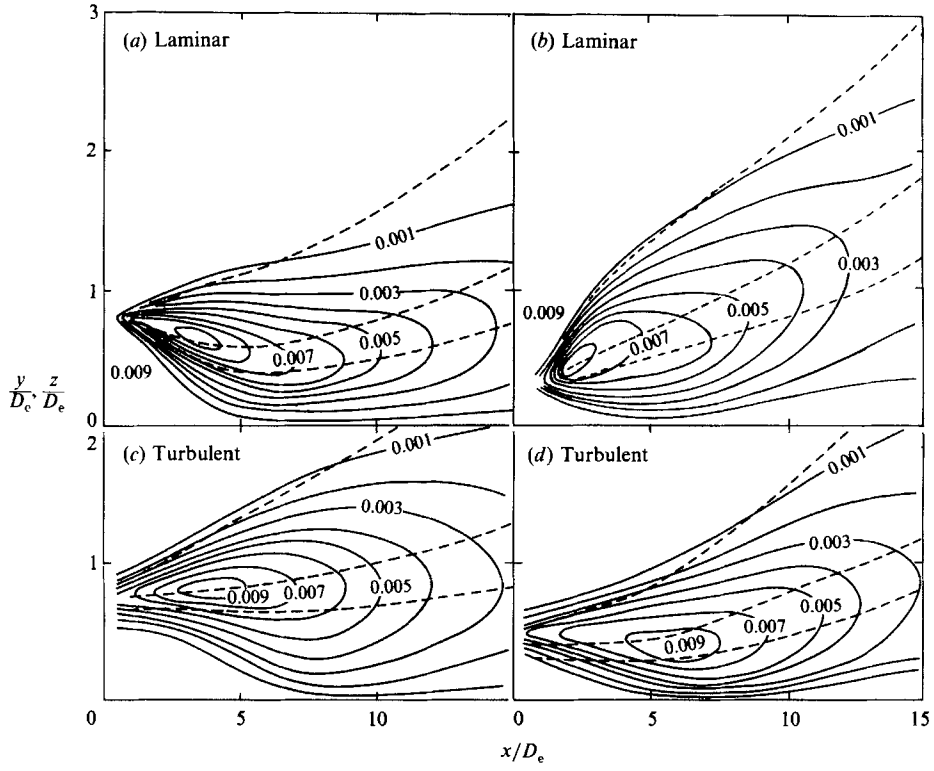

FIGURE 35. Contours of $\overline{uv}/U_e^2$ in elliptic jets. $D_e = 5.08$ cm, $U_e = 10$ ms^{-1}. (*a*), (*b*), (*c*) and (*d*) are the same as in figure 33.

Turbulence measures

Figures 33–35 show the contours of time-average turbulence measures u'/U_e, v'/U_e and $\overline{uv}/U_e^2$ respectively for both initially laminar and turbulent jets (N1 and N4). Dashed lines denoting $U/U_c = 0.1$, 0.5 and 0.7 are included for reference. These figures demonstrate significant influences of the state of the exit boundary layer on the evolution of the mixing layer in an elliptic jet. For the initially laminar jet, the higher-level contours of u', v' and $\overline{uv}$ in the major plane are inclined towards the jet axis, while these contours in the minor plane are inclined in the opposite direction. These opposite trends of inclinations of the contours are direct consequences of the deformation of elliptic structures (caused by self-advection) during their evolution. Since the deformation of elliptic structures in a turbulent jet is not as severe as in a laminar jet, the contours of u', v' and $\overline{uv}$ in the turbulent elliptic jet do not show a strong inclination in either plane.

In the following, we contrast the observations between the cases of initially laminar and turbulent boundary layers. All of the time-average turbulence measures (viz. u', v' and $\overline{uv}$) attain their maximum values much closer to the exit of the jet when initially laminar. Since the locations of u' and v' peaks are related to the location of structure roll-up, the contours of u' and v' suggest that structures are indeed formed farther downstream in the initially turbulent case. For example, contrast the contours in the minor plane only: the peaks occur beyond $x = 5D_e$ in the turbulent case but much closer to the exit plane (around $x = D_e$) in the laminar case. In the major plane this difference between the laminar and turbulent cases is less.

In both the major and minor planes, the peak values of u' as well as v' are higher when the jet is initially laminar. In the minor plane, areas encompassed by contour levels, for example $u'/U_e = 0.05$ and 0.12, $v'/U_e = 0.05$ and 0.08, and $\overline{uv}/U_e^2 = 0.001$ and 0.005, are about 15–20% larger for the laminar jet. In the major plane, the peak values of $\overline{uv}$ and the areas encompassed by constant contour levels of u', v' and $\overline{uv}$ are almost the same for both initially laminar and turbulent cases. Contours of u', v' and $\overline{uv}$, having high peak values and occupying larger areas, signify that mixing in an elliptic jet is more efficient, when laminar than turbulent. These differences are not unexpected because the smaller core (hence thinner) vortices in the laminar case undergo greater three-dimensional deformation as well as more energetic interactions like pairing. These differences between the laminar and turbulent cases (as clearly highlighted by the contours in figures 32–35) are an example of passive control of near-field turbulence. Also, as noted in §6, laminar jets are more amenable to active control via excitation.

8. Concluding remarks

Through hot-wire measurements, we have studied various time-average turbulence measures of elliptic jets of moderate aspect ratios. This study includes the effects of initial condition (initially laminar and turbulent boundary layers), non-uniformity of boundary-layer thickness along the exit perimeter, aspect ratio, and frequency and amplitude of excitation on the time-average measures. As a supplement to quantitative measurements, we employed flow visualization to obtain a better understanding of the flow physics. We have shown that some of the time-average turbulence measures can be explained in terms of the dynamics of large-scale elliptic vortical structures. The main difference with circular jets stems from the fact that the curvature-dependent self-advection of the vortical structures in an elliptic jet produces three-dimensional deformation leading to switching of axes and enhanced large-scale mixing. Since the self-induced motion depends on the local curvature and on the core radius, the effect of initial boundary-layer characteristics (which controls the core radius of rolled-up vortices) is more pronounced in elliptic jets than in circular jets.

Our interest in the coherent structures of non-uniform azimuthal curvature spurred our study of elliptic jets. The dynamics of elliptic vortical structures seems to be important also in technological applications. Turbulence management in this flow, like in other turbulent shear flows, can be achieved through the modification of initiation, evolution, interaction and breakdown processes of coherent structures. Passive control of turbulence through modification of the nozzle from a circular shape to an elliptic shape has proved to be efficient and, combined with proper excitation, appears promising for controlling transports of mass, momentum and heat – much more than is possible in circular jets. Clearly, effective turbulence management requires fundamental understanding of the coherent structure dynamics. Hence the motivation of our next phase of study (Parts 2 and 3).

As in circular jets, the jet column coherent structures in moderate-aspect-ratio elliptic jets are also characterized by preferred mode and stable pairing mode. Various time-average measures (equivalent jet width, mean velocity decay, centreline turbulence level, etc.) and also the jet column instability show that the equivalent diameter D_e is the most appropriate lengthscale for elliptic jets of moderate aspect ratios. At very high aspect ratios, elliptic jets should behave like plane jets.

The occurrence, let alone the dominant dynamical role, of coherent structures in fully turbulent flows, continues to be questioned by researchers. Switching of axes far downstream of the end of potential core is indeed a definite proof. Without any dominant and frequently occurring large-scale elliptic vortical structures, there is no mechanism which can cause systematic switchover of jet cross-section in the far field. Coherent structures in the far field of jets, wakes and mixing layers have been addressed previously (Tso 1983; Hayakawa & Hussain 1985; Metcalfe *et al.* 1987).

Studies of isolated elliptic vortices have revealed that, for aspect ratios greater than about 3.5, the deformation is so severe that instead of periodic switching of axes, an elliptic vortex splits into two vortices via the cut-and-connect interaction. Similar bifurcation of elliptic vortical structures were observed to occur in the 4:1 elliptic jet (but not in the 2:1 jet) under excitation at the preferred mode frequency, resulting in a large increase in the jet cross-sectional area and in mixing. This suggests that, for a given equivalent diameter, the aspect ratio is an important parameter controlling the deformation and topological changes (e.g. bifurcation) of the large-scale vortical structures in elliptic jets, and that the dynamics of low-aspect ratio elliptic jets are basically different from jets of moderate to high aspect ratios.

It is widely believed (notably, Winant & Browand 1974; Laufer 1983; Ho & Huerre 1984) that large-scale engulfment and enhanced mixing and momentum transport occur during pairing. However, the present data show that deformation of vortical structures can significantly increase entrainment and mixing in elliptic jets even without pairing. One should expect that a combination of these two effects, i.e. the deformation and pairing of vortices in elliptic jets should produce dramatic effects on the transports of mass, momentum and heat (cut-and-connect should contribute additionally). This provides the motivation for examining in detail the pairing dynamics in elliptic jets – the subject of Part 2.

The authors are grateful to James Bridges for providing results of numerical simulations and for careful reviews of the manuscript, and to him and Julian Hunt for many fruitful dicussions. This work was supported by NASA-Lewis Research Center Grant No. NAG 3-639 and Department of Energy Grant No. DE-FG05-88ER13839.

Appendix. Effects of aspect ratio: sharp-edged elliptic nozzles

The effect of aspect ratio on the development of elliptic jets has been studied further by extending the aspect ratio up to 8. From what precedes, it is clear that the deformation and evolution of near-field elliptic vortical structures and the jet characteristics are very sensitive not only to the state of the exit boundary layer (say, laminar or turbulent) but also to its thickness θ_e and spanwise uniformity. One would also expect a substantial dependence of the jet characteristics on the aspect ratio. To study the effect of the aspect ratio alone, the initial condition (i.e. jet exit plane details) for all the nozzles must be kept the same while the aspect ratio is varied. It will be practically impossible to achieve this condition using contoured elliptic nozzles of various aspect ratios: nozzles will vary in the exit boundary layer (mean, turbulence and spectral) measures as well as in the spanwise variations of these measures. We addressed this problem by using (sharp-edged) orifice nozzles which are characterized by initial shear layers of virtually zero momentum thickness and of no noticeable azimuthal variations (in θ_e, fluctuation amplitude and frequency). All the orifice jets used for this study were of the same – but smaller –

equivalent diameter $D_e = 2.54$ cm (see table 1) so that, even at the aspect ratio of 8, the settling chamber size left the azimuthal homogeneity of the initial shear layer unaffected.

Jet width and velocity decay

The initial instability of a shear layer originating from a sharp-edged orifice is basically that of a curved shear layer, which is formed as the stagnation streamline separates from the lateral edge (for more on the instability of plane orifice nozzle, see Clark & Kit 1980; Foss & Korschelt 1983). Owing to the curved streamlines, the issuing jet forms a *vena contracta* downstream of the exit plane. Thus, unlike a jet issuing from a contoured nozzle, orifice jets show an initial decrease (up to $x \approx 0.5D_e$) in the jet width on both major and minor planes (figure 36*a*). However, from about $x = 0.8D_e$ onward, the jet width in the minor plane starts increasing like that in a contoured jet. The decrease in the jet width in the major plane is due to the combined effects of the *vena contracta* and the deformation of the elliptic vortical structures. In orifice jets, the switching of axes takes place closer to the exit plane than in contoured nozzles. This is to be expected because the extremely thin initial boundary layer produces slender vortical structures with very thin cores (thus high vorticity) and with strong azimuthal variations in induced velocity (equation (1)), and hence earlier switching of axes. Thus the distance x/D_e where the first switching of axes occurs should be a unique function of the aspect ratio; in fact, within the range of our experiment, this distance increases linearly with the aspect ratio (figure 36*b*). Note that the minimum width in the minor plane occurs essentially at the same location (owing to the formation of *vena contracta*) while the location of the minimum in the major plane occurs progressively at larger x with increasing aspect ratio. The locations of these minima are also shown in figure 36*b*. A similar linear variation of switching location with aspect ratio in rectangular jets (Krothapalli *et al.* 1981) occurred at larger x values, presumably owing to the fact that long approach channels with thicker boundary layers were used by them.

Although the jet widths in major and minor planes do not show any apparent systematic variations, the equivalent jet widths for all the jets collapse onto a single curve and increase linearly with x (figure 36*c*). The growth rates of the equivalent jet width, i.e. $\mathrm{d}B_e/\mathrm{d}x$, of both orifice and contoured nozzles are almost the same, being approximately 0.085. This is fairly close to the spread rate of unexcited circular jets, which ranges from 0.082 to 0.101 (Newman 1967; Z. Husain 1982).

The centreline mean velocity decay of the elliptic orifice jets is shown as a function of x/D_e in figure 36(*d*). Velocity decay in circular jets issuing from contoured and orifice nozzles are also included in this figure for comparison. The formation of *vena contracta* in orifice jets increases the jet centreline velocity U_c downstream of the jet exit plane (by about 50%, which equals a drop in U_e/U_c from 1 to 0.68), delays the decay and hence shifts the virtual origin downstream. Shown as an insert in figure 36(*d*) are the details of the initial streamwise variations of the mean velocity on the centreline of the jets. Initially, all orifice jets show a rapid increase in U_c, reaching an asymptotic value of $U_e/U_c \approx 0.68$ at $x/D_e \approx 0.5$. Note that while the rapid increase in U_c is insensitive to nozzle aspect ratio, the subsequent decrease (i.e. relaxation to the decaying behaviour) is strongly dependent on the aspect ratio. Only the dynamics of the rolled-up elliptic vortices can explain this dependence. The value $U_e/U_c \approx 0.68$ persists longer (up to $x/D_e \approx 5$) for circular and low aspect ratio orifice jets (e.g. aspect ratios 3:2 and 2:1), but U_c starts decreasing at a faster rate with increasing aspect ratio (to be expected because of higher entrainment at higher

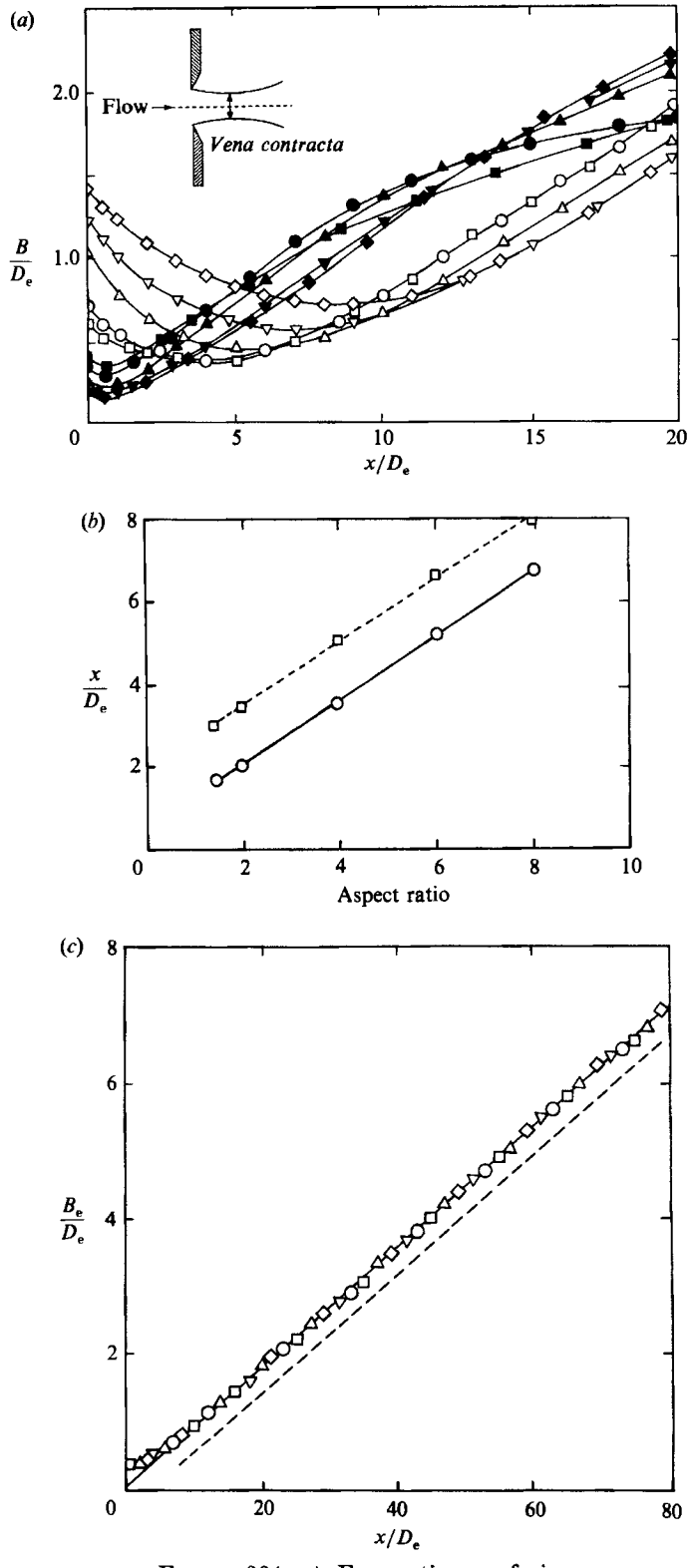

FIGURE 36 (*a–c*). For caption see facing page.

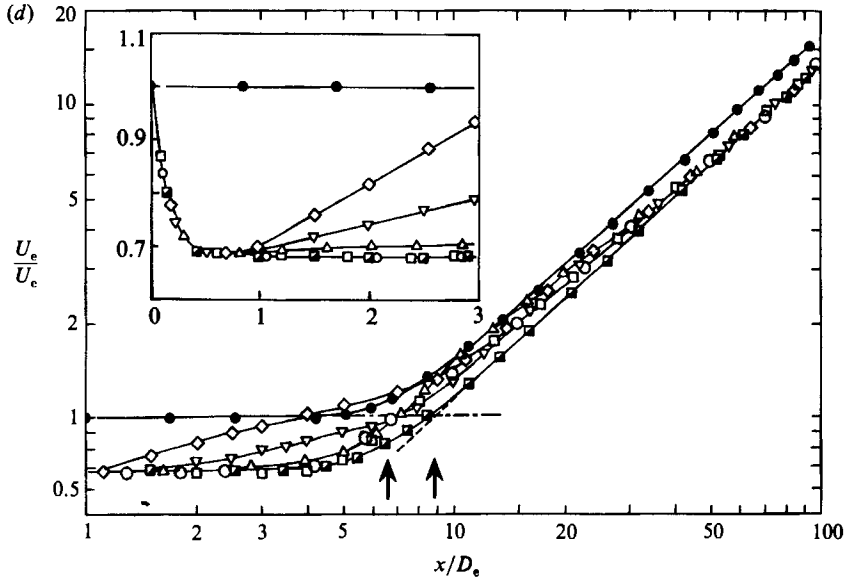

FIGURE 36. (*a*) Jet half widths of orifice jets of various aspect ratios. □, 3:2 jet; ○, 2:1 jet; △, 4:1 jet; ▽, 6:1 jet; ◇, 8:1 jet. Open symbols for major plane; solid symbols for minor plane. (*b*) First axis switchover location as a function of aspect ratio (—○—); locations of the minimum jet width in the major plane (---□---). (*c*) Equivalent jet width of orifice jets. Symbols are the same as in (*a*); – – – –, contoured nozzle circular jet (D = 5.08 cm). (*d*) Centreline mean velocity decay of orifice jets; □, 3:2 jet; ○, 2:1 jet; △, 4:1 jet; ▽, 6:1 jet; ◇, 8:1 jet; ◪, circular orifice jet (D = 2.54 cm); ●, contoured nozzle circular jet (D = 3 cm). Vertical arrows indicate virtual origin. Insert shows data near exit. D_e = 2.54 cm for all elliptic orifice jets and U_e = 29.26 ms^{-1}.

aspect ratios). These differences tend to disappear by the end of the potential core where the decay rate changes. Farther downstream, the decay rates of all orifice elliptic jets reach a constant asymptotic value, matching well with that of the circular jet (beyond $x/D_e \approx 50$). Note that, in this so-called axisymmetric decay region, the decay curves of all orifice nozzle elliptic jets (when non-dimensionalized by D_e) collapse with that of the orifice nozzle circular jet. This is also evidence that D_e is an appropriate lengthscale of elliptic jets.

The virtual origin of elliptic jets (determined by extending the U_c curve in the axisymmetric decay region) and circular jets issuing from orifice nozzles is about $x \approx 9D_e$, which is higher than the value obtained in contoured jets, e.g. $x \approx 6D_e$ (see figure 6*b*), as expected. The virtual origins for the contoured and orifice circular jets are denoted by arrows in figure 36(*d*). From these results it is clear that a change in the initial condition shifts the virtual origin, but does not affect the asymptotic decay rate. A comparison of circular jets from contoured and orifice nozzles shows that changing the nozzle type does not produce the dramatic near-field effects found in elliptic jets, although the achievement of the asymptotic decay rate is considerably delayed in the orifice jet.

Longitudinal turbulence intensity

The centreline r.m.s. intensity of the longitudinal velocity fluctuations u_c'/U_e are shown in figure 37(*a*) for the orifice nozzle elliptic jets and compared with contoured and orifice nozzle circular jets. For a low-aspect-ratio elliptic jet, the deformation as well as the self-induced inward and outward displacements of parts of elliptic

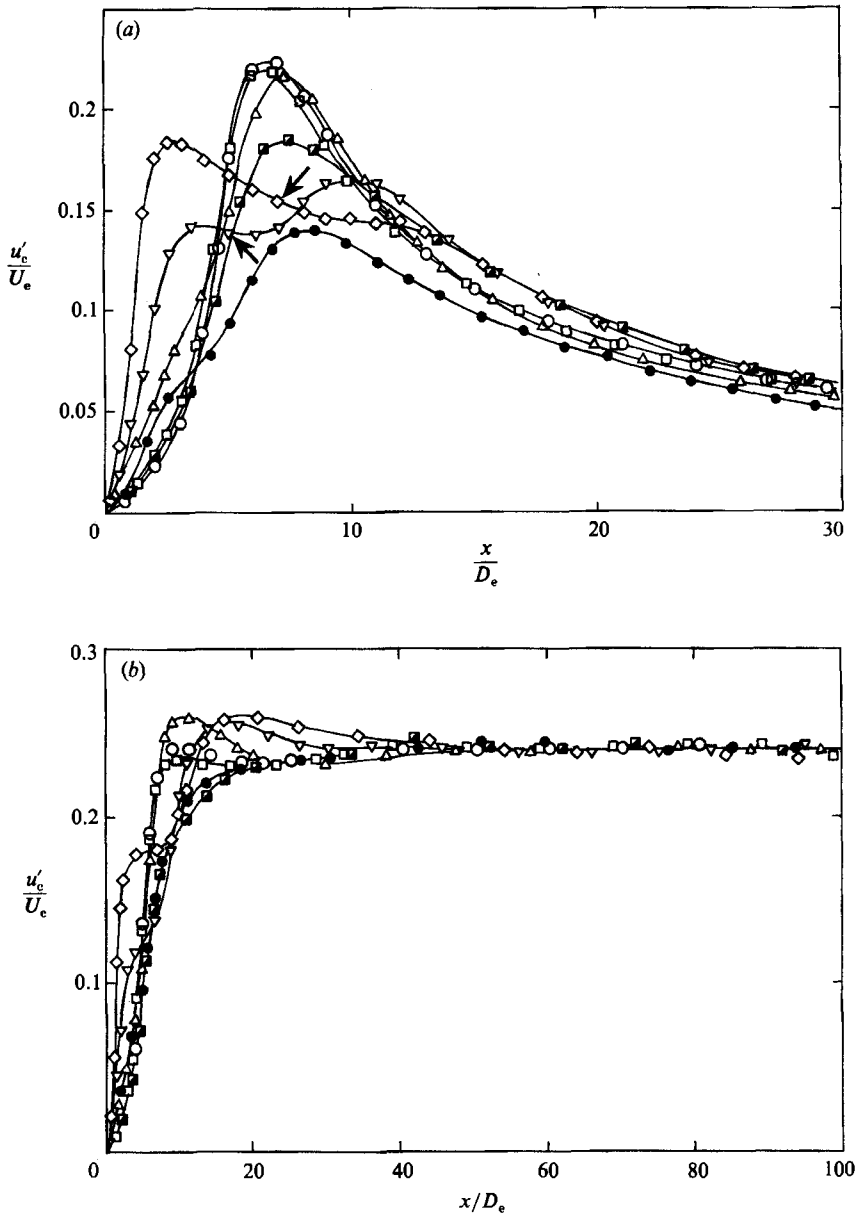

FIGURE 37 (a, b). For caption see facing page.

structures are small. Therefore, the fluctuations are caused primarily by advection of structures past a stationary probe. The r.m.s. fluctuations in the 3:2 and 2:1 jets show a gradual initial increase in x, attaining a peak value of $x \approx 6D_e$, before the end of the potential core where the structures break down. This trend is similar to that of circular jets. In either circular or elliptic jets, since the formation and breakdown of organized structures both suffer from spatial and temporal jitter, the u_c' distribution does not show separate peaks corresponding to these two events. Under proper excitation, however, structure formation and breakdown events can be localized in space and $u_c'(x)$ distributions then show two separate corresponding

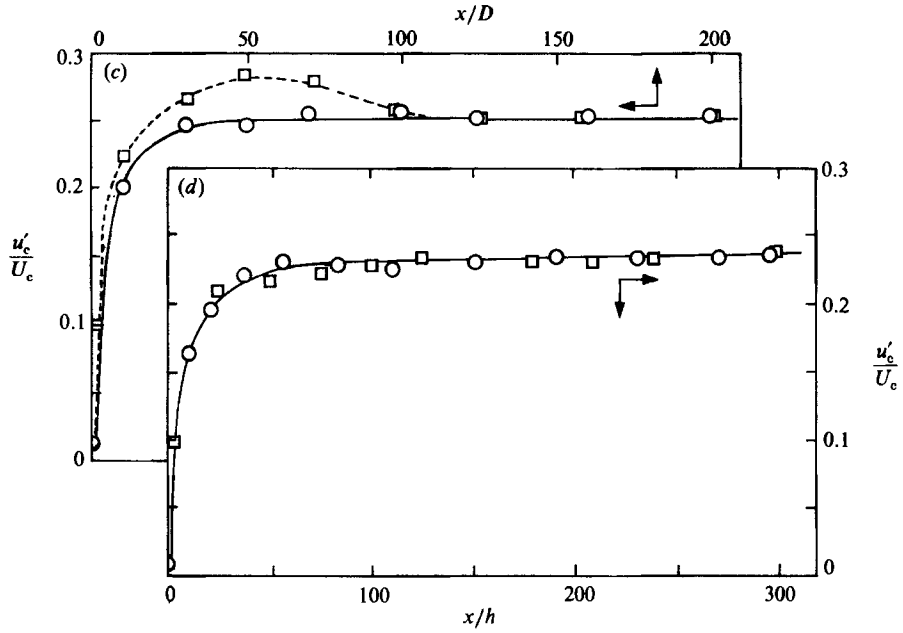

FIGURE 37. Centreline r.m.s. intensity of longitudinal velocity fluctuations in orifice jets: (*a*) dependence of u_c'/U_e on x/D_e; (*b*) dependence of u_c'/U_c on x/D_e. $U_e = 29.26$ ms^{-1}. Symbols are the same as in figure 36(*d*). Centreline r.m.s. intensity of longitudinal velocity fluctuations in contoured jets: (*c*) initially laminar and turbulent circular jets; $D = 3$ cm, $U_e = 65$ ms^{-1}; (*d*) plane jet; $h = 1.12$ cm and $U_e = 45$ ms^{-1} for the initially laminar jet; $h = 1.01$ cm and $U_e = 65$ ms^{-1} for the initially turbulent jet. ○, initially laminar; □, initially turbulent.

peaks (discussed in §6.1). Note that the peaks in u_c'/U_e distributions for these orifice nozzle jets are higher than in the contoured nozzle circular jet (figure 37*a*), as expected.

For a higher-aspect-ratio elliptic jet (i.e. 6:1 and 8:1), the structures on the minor-axis sides, being closer to the jet centreline, produce a peak in u_c' close to the exit plane; this peak, caused by advection of structures past the stationary probe, is compounded by self-induced deformations of the structures. Farther downstream, as the minor-axis sides of the structures move away from the jet centreline, u_c' is decreased. Note that the 6:1 and 8:1 jets show a second hump in $u_c'(x)$. This second hump occurs downstream of the axis switchover location (marked by arrows). Flow visualization showed that as the initial major axis sides of structures approach the centreline they typically undergo breakdown. In addition, vortical structures in the 6:1 and 8:1 jets almost certainly undergo cut-and-connect interactions (see §6.2) before breakdown. The cut-and-connect, formation of threads and subsequent breakdown of structures together cause the second hump in $u_c'(x)$ distribution. The lower turbulence level of the second hump does not necessarily suggest a weaker event, but instead, perhaps jitter in the location of cut-and-connect, cascade to smaller threads and breakdown to finer scales. Note that beyond about $15D_e$ there is no perceptible difference between the $u_c'(x)$ data for different aspect ratios.

To determine the appropriate lengthscale and to examine the achievement of self-preservation, u_c'/U_c data are plotted against x/D_e (figure 37*b*). In these coordinates, for $x/D_e > 40$, u_c'/U_c distributions for all elliptic jets show a reasonable collapse with those of circular jets, suggesting that, indeed, the equivalent diameter is a

	Type of jet	u_c'/U_c	$x/D, x/h$
Heskestad (1965)	Plane	0.264	160
Bradbury (1965)	Plane	0.209	60
Gutmark & Wygnanski (1976)	Plane	0.27	120
Z. Husain (1982)	Plane	0.24	300
Corrsin & Uberoi (1950)	Circular	0.22	26
Wygnanski & Fiedler (1969)	Circular	0.28	40
Z. Husain (1982)	Circular	0.25	200

TABLE 2. Comparison of far-field centreline turbulence intensities measured by different investigators

meaningful lengthscale. Note that, u_c'/U_c for all elliptic jets reaches an asymptotic value of about 0.24 at $x \approx 50D_e$. A constant value of u_c'/U_c may suggest that the elliptic jets have attained self-preservation for $x/D_e > 50$. But, once again, similar to centreline mean velocity decay, the $u_c'/U_c(x)$ distribution in the far field is not sensitive to switchover of axes. Thus, it is unlikely that elliptic jets (especially moderate to high aspect ratios) attain true self-preservation even up to $x/D_e \approx 100$.

The asymptotic value of u_c'/U_c for circular jets (Corrsin & Uberoi 1950; Wygnanski & Fiedler 1969) and plane jets (Heskestad 1965; Bradbury 1965; Gutmark & Wygnanski 1976; Everitt & Robins 1978) shows quite a wide variation: from 0.19 to 0.32 (asymptotic values of u_c'/U_c obtained by various investigators are listed in table 2). Heskestad and Gutmark & Wygnanski's data in plane jets (taken up to $x/h = 140$ and 120 respectively) did not reach an asymptotic value. There have been tentative suggestions by various investigators that the initial condition may be important. This is certainly true in the near field of jets (Hussain & Clark 1977), while it is difficult to explain a continued influence in the far field unless there is large deformation of organized structures.

Measurements in the far field of a jet, where velocity is quite low, need careful attention. Perry & Morrison (1971) have noticed that hot-wire measurements in the low-velocity range (less than 10% of the full range) can give rise to noticeable error. Using a few ranges of calibrations (so that at each downstream location, the velocity can be computed from the linear range of the hot-wire calibration), the effects of various initial conditions in the far fields of circular (up to $x/D = 200$) and plane ($x/h = 300$) jets were studied in our laboratory (Z. Husain 1982). It was found that the value of u_c'/U_c became independent of initial and boundary conditions, and reached the asymptotic value at $x/D = 100$ in the circular jets and at $x/h = 150$ in the plane jets. These data are shown in figure 37(*c*, *d*). In the circular jet with laminar exit boundary layer, however, the asymptotic value is achieved at $x/D \approx 50$, which agrees well with the present data of both circular and elliptic jets. Note that, in the present study, we used a second calibration for measurements in the far field to assure greater accuracy.

Based on our experience in various circular, plane and elliptic jets, we claim that the centreline turbulence intensities in the self-preserving regions of free jets (irrespective of nozzle geometry) is in the range 0.245 ± 0.005. We note from Bevilaqua & Lykoudis (1978) and Wygnanski, Champagne & Marasli (1986) that u_c'/U_c does not reach a constant value in wakes with different initial conditions, but have no explanation yet for their data except to suggest that wakes require a much longer distance for the achievement of self-preservation.

Previous studies of rectangular jets (Sforza, Steiger & Trentacoste 1966; Krothapalli *et al.* 1981; Tsuchiya, Horikoshi & Sato 1984) and elliptic jets (Ho & Gutmark 1987) have used various lengthscales such as minimum width $2b$, semi-major axis a, and hydraulic diameter D_h ($\equiv 4 \times$ nozzle area/perimeter). Obviously, a high-aspect-ratio elliptic jet should behave like a plane jet and the slit width $2b$ is then a more meaningful lengthscale. But none of these lengthscales are found to be satisfactory to characterize elliptic jets of low to moderate aspect ratios. It is tempting to use hydraulic diameter as the lengthscale for irregular jets. Conceptually, hydraulic diameter is a relevant lengthscale in a situation where frictional drag is an important parameter (e.g. frictional drag in a non-circular pipe), but its usefulness in a jet is nebulous at best. From all the time-average measures we have studied, the equivalent diameter D_e appears to be the most appropriate lengthscale for low to moderate aspect ratios.

REFERENCES

ARMS, R. J. & HAMA, F. R. 1965 *Phys. Fluids* **8**, 553.

BATCHELOR, G. K. 1967 *An Introduction to Fluid Dynamics*. Cambridge University Press.

BECKER, H. A. & MASSARO, T. A. 1968 *J. Fluid Mech.* **31**, 435.

BEVILAQUA, P. M. & LYKOUDIS, P. S. 1978 *J. Fluid Mech.* **89**, 589.

BRADBURY, L. J. S. 1965 *J. Fluid Mech.* **23**, 31.

BRADSHAW, P. 1966 *J. Fluid Mech.* **26**, 225.

BRIDGES, J. E. 1984 Effects of initial condition on jet noise. MS thesis, University of Houston.

BRIDGES, J. E. & HUSSAIN, A. K. M. F. 1987 *J. Sound Vib.* **117**, 289.

CLARK, J. A. & KIT, L. 1980 *Trans. ASME* I: *J. Fluids Engng* **102**, 219.

COLES, D. E. 1962 *Rand Corp. Rep.* R-403-PR.

CORRSIN, S. & UBEROI, M. S. 1950 *NACA Rep.* 988.

CRIGHTON, D. G. 1973 *J. Fluid Mech.* **59**, 665.

CROW, S. C. & CHAMPAGNE, F. H. 1971 *J. Fluid Mech.* **48**, 547.

DHANAK, M. R. & BERNARDINIS, B. 1981 *J. Fluid Mech.* **109**, 189.

EVERITT, K. W. & ROBINS, A. G. 1978 *J. Fluid Mech.* **88**, 563.

FOSS, J. F. 1977 *Symp. Turb. Shear Flows*, p. 11.3. Pennsylvania State University.

FOSS, J. F. & KORSCHELT, J. F. 1983 *J. Fluid Mech.* **132**, 79.

GUTMARK, E. & HO, C. M. 1985 *AIAA J.* **23**, 354.

GUTMARK, E. & WYGNANSKI, I. 1976 *J. Fluid Mech.* **73**, 465.

HAYAKAWA, M. & HUSSAIN, A. K. M. F. 1985 *Turbulent Shear Flows*, vol. 5, p. 4.33. Cornell University. (See also *J. Fluid Mech.* **180** (1987) 193.)

HERNAN, M. A. & JIMENEZ, J. 1982 *J. Fluid Mech.* **119**, 923.

HESKESTAD, G. 1965 *J. Appl. Mech.* **32**, 721.

HO, C. M. & HUERRE, P. 1984 *Ann. Rev. Fluid Mech.* **16**, 365.

HO, C. M. & GUTMARK, E. 1987 *J. Fluid Mech.* **179**, 383.

HUSAIN, H. S. 1984 An experimental investigation of unexcited and excited elliptic jets. PhD thesis, University of Houston.

HUSAIN, H. S. & HUSSAIN, A. K. M. F. 1983 *Phys. Fluids* **26**, 2763.

HUSAIN, Z. D. 1982 An experimental study of effects of initial and boundary conditions on near and fair fields of jet flows. PhD thesis, University of Houston.

HUSSAIN, A. K. M. F. 1980 *Lecture Notes in Physics*, vol. 136, p. 252. Springer.

HUSSAIN, A. K. M. F. 1983 *Phys. Fluids* **26**, 2816.

HUSSAIN, A. K. M. F. & CLARK, R. 1977 *Phys. Fluids* **20**, 1416.

HUSSAIN, A. K. M. F. & ZAMAN, K. B. M. Q. 1985 *J. Fluid Mech.* **159**, 85.

KELLY, R. E. 1967 *J. Fluid Mech.* **27**, 667.

KIDA, S., TAKAOKA, M. & HUSSAIN, F. 1989 *Phys. Fluids* A **1**, 630.

KROTHAPALLI, A., BAGANOFF, D. & KARAMCHETI, K. 1981 *J. Fluid Mech.* **107**, 201.

LAUFER, J. 1983 *J. Appl. Mech.* **50**, 1079.

MAXWORTHY, T. 1974 *J. Fluid Mech.* **64**, 227.

MELANDER, M. V. & HUSSAIN, F. 1988 *NASA-Stanford CTR Rep.* CTR-88, p. 257. (See also *Phys. Fluids A* **1** (1989) 633.)

METCALFE, R., HUSSAIN, A. K. M. F., MENON, S. & HAYAKAWA, M. 1987 *Fifth Symp. Turbulent Shear Flow*, vol. 5 (ed. F. Durst, B. E. Launder, F. W. Schmidt & J. H. Whitelaw), p. 110. Springer.

MONKEWITZ, P. A. 1988 *J. Fluid Mech.* **188**, 223.

MORRIS, P. J. 1986 *AIAA paper no.* 86-1868, AIAA 10th Aeroacoustics Conf. July 9–11, Seattle, Washington.

NEWMAN, B. G. 1967 *Fluid Mechanics of Internal Flow* (ed. G. Sorvan), p. 170. Elsevier.

PERRY, A. E. & MORRISON, G. L. 1971 *J. Fluid Mech.* **47**, 765.

ROCKWELL, D. O. 1972 *Trans. ASME* E: *J. Appl. Mech.* **52**, 263.

SFORZA, P. M., STEIGER, M. H. & TRENTACOSTE, N. 1966 *AIAA J.* **4**, 800.

TAKAKI, R. & HUSSAIN, A. K. M. F. 1985 *Turbulence Shear Flows*, vol. 5, p. 3.19, Cornell University.

TSO, J. 1983 Coherent structures in a fully developed turbulent axisymmetric jet. PhD thesis, Johns Hopkins University. (See also *J. Fluid Mech.* **203** (1989) 425.)

TRENTACOSTE, N. & SFORZA, P. M. 1967 *AIAA J.* **5**, 885.

TSUCHIYA, Y., HORIKOSHI, C. & SATO, T. 1984 *Turbulence Symp.* p. 15.1, University of Missouri-Rolla.

VIETS, H. & SFORZA, P. M. 1972 *Phys. Fluids* **15**, 230.

WINANT, C. D. & BROWAND, F. K. 1974 *J. Fluid Mech.* **63**, 237.

WYGNANSKI, I. & FIEDLER, H. 1969 *J. Fluid Mech.* **38**, 577.

WYGNANSKI, I., CHAMPAGNE, F. & MARASLI, B. 1986 *J. Fluid Mech.* **168**, 31.

ZAMAN, K. B. M. Q. & HUSSAIN, A. K. M. F. 1977 *Turb. Shear Flows*, p. 11.23, Pennsylvania State University.

ZAMAN, K. B. M. Q. & HUSSAIN, A. K. M. F. 1980 *J. Fluid Mech.* **101**, 449.